Miniaturized Chip-Scale Quantum and Terahertz Systems Through Tight Integration of Electronics, Electromagnetics, and Qubits

by

Mohamed Ibrahim Mohamed Ibrahim

B.Sc., Electrical Engineering, Ain Shams University (2012)
M.Sc., Electrical Engineering, Ain Shams University (2016)
M.S., Electrical Engineering and Computer Science, Massachusetts Institute of Technology (2020)

Submitted to the Department of Electrical Engineering and Computer Science
in partial fulfillment of the requirements for the degree of

Doctor of Philosophy in Electrical Engineering and Computer Science

at the

MASSACHUSETTS INSTITUTE OF TECHNOLOGY

September 2021

Author . . . .
Department of Electrical Engineering and Computer Science
August 27, 2021

Certified by . . . .
Ruonan Han
Associate Professor of Electrical Engineering and Computer Science
Thesis Supervisor

Accepted by . . . .
Leslie A. Kolodziejski
Professor of Electrical Engineering and Computer Science
Chair, Department Committee on Graduate Students

Miniaturized Chip-Scale Quantum and Terahertz Systems Through Tight Integration of Electronics, Electromagnetics, and Qubits

by

Mohamed Ibrahim Mohamed Ibrahim

Submitted to the Department of Electrical Engineering and Computer Science
on August 27, 2021, in partial fulfillment of the
requirements for the degree of
Doctor of Philosophy in Electrical Engineering and Computer Science

Abstract

The utilization of electromagnetic waves in quantum information science and the least-explored terahertz (THz) regime are posed to revolutionize sensing, computing, and communication. The key to the prosperity of such a frontier is the development of integrated circuits that enable high-precision and high-flexibility manipulation of the RF-to-optical spectrum. This thesis presents innovations of chip-scale quantum and THz systems, which allow for significant miniaturization, practical solutions, and exciting research opportunities across the device, circuit, and system levels. To illustrate such opportunities, we propose two chip-scale systems realized through tight integration of electronics, electromagnetics, and qubits on CMOS technology. The first one is a hybrid CMOS magnetometer that integrates the essential microwave and optical components to control and measure the field-sensitive quantum states of the solid-state nitrogen-vacancy (NV) centers in diamond. This hybrid architecture is a step to achieve compact and scalable integrated platforms towards quantum-enhanced sensing and information processing. The second system is a package-less THz identification tag (THzID) in CMOS, the smallest monolithic ID chip with far-field communication capability, beam steering, and asymmetric cryptography. This ID opens the door to aggressively utilize the overlooked size shrinkage aspect of THz technology while sustaining broad-bandwidth and low-power operation. The thesis is concluded with potential improvements and perspectives for future work, in addition to several research directions that utilize the advantages of wireless communication and quantum systems, enabling new paradigms in sensing, computing, and communication infrastructures.

Thesis Supervisor: Ruonan Han
Title: Associate Professor of Electrical Engineering and Computer Science

Acknowledgments

First, I wish to express my most gratitude to my thesis supervisor, Prof. Ruonan Han, for his guidance, encouragement, and useful discussions. He has been more than a technical supervisor to me and I have learned a lot from him throughout my PhD at MIT.

I would also like to thank my PhD committee members Prof. Dirk R. Englund, and Prof. Anantha P. Chandrakasan. I was fortunate to work with Prof. Englund through the collaboration of creating the CMOS-diamond hybrid quantum systems. I also had the honor to work with Prof. Chandrakasan to realize low-power THz secure wireless systems. I wouldn't have completed my PhD without their help and advice.

Special thanks to my colleague and my friend Christopher Foy who has been working closely with me throughout my PhD in the hybrid CMOS-diamond hybrid magnetometers projects. I would also like to thank Donggyu Kim and Matthew Trushiem for working with Chris and me on the first hybrid magnetometer prototype. All their inputs were essential and the discussions with them were very helpful.

I would also like to thank my teammate Muhammad Ibrahim Wasiq Khan who has been working closely with me in the THzID project. I am also very fortunate to have him as a close friend and coworker in other projects as well. Special thanks to Chiraag S. Juvekar, and Wanyeong Jung for their significant contribution towards the THzID project. I would also like to thank Rabia Tugce Yazicigil for her help and support for the last few years, in addition to her input to the THzID project.

I would also like to acknowledge Isaac Harris, Jinchen Wang, Xiang Yi, and Xingyu Zou who have been working with me on some of the ongoing projects presented in Chapter 5. Furthermore, thanks for the technical discussion and assistance from the rest of my labmates at the THz integrated electronics group including but not limited to: Cheng Wang, Zhi Hu, Nathan Monroe, Mina Kim, Mohamed Elsheikh, Alec Yen, Xibi Chen, and Eunseok Lee.

Special thanks to all my Egyptian friends in Boston. Their support and help during my PhD have been instrumental. Special acknowledgements to my best friends from

Egypt. Although we don't all live in the same country, and we live in 4 different time zones, they have been always there for me, very supportive, good listeners and true friends. Last but not least, I would like to thank my family, my parents, and my sisters. The love, care, support and encouragement they have given me can not be expressed by words. In addition, I would also like to specially thank my fiancée, she has been the best partner, friend and supporter. I can not express my gratitude to her.

Contents

List of Figures

List of Tables

Chapter 1

Introduction

The significant demand for connectivity in the era of the Internet of Things (IoT) requires a revolution in communication, sensing, and computing. New technologies utilizing the high-frequency spectrum including quantum information science and the least-explored terahertz (THz) regime are posed to play a significant role in this revolution. The utilization of electromagnetic waves and the development of integrated circuits that enable significant miniaturization, and practical solutions are key to the prosperity of such frontier. chip-scale implementation of such systems realized through tight integration of electronics, electromagnetics, and qubits opens exciting research opportunities across the device, circuit, and system levels.

1.1 Chip-Scale Terahertz (THz) and Quantum Systems

Exploring the THz gap on-chip has gained significant interest over the past decade to enable new opportunities in imaging, radar, and broadband communication [1–3]. However, utilizing the overlooked aspect of THz systems, which is the ability to shrink the communication node size with the challenge of keeping low-power operation, can pave the way to new paradigms for wireless sensing and IoT systems, especially with the advances in 6G and beyond. In this thesis, a package-less ultra-low-power THz identification tag (THzID) is reported. This tag is the smallest reported ID chip with far-field communication distances, beam steering, and asymmetric cryptography. This tag represents an example of the collaborative nature of the projects presented in this thesis that show the tight integration concept. In this chip, we integrated an ultra-low-power THz front end, a sub-threshold baseband amplifier, a photodiode array for powering through light harvesting, a switched-capacitor based DC-DC converter, and a cryptographic processor to control the chip.

Conventional imaging or radar THz systems are based on the interaction of the waves with macroscopic objects to detect them. In this case, the exact frequency of operation is not strictly important. However, the interaction with microscopic particles, which requires a specific frequency of operation, has emerged to enable advanced sensing, computing, and clocking systems. For example, manipulating the vibrational or rotational modes of molecules to build ultra-stable frequency reference [4] . In this thesis, we focus on the interaction with the spin states of qubits in quantum systems with applications in sensing, imaging, and information processing.

Applications of CMOS integrated circuits in quantum apparatus are gaining increasing attention due to the prospect of significantly increased hardware scalability and reduction of cost, size, and power. For instance, CMOS-based control and readout circuitry, operating at cryogenic temperature, have been demonstrated recently to construct large-scale quantum computers [5], [6]. In comparison, the potential of CMOS circuits in another vast application space of quantum systems – high-performance sensing – still awaits more extensive investigations. In this thesis, we present the first integrated hybrid CMOS magnetometer that integrates the electronics with color centers, nitrogen-vacancy (NV) centers in diamond. The system integrates all the necessary components to manipulate and read out the spin states of the NV centers in diamond. This sensor is another example of the interdisciplinary research done in this thesis, where we integrate on-chip electronic, microwave, and photonic components and color-center qubits in the same system. The thesis also provides an outlook on using CMOS circuits to control color centers for quantum information processing applications.

1.2 Thesis Organization

This thesis is organized as follows:

- **Chapter 2** introduces the basic principle of using NV centers in diamond for magnetic field sensing. Next the details of the architecture and the design of the first prototype of the on-chip hybrid CMOS-diamond magnetometer is presented. Finally, the measurements setup and results of the sensing performance are introduced.

- **Chapter 3** describes the scalable magnetometer chip architecture, which incorporates high-homogeneity microwave delivery in addition to optical filtering that is based on plasmonic and Talbot effects. The measurement setup and results and the magnetic sensing performance are also introduced.

- **Chapter 4** presents the overall architecture of the THzID chip. Details of the THz downlink and uplink circuits are also given. Then, the ECC security protocol and the photo-voltaic powering scheme are discussed. Finally the experiment demonstrations and comparisons with the prior state-of-the-arts are presented.

- **Chapter 5** provides a conclusion for the projects presented in this thesis. We also point out potential improvements and perspectives for future work. In addition, exciting research directions that utilize the advantages of wireless communication and quantum systems, enabling new paradigms in sensing, computing, and communication are also introduced.

1.3 Publications

Much of the work presented in this dissertation has been previously published or submitted for publication. Main works contributing to this thesis [1]:

- [38]: **Mohamed I. Ibrahim***, Christopher Foy*, Donggyu Kim*, Dirk R. Englund, "Room-temperature quantum sensing in CMOS: On-chip detection of electronic spin states in diamond color centers for magnetometry," *IEEE VLSI Circuits Symposium*, Honolulu, HI, June 2018.
- [39]: Donggyu Kim*, **Mohamed I. Ibrahim*** , Christopher Foy, Matthew E. Trusheim, Ruonan Han, and Dirk R. Englund, "A CMOS-integrated quantum sensor based on nitrogen–vacancy centres," *Nature Electronics*, 2(7):284–289, 2019.
- [47]: **Mohamed I. Ibrahim**, Christopher Foy, Dirk R. Englund, and Ruonan Han, "A scalable quantum magnetometer in 65nm CMOS with vector-field detection capability," *IEEE Int. Solid-State Circuit Conf. (ISSCC)*, San Francisco, CA, Feb. 2019.
- [48]: **Mohamed I. Ibrahim***, Christopher Foy*, Dirk R. Englund, and Ruonan Han, "High-scalability CMOS quantum magnetometer with spin-state excitation and detection of diamond color center," *IEEE Journal of Solid-State Circuits (JSSC)*, vol. 56, no. 3, Mar. 2021.
- [71]: **Mohamed I. Ibrahim**, Muhammad Ibrahim Wasiq Khan, Chiraag S. Juvekar, Wanyeong Jung, Rabia Tugce Yazicigil, Anantha P. Chandrakasan, and Ruonan Han, "THzID: a 1.6 mm^2 package-less cryptographic identification tag with backscattering and beam-steering at 260GHz," *IEEE Intl. Solid-State Circuit Conf. (ISSCC)*, San Francisco, CA, Feb. 2020.
- [72]: Muhammad Ibrahim Wasiq Khan, **Mohamed I. Ibrahim**, Chiraag S. Juvekar, Wanyeong Jung, Rabia Tugce Yazicigil, Anantha P. Chandrakassan, and R. Han, "CMOS THz-ID: a 1.6 mm^2 package-less identification tag using asymmetric

---

[1] *Equal Contributions to the paper

cryptography and 260-GHz far-field backscatter communication," *IEEE Journal of Solid-State Circuits (JSSC)*, vol. 56, no. 2, Feb. 2021.

Chapters 2, 3, and 4, reproduce and adapt material from previous published works. Chapter 2 is adapted from Ref. [38], and [39], with Chapter 3 being adapted from Ref. [47], and [48]. In addition, Chapter 4 report results from references [71] and [72].

1.4 Co-worker Contributions

The collaborative work presented in this thesis would not have been possible without the valuable contributions of my research colleagues. I would like to mention, first, my thesis supervisor, Prof. Ruonan Han, who guided me through all the projects presented in this thesis. Our useful discussions were invaluable for me. The substantial guidance, advice and technical inputs of Prof. Dirk R. Englund and Prof. Anantha P. Chandrakasan to the work presented in this thesis were crucial. The rest of my co-workers' contributions are summarized below:

- The idea of CMOS-Diamond integration described in Chapter 2 was initially conceived by Dirk Englund and Ruonan Han. The idea of stacking the microwave inductor, plasmonic filter and photodiode in a 3D architecture was developed by myself. Christopher Foy and myself contributed mainly to the chip specifications. I was responsible for the CMOS chip design with all the related items such as circuits schematics and physical layout. Dongyyu Kim performed FDTD simulations for the optical filter design. Chris, Dongyyu and I contributed equally to the experiments. Chris prepared the control software for the experiment. Chris and Dongyyu constructed the optical set-up. I prepared the electronic measurements platform.

- The scalable magnetometer chip design specification presented in Chapter 3 was done by Christopher Foy and myself. I developed the scalable microwave launcher, multi-layer photonic filter and the rest of the integrated components on the chip. The optical setup, MATLAB code base, and diamond acquisition were led by Chris.

Chris and I performed the experiments, analyzed the data, and characterized the chip performance.

- The ThzID system design presented in Chapter 4 was led by my self in a collaboration with Muhammad Ibrahim Wasiq Khan, Rabia Tugce Yazicigil, Chiraag S. Juvekar, and Wanyeong Jung. Ibrahim Khan and I were responsible for the THz/analog front-end. I conceived and constructed the multi-functional patch antenna. Ibrahim designed the THz square-law detector. Ibrahim and I contributed to the design of the SSB mixer, and the base-band amplifier. I was responsible for the co-design of the antennas and the photodiode array. Wanyeong designed the DC-DC converter. Chiraag and Rabia designed the ECC processor. The system integration was mainly done by myself. Ibrahim, Chiraag and I constructed the measurement setup and performed the experiments.

Chapter 2

Hybrid CMOS-Diamond Magnetometer

Solid-state quantum sensors are attracting broad interests thanks to a combination of excellent sensitivity and long-term stability. In particular, nitrogen-vacancy (NV) centers in diamond have emerged as an outstanding room-temperature quantum sensor platform for temperature [7], electric field [8] and magnetic field [9–15]. The capabilities of NV-based quantum metrology are based on its long spin coherence time [16] and its efficient optical interface for spin polarization and readout. NV center in diamond has also demonstrated outstanding imaging capabilities with sub-micron resolution. For example, imaging of magnetic structures and the magnetic fields generated by bacteria samples have been demonstrated (see Fig. 2-1). In addition, wide-field microscopy of superconducting materials [17] has also been achieved.

As a magnetometer, picotesla to sub-nanotesla sensitivity under ambient conditions has been achieved using NV centers in diamond [18–20]. However, conventional approaches for NV sensing involve bulky and discrete off-the-shelf instruments. These instruments are required for spin state manipulation and readout (see Section 2.1, and Section 2.2). The NV systems consist of a number of components, including: (1) microwave signal generator, and delivery interface to control the NV spin state. (2) optical filter to reject the pump laser and a photodetector for NV spin-dependent fluorescence measurement. (3) green pump laser. The current discrete realization of

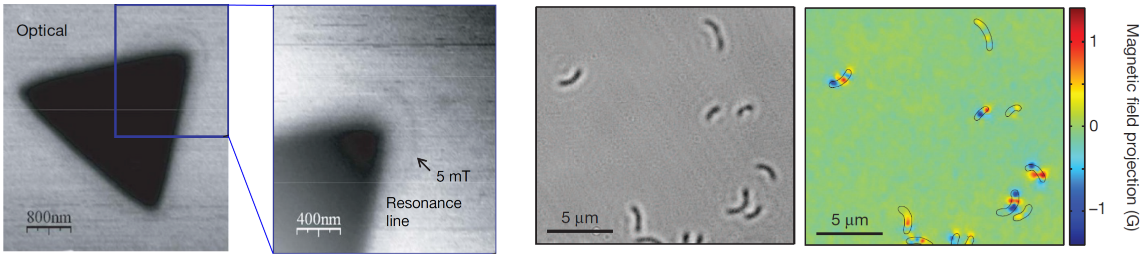

(a) (b)

Figure 2-1: (a) A magneto-optical image of the magnetic structure, recorded using a single NV center on the AFM tip [10]. (b) Optical image of bacteria living cells and the corresponding magnetic field image generated using NV centers [11].

the above-mentioned system limits practical applications and scalability.

A comparison of different magnetometer technologies with respect to their sensitivities and scale is shown in Fig. 2-2. The first group includes compact and low-cost integrated sensors such as Fluxgate [21, 22], Giant Magnetoresistive (GMR) [23, 24], and Hall-effect [25–27] sensors. However, the magnetic sensitivity of these sensors is limited to $\sim$nT/Hz$^{1/2}$. The second group includes highly-sensitive (pT//Hz$^{1/2}$ to even fT//Hz$^{1/2}$ levels), but bulky, and characterized by complicated and expensive packaging. Their miniaturization and low-cost implementation, although highly desired, are challenging. For instance, SQUIDs require the condition of cryogenic temperature [28–30], and

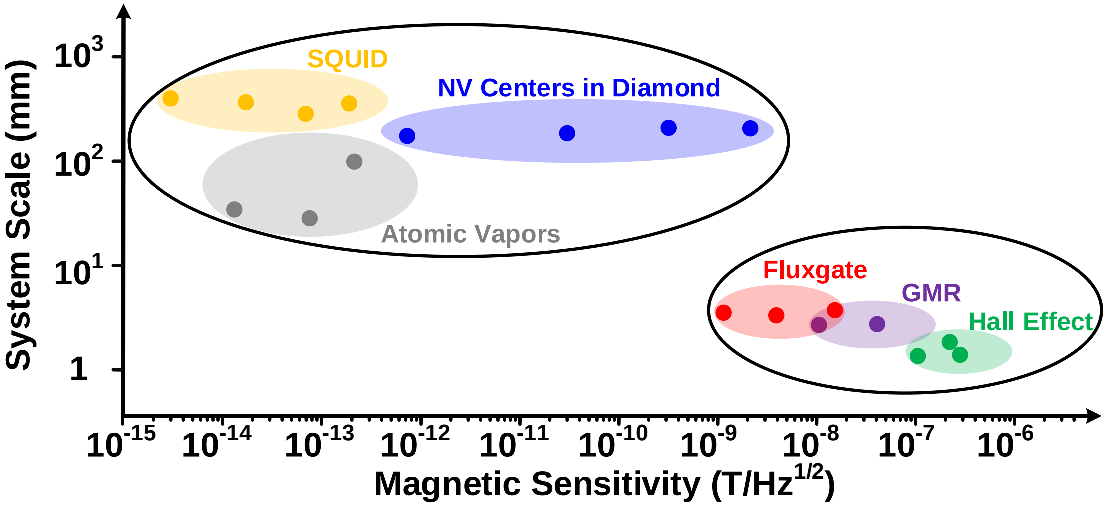

Figure 2-2: A comparison of different magnetometer technologies with respect to their sensitivities and scale.

vapor-cell sensors require advanced packaging of the reference gas [31–33]. On the other hand, the room-temperature operation condition and solid-state nature of NV centers [16, 18–20] lower the barriers for platform miniaturization to chip scale and hybrid integration of quantum materials (i.e. diamond with color centers). In this thesis, we discuss the details of our efforts in designing and implementing a scalable CMOS-Diamond sensor that can open up opportunities in compact and affordable sensors with unprecedented performance.

2.1 Overview of the Nitrogen Vacancy Center

The negatively-charged nitrogen-vacancy (NV) center in diamond consists of a nitrogen atom and a vacancy that substitute two adjacent carbon atoms in the diamond lattice as shown in Fig. 2-3. For a single crystalline diamond, NV centers have four possible orientations as shown in Fig. 2-3. The four orientations lay along the tetrahedral axes of the host diamond. Figure 2-4 also illustrates the NV energy level diagram. A spin magnetic triplet is formed at the ground state (^{3}A), consisting of a sub-level $|m_s = 0\rangle$ at its lowest energy and another two degenerate sub-levels $|m_s = \pm 1\rangle$ raised by ~2.87 GHz, which is temperature dependant. Under green light ($\lambda \approx 532$ nm) excitation, the NV center spins are stimulated to their excitation states (^{3}E in Fig. 2-4)

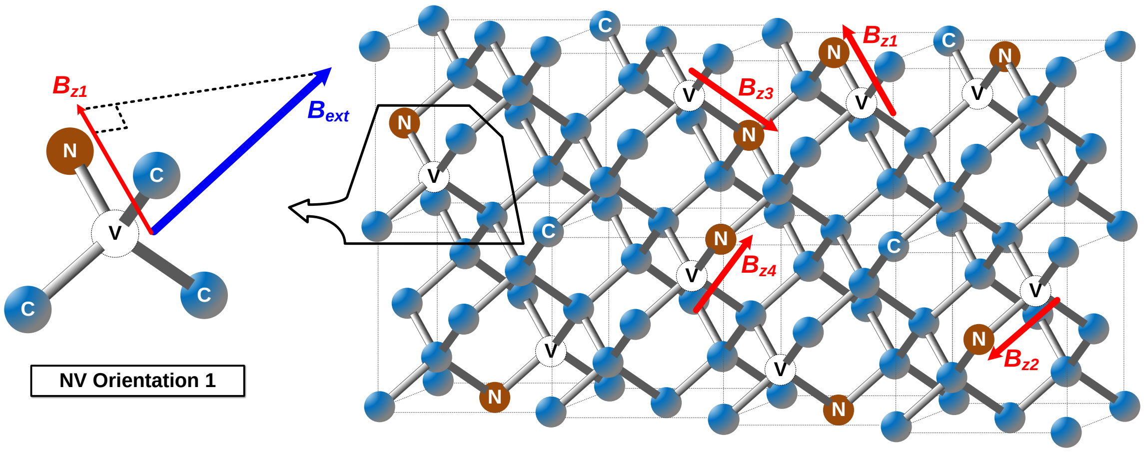

Figure 2-3: Nitrogen-vacancy centers in a diamond lattice. The blue, and red circles represent carbon, and nitrogen atoms respectively. The white circles represent the vacancy. The projections (B_{z1}, B_{z2}, B_{z3}, B_{z4}) of an external magnetic field B_{ext} along the four nitrogen-vacancy axes are also shown.

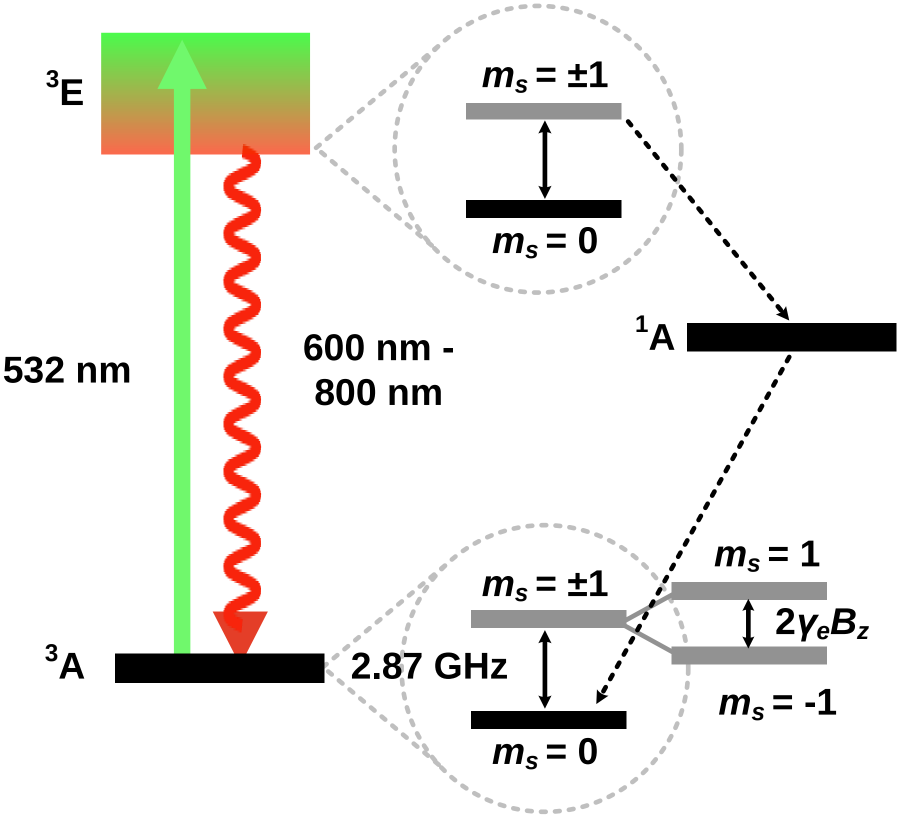

Figure 2-4: The energy-level diagram of a nitrogen-vacancy center in diamond.

and then relax back to the ground state (^{3}A). This is accompanied by spin dependent red fluorescence, which is a unique property for NV centers. The relaxation of the $|m_s = 0\rangle$ state is accompanied by a bright red fluorescence (λ≈600∼800 nm). In contrast, when the $|m_s = \pm1\rangle$ states are excited and relax back, they can undergo a non-radiative intersystem crossing into a metastable spin-singlet state (^{1}A in Fig. 2-4), and then transition into the $|m_s = 0\rangle$ ground level reducing the red fluorescence intensity. Therefore, by applying a microwave ($f_0 = \sim$2.87 GHz) and measuring the red fluorescence intensity of the NV center under green light excitation, the magnetic resonance of the NV can be detected (shown in Fig. 2-5). Since this resonance is detected optically, this is called optical detected magnetic resonance (ODMR) [10, 12]. As shown in Fig. 2-5, the amplitude of the dip at 2.87 GHz is called the contrast.

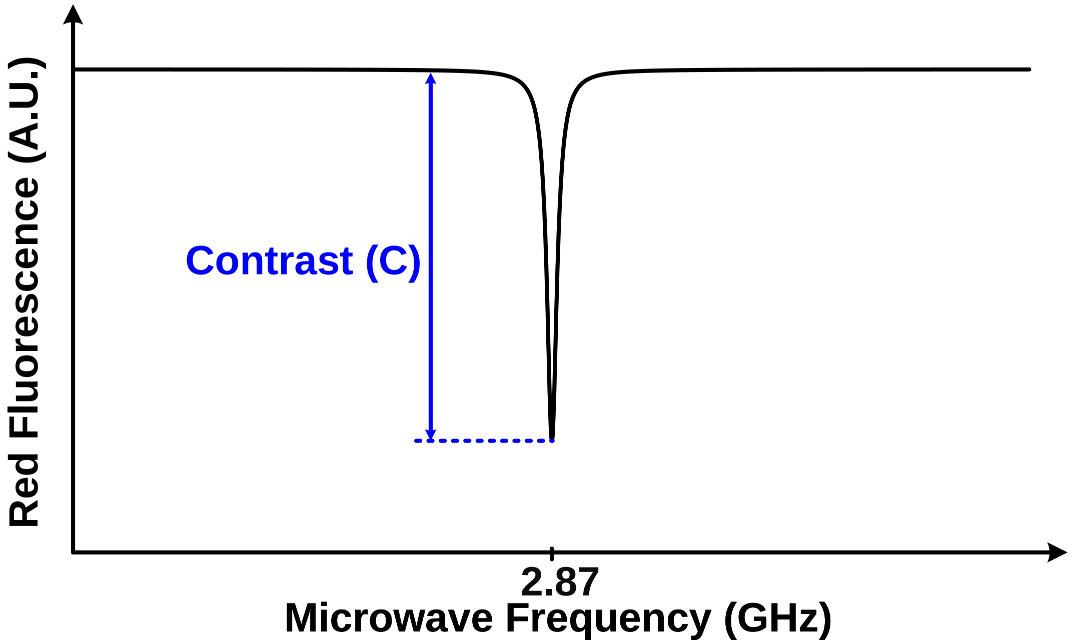

Figure 2-5: The red fluorescence intensity of the NV centers at varying microwave frequency (ODMR) under no external magnetic field bias.

2.2 DC Magnetic Field Measurements Using NV

The two unpaired electrons in each NV center form antiparallel spins in $|m_s = 0\rangle$ and parallel spins in $|m_s = \pm 1\rangle$. When an external magnetic field $\overrightarrow{B_{ext}}$ with a component $\overrightarrow{B_z}$ along the N-V axis (see Fig. 2-3) is applied, the $|m_s = \pm 1\rangle$ sub-levels are split apart (i.e. Zeeman effect). The $|m_s = +1\rangle$ level with the two spins anti-parallel with $\overrightarrow{B_z}$ has higher energy than that of the $|m_s = -1\rangle$ level, where the two spins are parallel with $\overrightarrow{B_z}$, The photon frequency Δf associated with such an energy gap is proportional to $|\overrightarrow{B_z}|$:

$$\Delta f = f_+ - f_- = 2\gamma_e |\overrightarrow{B_z}|, \tag{2.1}$$

where γ_e is the gyromagnetic ratio and equals to 28 GHz/T, and f_+ and f_- are the frequencies for the transitions from $|m_s = 0\rangle$ to $|m_s = +1\rangle$ and $|m_s = -1\rangle$, respectively. NV magnetometry is performed by determining f_+ and f_- via ODMR. We use Δf to derive $\overrightarrow{B_z}$. Through detecting the magnetic resonance using ODMR, a static or slowly-varying magnetic fields $\overrightarrow{B_z}$, can be determined by sweeping a microwave frequency f_0

around 2.87 GHz and monitoring the average intensity. The observed resonances of Fig. 2-6 are f_+ and f_-, which give $\overrightarrow{B_z}$. Since NV centers have four possible orientations in a single crystalline diamond as discussed in Section 2.1, this leads to four pairs of splitting in a single ODMR measurement (Fig. 2-6). The magnetometer based on this principle, therefore, has vector-field measurement capability by monitoring the different magnetic field projections and reconstructing $\overrightarrow{B_{ext}}$. That is advantageous over conventional fluxgate and Hall-based sensors [21, 27], where three devices in x- y- z- axes are needed for vector detection.

An NV-center vector magnetometer normally has a static bias field to create the aforementioned four ODMR spectral splittings (Fig. 2-6). The electronics of the magnetometer then tracks the shifts of f_+ and f_-, so as to measure the variation of the externally applied magnetic field. This can be done by recording the additional change of the sensor output red fluorescence intensity measurements around each dip in the magnetic resonance curve. Note this intensity change is caused by the shift of each resonance frequency Δf_i due to the projection of the added field on the

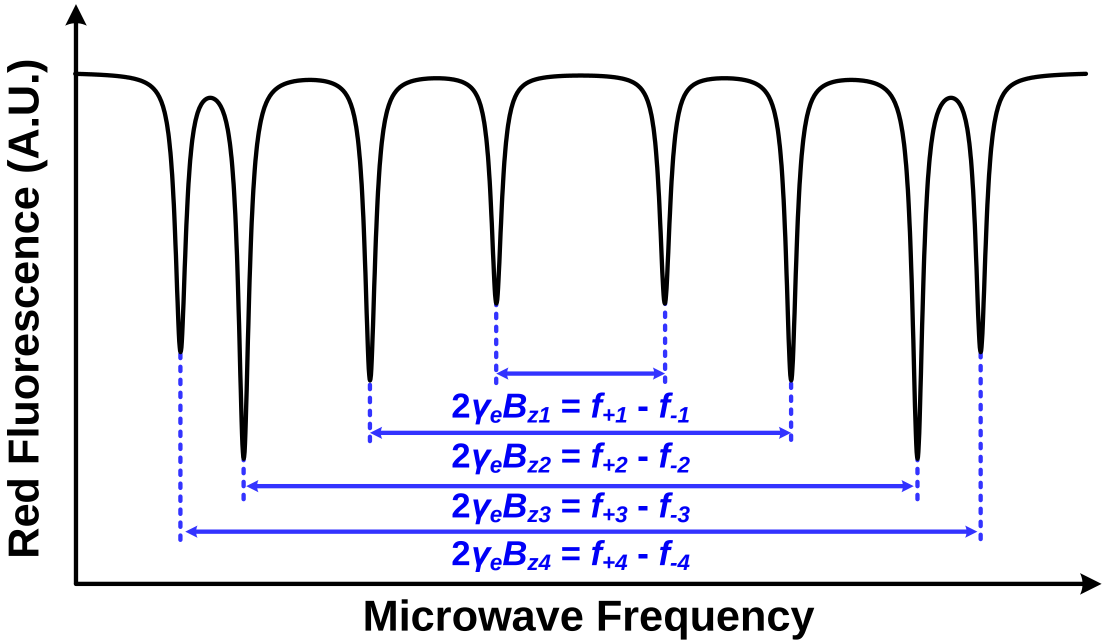

Figure 2-6: The red fluorescence intensity of the NV center at varying microwave frequency (ODMR) under an external magnetic field bias with projections along the four N-V axes.

associated NV-center axis ΔB_{zi} (to be measured) on top of the bias static field. The sensitivity obtained from an ODMR spectrum as shown in Fig. 2-6 is determined by two factors: the linewidth and the signal-to-noise ratio (SNR) of each transition curve. The SNR is proportional to the contrast of the experiment and inversely proportional to the minimum detectable intensity signal. In Section 2.7, and Section 3.2, more details and analytical expressions of the sensitivity are provided.

2.3 Chip-Scale CMOS-Diamond Hybrid Sensing Architecture

In the proposed CMOS-diamond sensing architecture, we use standard CMOS technology to implement most of the components required to manipulate and readout the spin states of NV centers in diamond. A diamond layer full of NV centers is attached on the top of the chip. A green laser source is used for optical excitation. As shown in Fig. 2-7, a microwave signal generator, switches and current drivers that feed a microwave coupling structure are needed to manipulate the spin state of the NV centers. The microwave signal generator has to operate over a sufficient range (i.e. 2.6 GHz to 3.2 GHz) to enable the measurements of the ODMR curve. The microwave delivery structure which can be an inductor has to generate a strong homogeneous microwave field to increase the contrast of the ODMR curve (i.e. signal) and drive all the NV centers in the ensemble with the same strength.

In order to detect the spin dependent red fluorescence a photodiode on the chip is integrated below the microwave delivery structure. However, the absorption probability of the NV to green light is very low, which means the majority of the green light transmits into the on-chip photodiode. This hurts the overall noise of the experiment, hence the sensitivity. This is due to two factors: (i) the intensity fluctuation of the green light. (ii) the shot noise due to the large output DC current which can be given by Eq. 2.2:

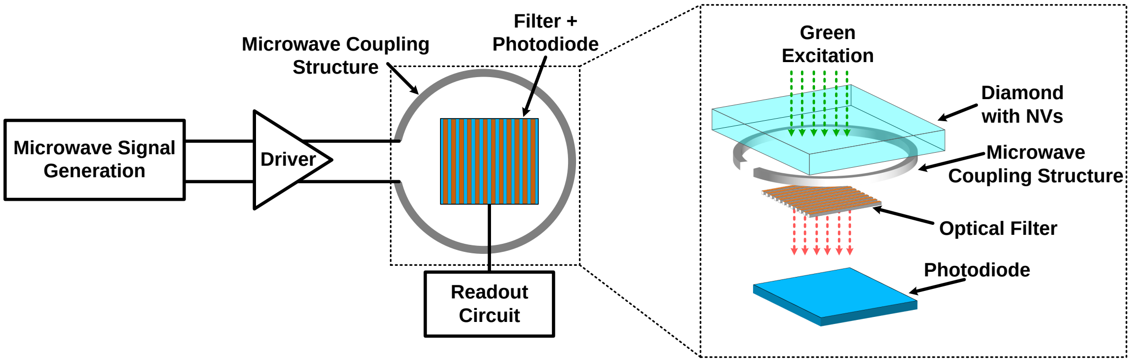

Figure 2-7: The basic schematic of the proposed CMOS-Diamond sensing architecture.

$$\bar{i_n^2} = 2qI_D\Delta f = 2q(I_g + I_r)\Delta f. \tag{2.2}$$

where, Δf is the noise bandwidth, and I_D is the DC current detected by the photodiode. I_g, and I_r are the green and red current portions detected by the photodiodes. This green background also hurts the contrast of the ODMR curve, which consequently hurts the sensitivity. Therefore an optical filter is needed to suppress the green excitation light and pass the red fluorescence. This filter should be added between the diamond and the photodiode. We choose to integrate this filter on the same chip pushing towards a monolithic solution using standard CMOS processes.

2.4 CMOS-Diamond Hybrid Quantum Magnetometer

Figure 2-8 shows the system schematic of the first prototype of the hybrid CMOS-diamond quantum magnetometer. This chip, using TSMC 65 nm CMOS technology, integrates most of the critical components for the ODMR operation. Shown in Fig. 2-8, an on-chip ~ 2.87 GHz voltage-controlled oscillator (VCO) is phase-locked to an external reference with a tunable frequency. Through a differential current driver and a loop inductor, the circuit applies a vertical AC magnetic field to excite the

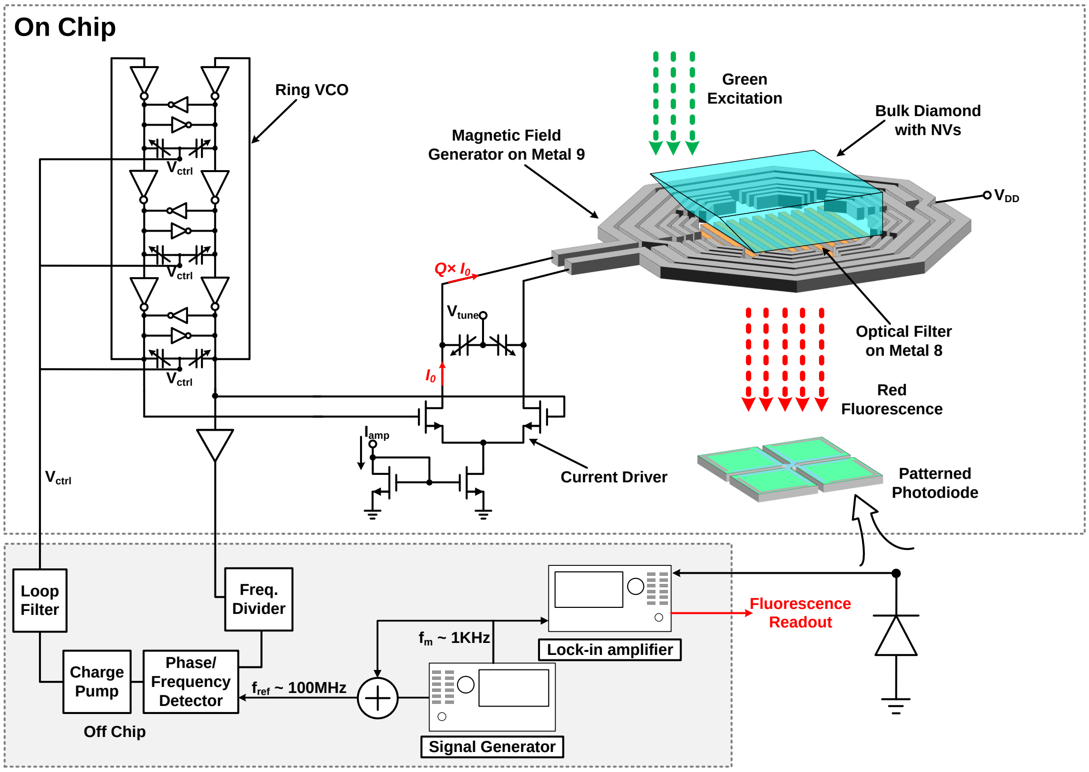

Figure 2-8: The schematic of the first CMOS-diamond quantum magnetometer with a single crystalline slab on the top of the chip.

$|m_s = \pm 1\rangle$ ground levels of NV centers inside a slab of single crystalline diamond. The diamond is excited from above with a green light, and the red fluorescence is detected by a p+/n-well/p-sub photodiode placed under the loop inductor. The diode is partitioned into smaller portions in shunt, in order to prevent the induction of large eddy current from the inductor (hence RF loss). As described in Section 2.3 the majority of the green light is not absorbed by the diamond, but transmits into the chip. A plasmonic nano-photonic filter, using a grating of the CMOS interconnect metal (Metal 8), is implemented above the photodiode (Fig. 2-8). The detailed design of the filter is provided in Section 2.6.

2.5 On-chip Microwave generation

The ground-state spin transitions are driven by the on-chip generated microwave fields. Figure 2-9 shows the circuitry for on-chip microwave generation and delivery. This circuitry is composed of a phase-locked loop (PLL), a current driver, and a resonant loop inductor. The PLL generates the microwave sweep signal from 2.6 GHz to 3.1 GHz required for the ODMR experiment. The main component of this loop is an on-chip voltage-controlled ring oscillator (VCO) with 3 differential inverter stages. The usage of a ring VCO [34] avoids any large-size inductor and minimizes the cross-talk between the oscillator and the microwave inductor which drives the NV ensemble. The mutual-locking inverter pair (e.g., INV$_2$ in Fig. 2-9 forms a latch and ensures the differential phases between the left and right branches of the VCO. Inside each inverter stage of the on-chip ring VCO in Fig. 2-9 (e.g., INV$_1$), the sizes of the NMOS and PMOS (gate width/gate length) are 24 μm/280 nm and 54 μm/280 nm, respectively. Inside each latch inverter (e.g., INV$_2$ in Fig. 2-9), the NMOS and PMOS sizes are 5.2 μm/280 nm and 12 μm/280 nm, respectively. The frequency tunability of the oscillator is realized via 3 pairs of MOS variable capacitors (e.g., C$_{VCO}$ in Fig. 2-9, of which the capacitance changes from 22 fF to 75 fF when the PLL control voltage V_{ctrl} varies from 0 to 5 V. The simulated and the measured VCO tuning curves are shown in Fig. 2-10. The curves show very good agreement between them. The VCO gain is ∼180 MHz/V. The entire phase-locked loop is closed with off-chip components to

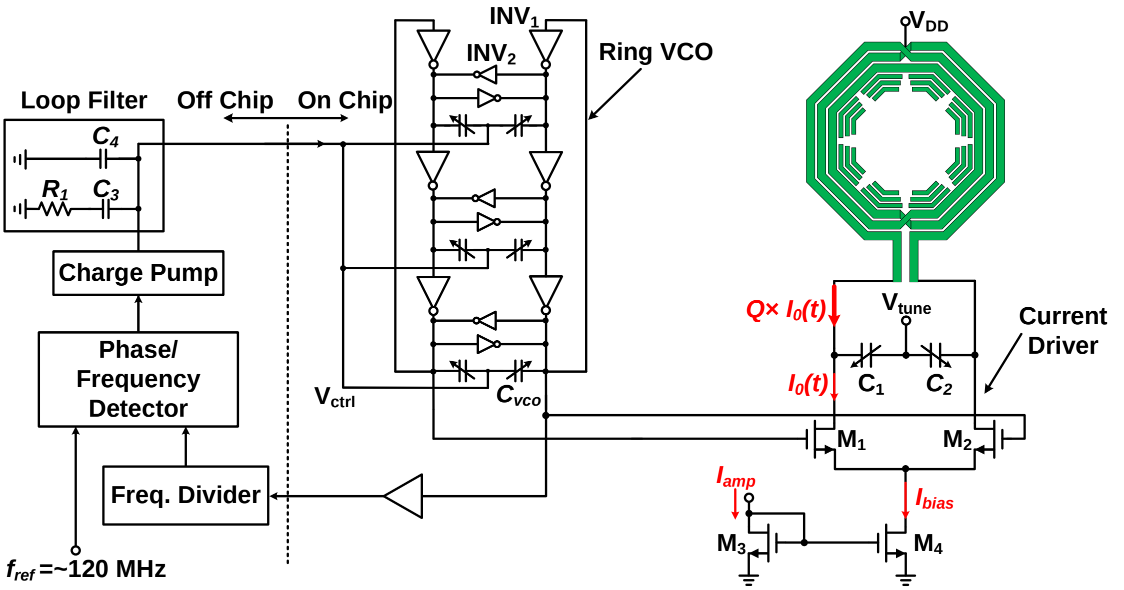

Figure 2-9: Schematic of the microwave generation circuitry.

enhance the stability and decrease the phase noise of the signal. The loop filter of the PLL is a typical second-order low-pass filter and the values of the components shown in Fig. 2-9 are R_1=0.4 kΩ, C_3=4.5 nF and C_4=150 pF.

The microwave fields are delivered to the NV ensemble through the loop inductor (Fig. 2-9) implemented on the top-most copper layer (Metal 9). To efficiently deliver the microwave field, the loop inductor and a pair of shunt capacitors (C_1 and C_2 in Fig. 2-9) form a resonating load for the current driver. C_1 and C_2 are MOS variable capacitors with capacitance ranging from 312 fF to 1.4 pF. By electrically tuning them via V_{tune}, the load resonates near D_{gs} as shown in Fig. 2-11. This current driver fed by the output of the ring VCO produces oscillating current in the inductor at the VCO microwave frequency. In Fig. 2-9, the sizes (gate width/gate length) of transistors $M_1 \sim M_4$ are 80 μm/280 nm, 80 μm/280 nm, 72 μm/500 nm and 720 μm/500 nm, respectively. To improve the performance of this inductor for advanced NV sensing protocols [35, 36], we need to increase the applied microwave field amplitude. The amplitude is enhanced by a factor Q compared to the driver DC bias current (I_{bias} $\approx$ 5 mA from a 2.5 V power supply), where Q ($\sim$ 15) is the quality factor of the

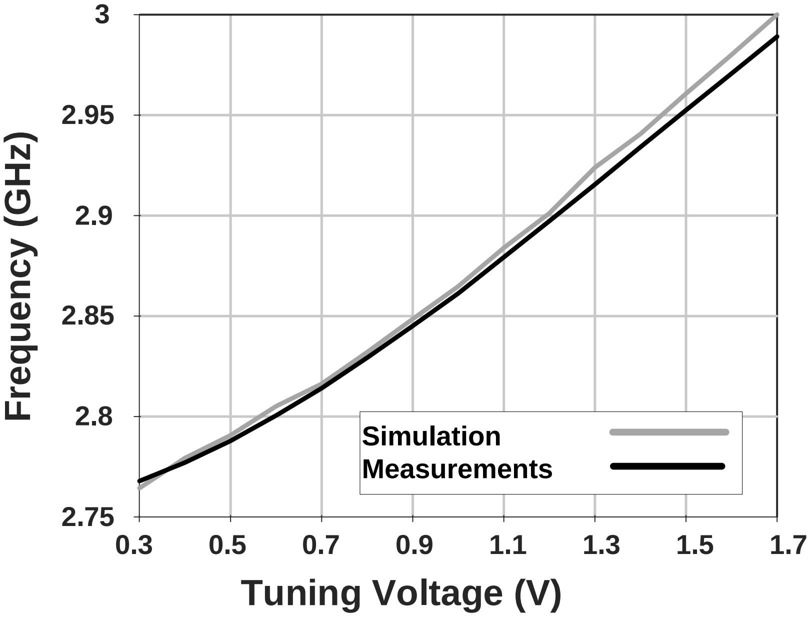

Figure 2-10: The simulated and measured tuning curve of the on-chip ring VCO.

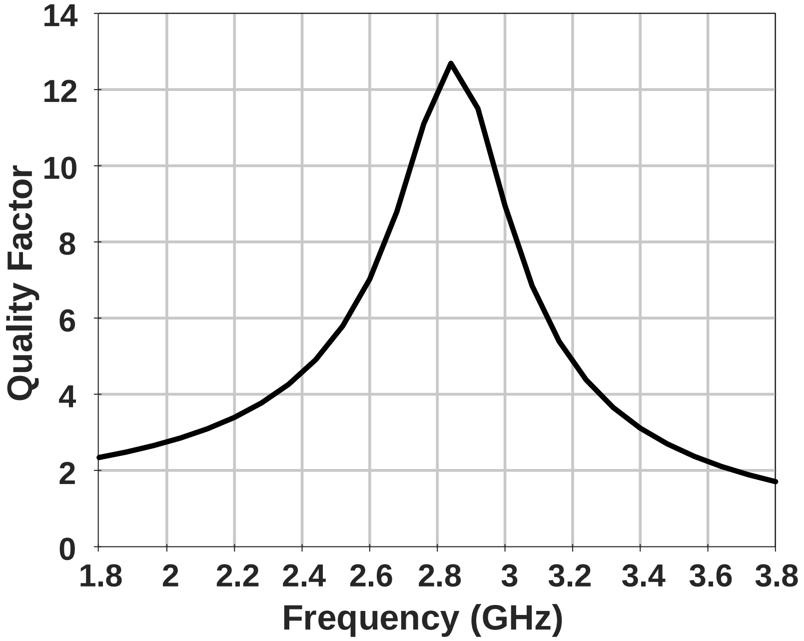

Figure 2-11: The amplitude of the AC current flowing in the inductor as a function of frequency. The plot shows a resonance behavior at 2.87 GHz.

inductor. In addition, a three-turn loop is used to multiply the microwave field strength. Overall, we have 25× enhanced microwave field strength compared to a non-resonant single turn loop. The High-frequency electromagnetic fields simulations (HFSS) [37] result is plotted in Fig. 2-12. The magnetic field amplitude is plotted as a function of distance from the inductor center

The advanced NV sensing protocols mentioned above also require highly uniform microwave fields over the excitation volume. To achieve this, three capacitive parasitic loops are inserted. The radius of these loops is tailored, so that their opposite induced field homogenizes the overall generated field. Another degree of freedom is the capacitive gaps in the parasitic loops. This controls the amount of current flowing in these loops. A comparison between the field distribution of a simple one turn loop and another one with the capacitively loaded parasitic loop as a function of the distance from the center of the inductor is shown in Fig. 2-13. This loading enhances the homogeneity of the field without sacrificing the field magnitude. The two important parameters (i.e., the parasitic loop radius and the capacitive gap) for

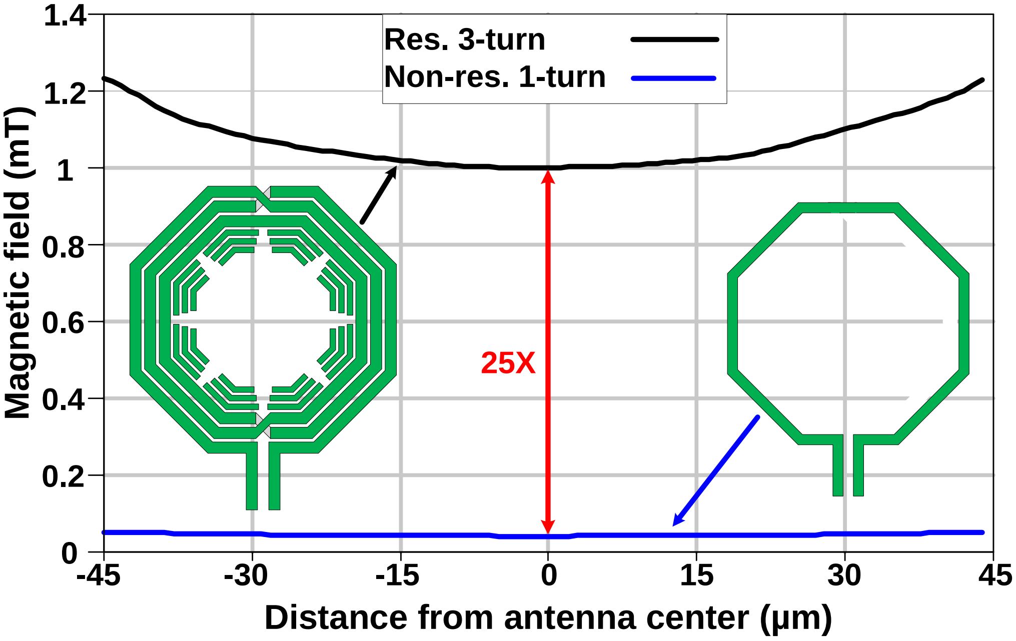

Figure 2-12: The simulated magnetic field profiles as a function of distance from the center of the proposed resonant inductor and a non-resonant one.

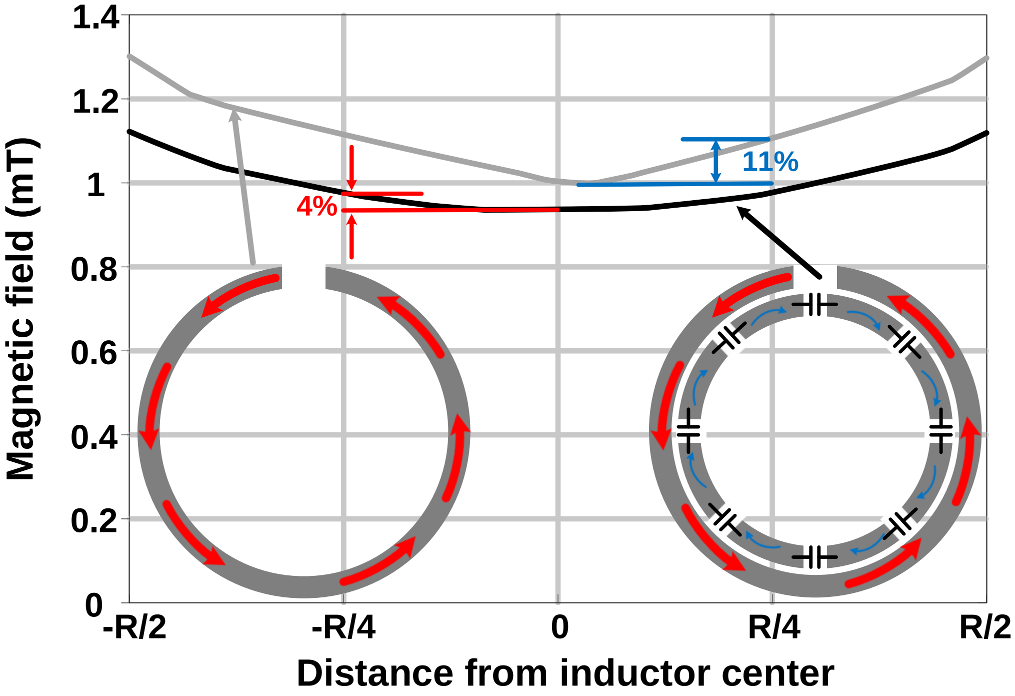

Figure 2-13: The simulated magnetic field profiles as a function of distance from the inductor center with and without the capacitive parasitic loop.

the three parasitic loops are optimized to achieve > 95% uniformity. The detailed dimensions of the final loop inductor implemented in the chip is shown in Fig. 2-14. The loop outer diameter is 236 µm, and exhibits an inductance of ∼3 nH.

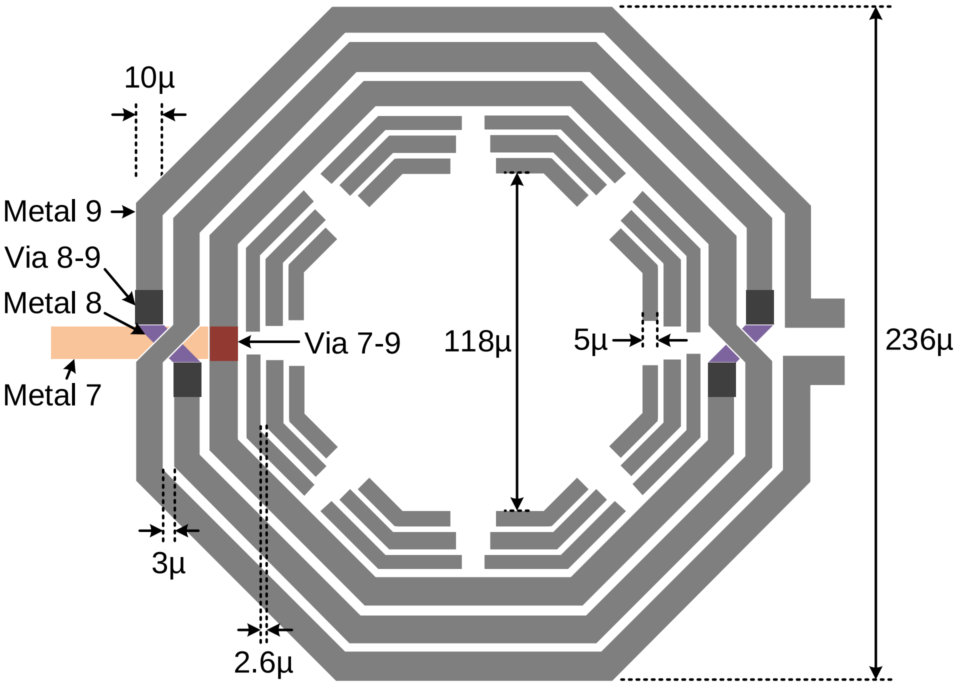

Figure 2-14: The layout of the 3-turn on-chip inductor with parasitic capacitive loops.

2.6 On-chip Optical Detection

The NV spin transitions are detected using an on-chip photodetector. A CMOS-compatible periodic metal-dielectric structure in the Metal 8 interconnect layer (the grating pitch, t equals 800 nm) filters green pump light (Fig. 2-15) [38, 39]. The incident light couples to the surface plasmon polariton (SPP) at the metal-dielectric interface, where it undergoes frequency-dependent Ohmic loss [40, 41]. Therefore green light is attenuated more than red light, achieving a finite green to red rejection. As shown in Fig. 2-15 each slit is considered as a parallel plate waveguide transmitting light inside a dielectric (relative permittivity $\epsilon_d \approx 1.5$) in the z- direction. The incoming light is modeled as a plane wave with a transverse electrical field E_x and a propagation constant $k_0 = \omega\sqrt{\epsilon_d}/c$ (c is the speed of light in vacuum). Then, it is coupled to the

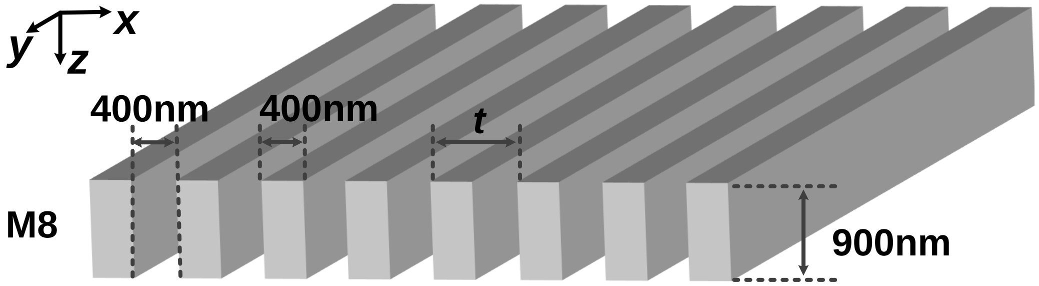

Figure 2-15: The layout of single-layer plasmonic grating filter implemented on Metal 8 [38].

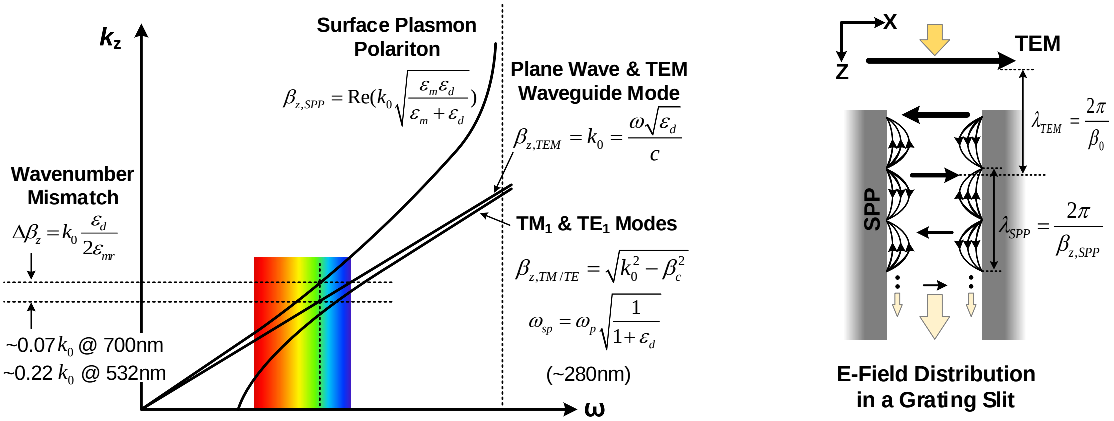

(a) (b)

Figure 2-16: TEM and SPP modes inside a grating slit (modeled as a parallel-metal-plate waveguide): (a) dispersion relationships and (b) short-distance coupling.

TEM mode of the parallel-plate waveguides, which has identical propagation constant k_0 (see Fig. 2-16a). As the propagating wave interacts with the metal, the surface plasmon polariton (SPP) mode at the metal-dielectric interface is excited. Note that the dispersion relation of SPP mode is:

$$k_{z,SPP} = \beta_{SPP} + j\alpha_{SPP} = k_0\sqrt{\frac{\epsilon_m}{\epsilon_m + \epsilon_d}}. \tag{2.3}$$

In Eq. 2.3, the permittivity ($\epsilon_m{=}\epsilon_{mr} + i\epsilon_{mi}$) of the metal (copper in our case) has a negative real part, which leads to $\beta_{SPP} > k_0$. Although coupling from the TEM waveguide mode and the SPP mode generally does not occur[1], it still does in this case. That is because, by examining the value of β_{SPP} in Eq. 2.3:

$$\beta_{SPP} = \mathrm{Re}(k_0\sqrt{\frac{\epsilon_m}{\epsilon_m + \epsilon_d}}) \approx k_0(1 - \frac{\epsilon_d}{2\epsilon_{mr}}), \tag{2.4}$$

we see that since $|\epsilon_{mr}|$ remains large, the relative mismatch between the β_{SPP} and β_{TEM}=k_0, namely $\epsilon_d/2\epsilon_{mr}$ in Eq. 2.4, are ∼0.07 for red (700 nm) and ∼0.22 for green (532 nm) (see Fig. 2-16a). These calculations are based on the Drude-Brendel-Bormann model [42, 43]. Along the vertical propagation distance of the grating (i.e. the M8 grating thickness d=900 nm, or $2\lambda_{red}$=$2.5\lambda_{green}$ in dielectric), the accumulated phase mismatch is:

$$\Delta\phi = 2\pi\frac{\epsilon_d}{2\epsilon_{mr}}\frac{d}{\lambda}, \tag{2.5}$$

or $\sim 50^o$ (red) and $\sim 180^o$ (green), respectively. Therefore, for red light, constructive coupling from the TEM mode to SPP mode still occurs within the single-layer grating. For green light, although phase mismatch appears to be large, the coupling is still effective in the M8 slit due to the large SPP loss; and when the TEM wave reaches the bottom half of the slit, its power is already heavily depleted.

To quantify the loss of the SPP mode using the real and imaginary parts of the dielectric constant of copper shown in Fig. 2-17, the attenuation factor α_{SPP} is derived in Eq. 2.6:

$$\alpha_{SPP} = \mathrm{Im}(k_0\sqrt{\frac{\epsilon_m}{\epsilon_m + \epsilon_d}}) \approx k_0\frac{\epsilon_d\epsilon_{mi}}{2\epsilon_{mr}^2}, \tag{2.6}$$

where ϵ_m=$\epsilon_{mr} + j\epsilon_{mi}$ is the permittivity of the metal, which is copper for M8 in the technology we use. This exhibits large difference between red (α_{SPP}≈$0.01k_0$) and green (α_{SPP}≈$0.26k_0$). That is due to not only the decreased ϵ_{mr} of copper in green, which is normal plasmonic property described by the Drude model, but also an

---

[1] Normally, dedicated material/geometrical configurations, such as the Otto and Kretschmann-Raether configurations, are needed to enable the excitation of the SPP mode.

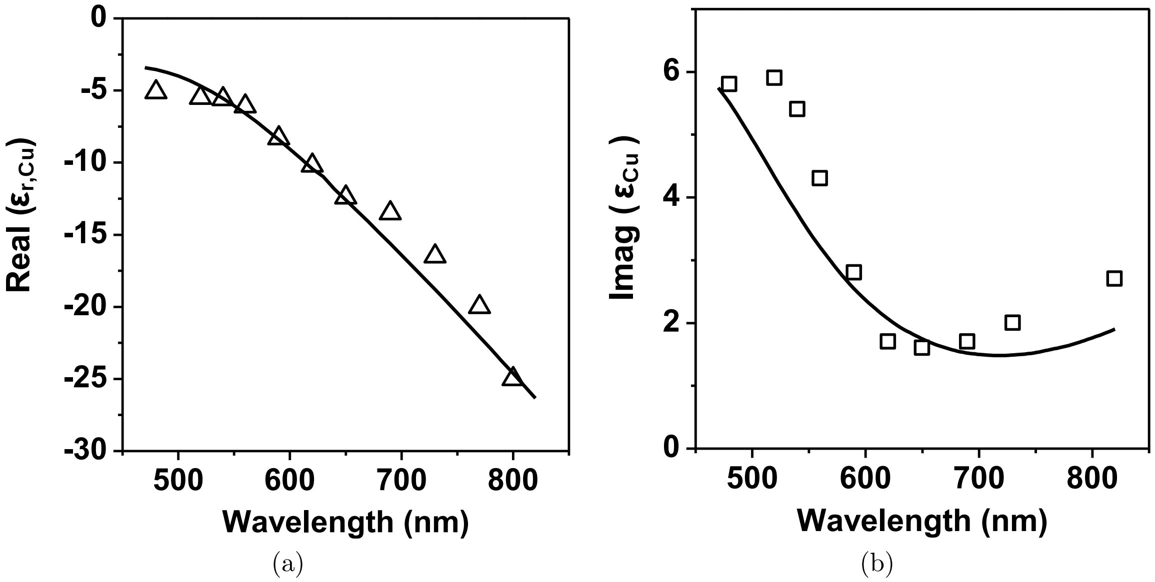

Figure 2-17: The (a) real and (b) imaginary parts of the relative dielectric constant of copper. The calculated plots (solid lines) are based on the Drude-Brendel-Bormann model. The measured data (triangles and squares) are from [42, 43].

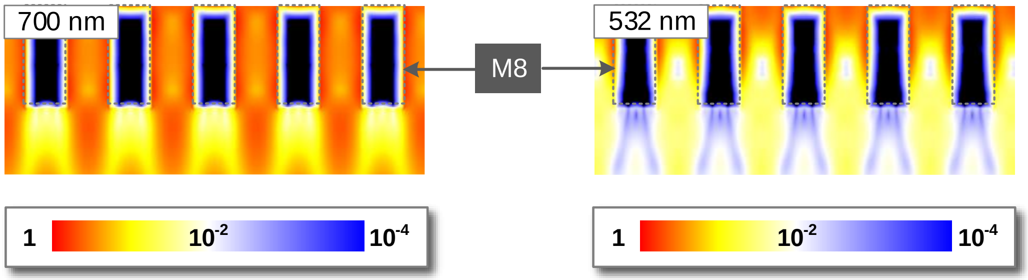

Figure 2-18: The simulated FDTD Poynting vector profile $|P|=|E \times H|$ for single-layer grating in M8.

abnormal dispersion with increased ϵ_{mi}, which is caused by interband transitions of bound electrons excited by the photons.

The simulated Lumerical FDTD [44] transmission through the filter at the wavelengths of 532 nm (green) and 700 nm (red) are shown in Fig. 2-18. The measured green-to-red suppression ratio due to this filter (d=900 nm) is 10 dB. Increasing the slit thickness by stacking more grating layers (in M7, M6...) is expected to further increase the suppression of the green light [41]. However, that causes degradation of red-light transmission due to the scattering at the side walls formed by the sparse inter-layer via pillars.

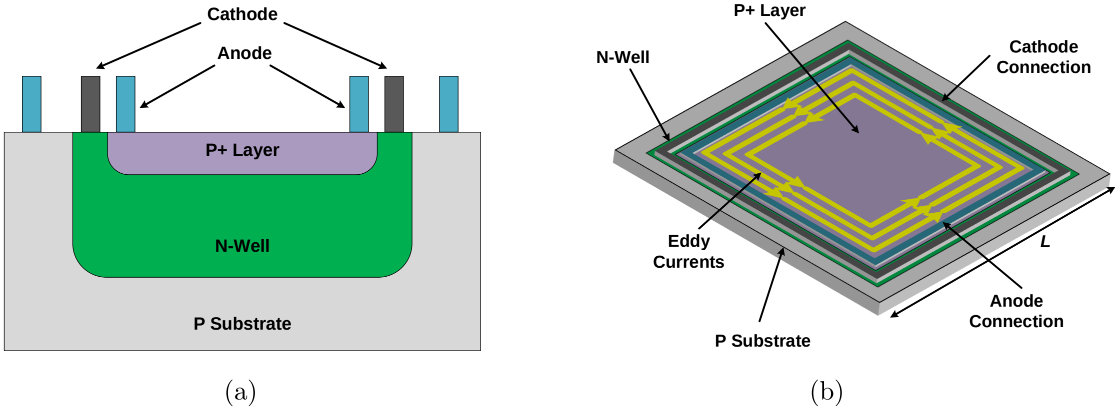

Figure 2-19: (a) The cross section of the P+/N-well/P-sub (b) unpatterned photodiode layout with eddy current loops in the active area and possibly the anode and cathode connection.

To detect the NV-emitted red fluorescence, a P+/N-well/P-sub photodiode as shown in Fig. 2-19a is used. This specific configuration is preferable for long wavelength detection [45]. Since we place the photodiode with its conductive layers below the inductor (Fig. 2-8), large eddy currents near 2.87 GHz can be induced if we use a conventional unpatterned physical layout as shown in Fig. 2-19b. This reduces the quality factor of the inductor, resulting in microwave amplitude reduction. By dividing the photodiode area into four subareas (2×2 array) as shown in Fig. 2-20a, this eddy current is reduced by half as shown in Eq. 2.7, and Eq. 2.8:

$$P_{\text{eddy}} \propto \frac{(d\phi(t)/dt)^2}{R} \propto \frac{L^4\left(\frac{dB}{dt}\right)^2}{L} \propto L^3\left(\frac{dB}{dt}\right)^2 \tag{2.7}$$

$$\frac{P_{\text{eddy}\,Prop}}{P_{\text{eddy}\,Conv}} = \frac{4(\frac{L}{2})^3}{L^3} = \frac{1}{2} \tag{2.8}$$

where, P_{eddy} is the eddy current loss and L is the side length of the photodiode. $\phi(t)$ and B are the magnetic flux and the magnetic field generated by the loop inductor in Metal 9, respectively. t is the time and R is the active area resistance. Similarly, by dividing the photodiode active area into N×N subareas, the eddy current loss is reduced by 1/N. Furthermore, the anode/cathode connectors are arranged in a radial way that is similar to patterned ground shielding used in CMOS inductors [46]. This arrangement (Shown in Fig. 2-20b, and Fig. 2-20c) avoids any closed loops, which

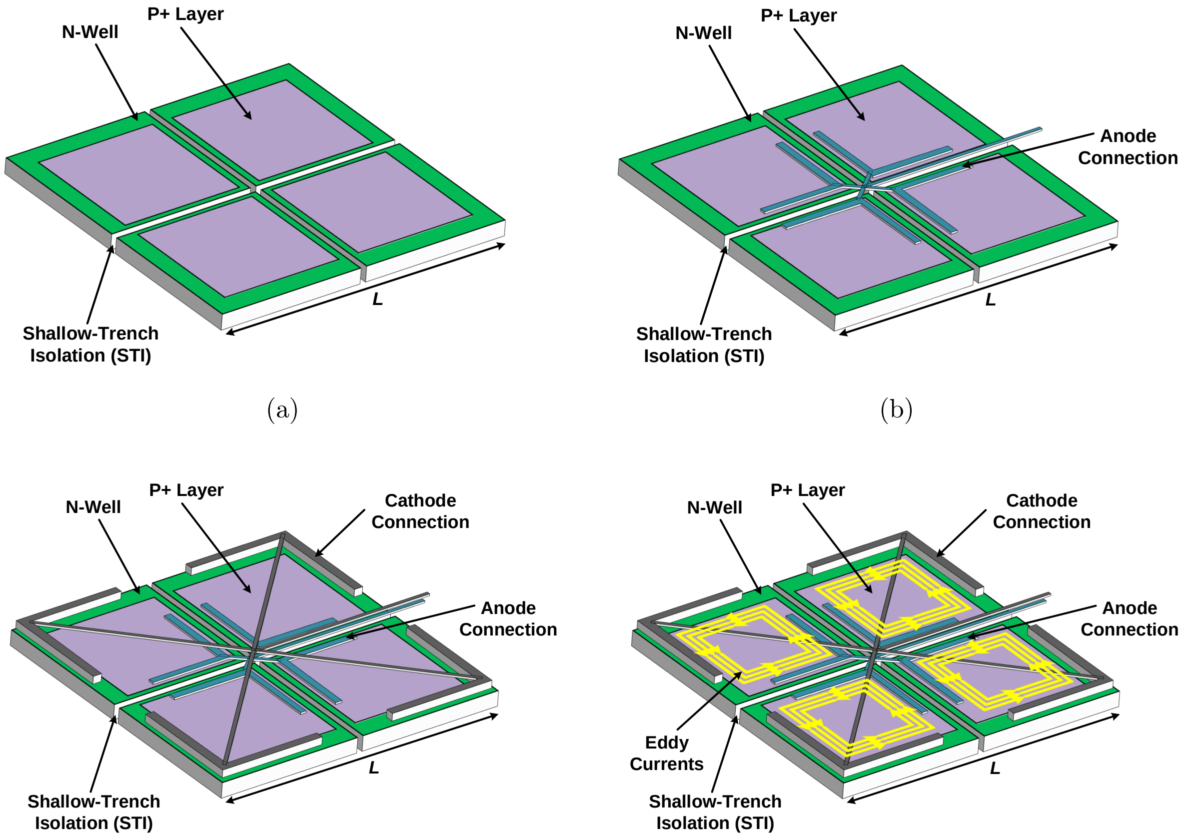

(a) (b)

(c) (d)

Figure 2-20: The proposed patterned photodiode layout (a) 2×2 active area layout (b) the radially connected anode connection that prevents any closed loops implemented in M1. (c) the full layout with cathode connection in M2 added. (d) the full layout with eddy current loops in the patterned active area only.

helps to cut the eddy current that may flow in the metallic connections. As shown in Fig. 2-20d the eddy current loops flow only in the patterned active area only. The photodiode has a measured responsivity of 0.23 A/W at the wavelength of 532 nm, which corresponds to a quantum efficiency of 0.54.

2.7 Experimental Results

As mentioned in Section 2.4, a slab of single crystalline diamond is placed on the top of the chip on the sensing area (see Fig. 2-21a) including the on-chip inductor, the optical filter and the photodiode. A 500 µm × 500 µm × 500 µm diamond slab is

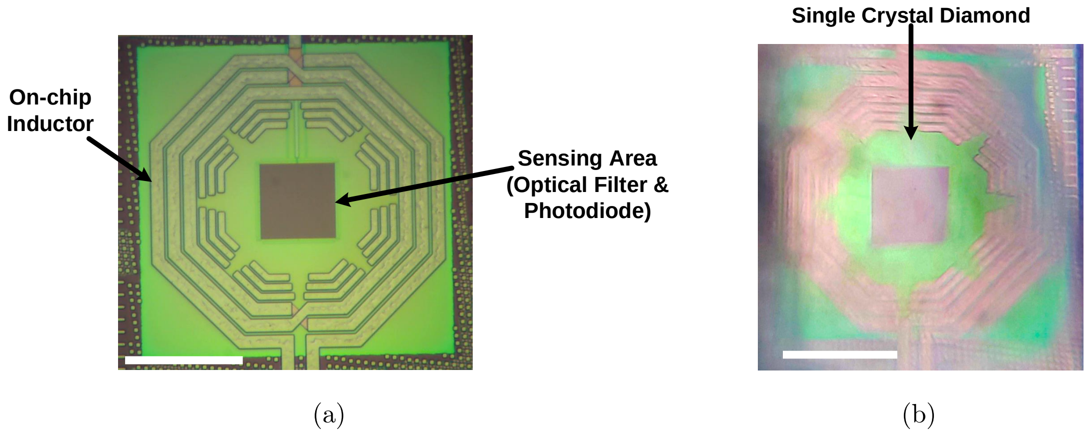

(a) (b)

Figure 2-21: Top-view micrograph of (a) the fabricated CMOS chip sensing area including the inductor, optical filter, and photodiode, (b) the sensing area covered by the single crystalline diamond slab. Scale bar is 100 µm.

picked and placed on top of the chip under a microscope. The diamond is a single crystalline CVD-grown diamond from Element 6. It is electronically irradiated with a dosage of 10^{18} e^{-}/cm^{2} at 1 MeV, and then annealed for 2 hours at 850°C. This produces an estimated NV centers density of ~ 0.01 ppm. Immersion oil is used to adhere the diamond slab to the chip. By bridging the difference of the refractive index, the oil also minimizes the fluorescence loss. A 45° cut is introduced in the diamond's corner as shown in Fig. 2-8 to direct the vertical incident green laser horizontally to further enhance the overall green rejection ratio. Figure 2-21b shows an optical image of the diamond slab on top of the chip. The CMOS chip is then wire-bonded on a PCB board. The PCB photo with the chip micrograph are shown in Fig. 2-22.

We start with measuring the ODMR by detecting the NV spin-dependent red fluorescence using the on-chip photodiode. Figure 2-23 shows the test setup of the experiment. A linearly polarized DPSS green laser beam (500 mW, $\lambda = 532$ nm, Verdi G2, Coherent) is delivered to the diamond through a telescope of $f_1 = 35$ mm and $f_2 = 150$ mm. The beam diameter incident on the diamond is ~500 µm. The lens system used is placed far from the sample for experimental convenience, though it is important to note that the lens system could be avoided if the laser was positioned nearby the CMOS chip or even replaced with other options as discussed in Chapter 5.

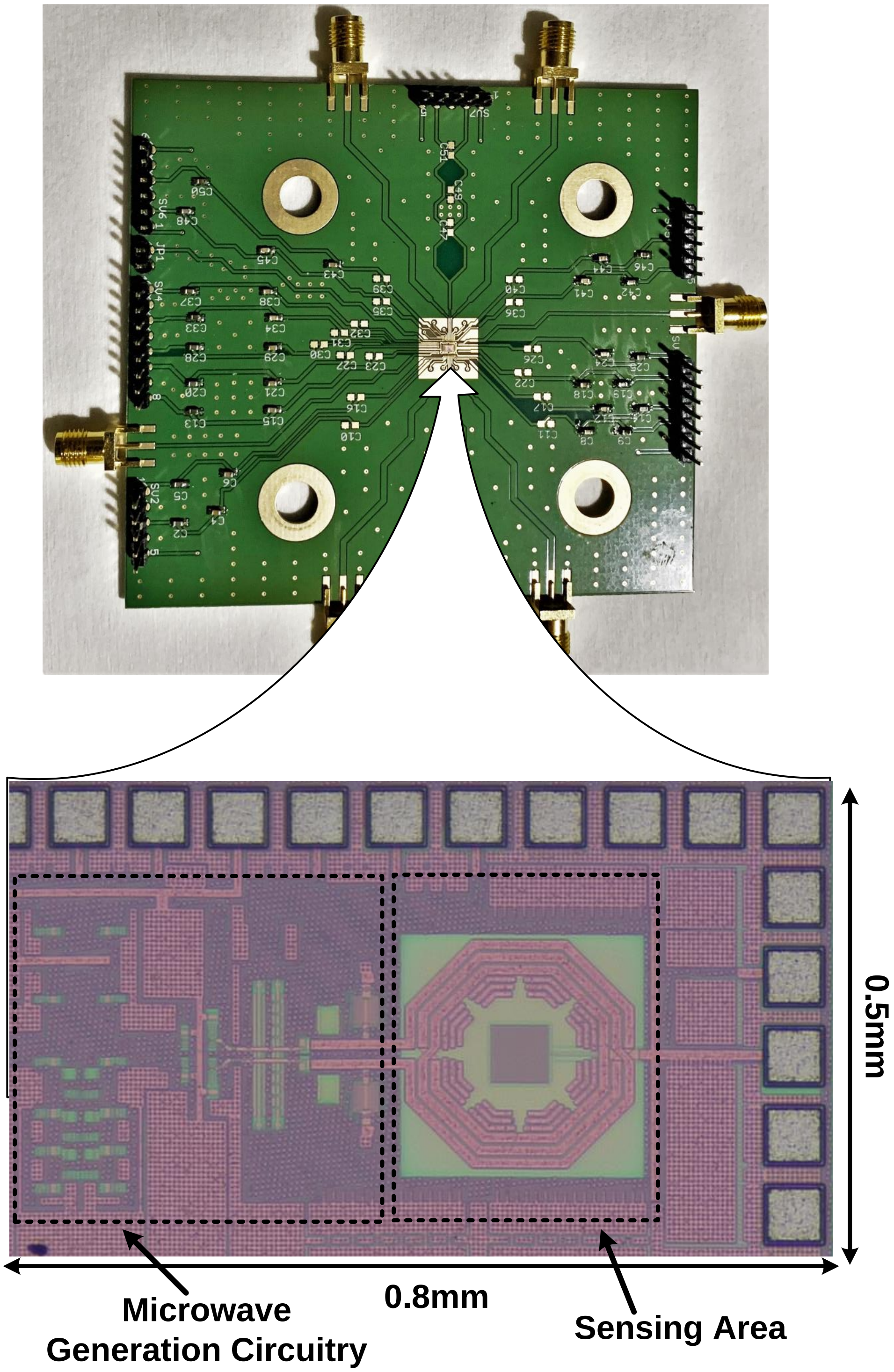

Figure 2-22: Optical micrograph of the CMOS chip (bottom) and photo of the printed circuit board for testing (top).

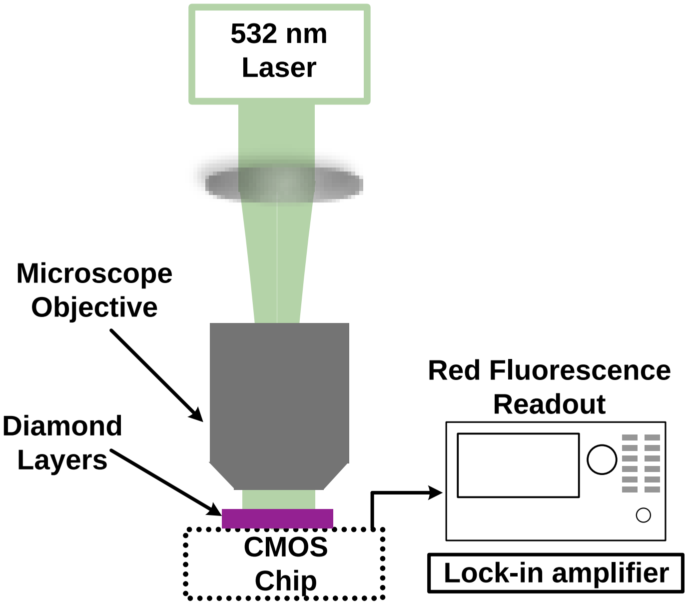

Figure 2-23: The experimental setup of the ODMR experiment using on-chip photodiode.

The microwave frequency is swept to address the NV center and excite the magnetic resonance. This is done by changing the reference frequency of the PLL loop through an external signal generator ($\sim$ 120 MHz). The VCO output signal is frequency-divided by 24 and then compared to the reference signal provided by an external signal source (HP ESG-D4000A). In addition, a lock-in amplifier is used to detect the photodiode signal as shown in Fig. 2-8. A half-wave plate rotates the polarization of the laser beam to maximize the laser absorption through the periodic metal/dielectric structure in the Metal 8 layer. Since the filter rejection is still only 10 dB, there is a huge background green signal that complicates the measurements. A lock-in detection technique is used to detect the NV red fluorescence. The green laser beam continuously excites the NV ensemble, and the frequency-modulated (FM) microwave fields (f_m = 1.5 kHz and modulation depth of 6 MHz) drive the NV electron spin transition (Fig. 2-8). The spin-dependent fluorescence produces photo-current within the on-chip photodiode. Then, the modulated photo-current is detected through the voltage drop across a 50 Ω resistor at f_m with a Stanford Research Systems lock-in amplifier (SR865A). The experiment is done with one second integration time, which corresponds to the equivalent noise bandwidth of 0.078 Hz (considering the filter

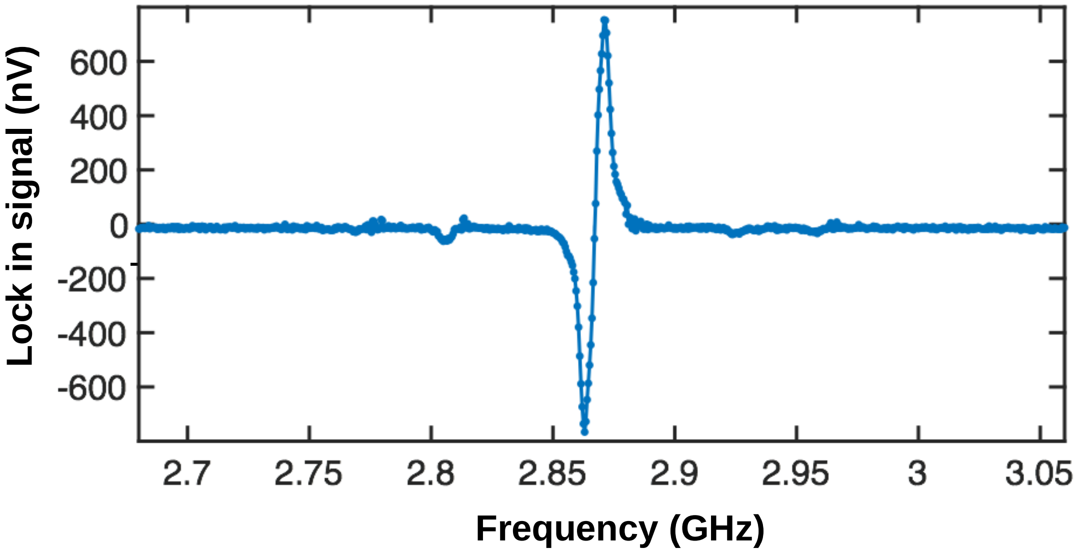

Figure 2-24: Frequency-modulated (FM) lock-in signal of NV spin-dependent fluorescence at zero external magnetic field.

roll-off of 24 dB/oct) of the lock-in amplifier. The use of the lock-in amplifier rejects the DC current offset of the photodiode, which is caused by the unmodulated green laser, and avoids the low-frequency flicker noise accordingly.

The measured ODMR of the ensemble of NV centers inside the diamond slab under zero external magnetic field applied is shown in Fig. 2-24. This spectrum corresponds to the derivative of the ODMR spectrum shown in Fig. 2-6. Next, a permanent magnet (6.27 mT) is aligned to split the spin transitions of the four NV orientations. Figure 2-25 plots the ODMR spectrum, which exhibits the expected eight spin transitions (Fig. 2-6). The use of the corresponding four NV ensembles enables vector magnetometry.

Monitoring the lock-in signal V at ν_- and ν_+ enables independent measurements of magnetic field and temperature. Specifically, the sum of the lock-in signal change ΔV at $\nu_\pm$ is proportional to ΔT, while the difference provides ΔB_z:

$$\Delta T = \frac{1}{2\beta_T}\left(\left.\frac{\Delta V}{dV/df}\right|_{\nu_+} + \left.\frac{\Delta V}{dV/df}\right|_{\nu_-}\right) \tag{2.9}$$

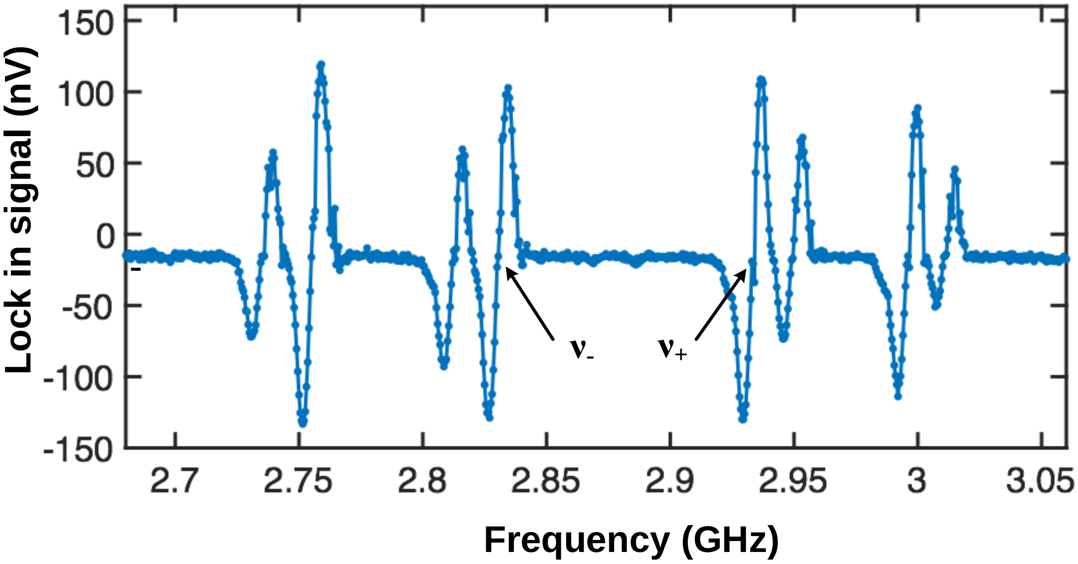

Figure 2-25: FM lock-in signal with a permanent magnet ($B = 6.27$ mT). The linewidth of the ODMR is 7 MHz. Slopes dV/df at $\nu_- = 2.8303$ GHz and $\nu_+ = 2.9330$ GHz are 42.969 nV/MHz and 42.450 nV/MHz, respectively.

and

$$\Delta B_z = \frac{1}{2\gamma_e}\left(\frac{\Delta V}{dV/df}\bigg|_{\nu_+} - \frac{\Delta V}{dV/df}\bigg|_{\nu_-}\right). \tag{2.10}$$

Figure 2-26 plots the detected ΔB_z induced by an electromagnet (blue) and measured center frequency shift (red). The square-wave magnetic field applied in Fig. 2-26 is generated by an electromagnet. Alternating electrical current is used to avoid magnetization. lock-in signals at both $\nu_\pm$ are observed while switching the polarity of external electromagnet with a period of 26 min. The center frequency shift represents the temperature shift in the experiment which is calibrated to determine the magnetic sensitivity. The magnetic field sensitivity is given by the following relation:

$$S = \frac{\sigma_{B_z}}{\sqrt{\text{ENBW}}}. \tag{2.11}$$

Here, σ_{B_z} is the noise in ΔB_z measurement, and ENBW is the equivalent noise bandwidth of the lock-in detector. In the measurements, $\text{ENBW} = 5/(64\tau)$ with a time constant τ of 1 second, accounting for the 24 dB/oct of the lock-in amplifier filter

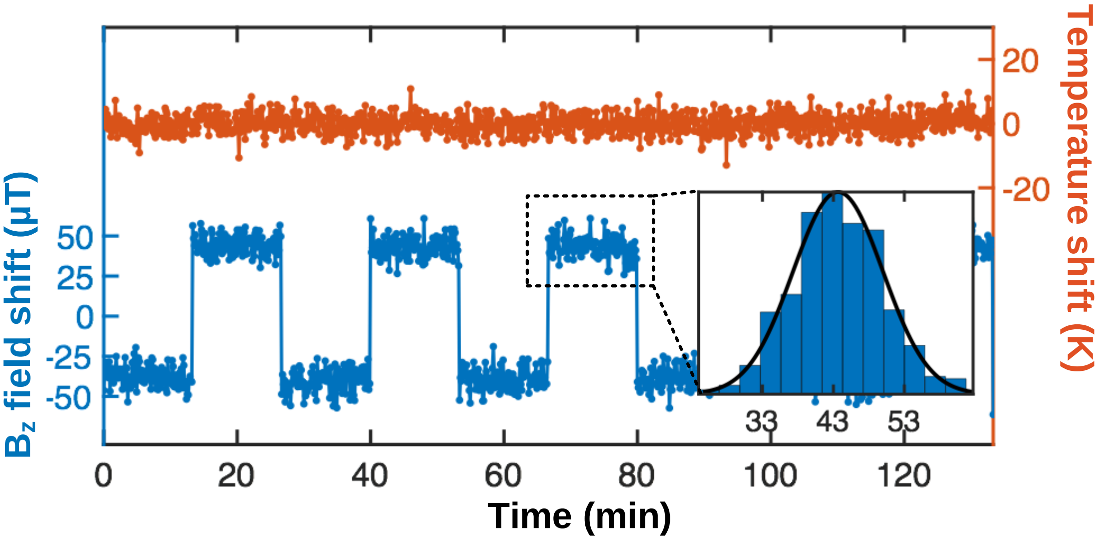

Figure 2-26: On-chip magnetometry (Blue) and temperature effect (Red) separation by detecting the effect of switching electromagnet on $\nu_{\pm}$ of the ODMR curve of Fig. 2-25.

roll-off. By measuring σ_{B_z} of 6.3 μT from the modulated spin-dependent fluorescence (Inset in Fig. 2-26), a DC magnetic field sensitivity of 32.1 μT/$\sqrt{\mathrm{Hz}}$ is determined. The sensitivity includes additional $\sqrt{2}$ factor of ν_+ and ν_- signal average. This DC magnetic field sensitivity is limited by the noise detected in the ENBW at $f_m = 1.5$ kHz.

In order to understand the contribution of each component on the overall noise performance of the system, the noise is measured using the lock-in amplifier. The measured overall noise in the experiment is 38 nV/$\sqrt{\mathrm{Hz}}$ at $f_m = 1.5$ kHz. This is primarily because of the green laser intensity noise, due to the limited performance of the optical filters. This laser intensity noise is orders of magnitude larger than other noise sources:

1. The thermal noise of the 50 Ω resistance (R), which is used to convert the photocurrent to voltage. This noise is ~ 0.9 nV/$\sqrt{\mathrm{Hz}}$ as calculated from Eq. 2.12:

$$\bar{V_n^2} = 4KTR\Delta f. \tag{2.12}$$

where K is the Boltzmann constant, T is the temperature, and Δ f is the bandwidth.

2. The NV red fluorescence shot noise is ~ 9 pV/$\sqrt{\text{Hz}}$ at $f_m = 1.5$ kHz as given in Eq. 2.13:

$$\bar{V_n^2} = R^2(2qi_D)\Delta f \approx R^2(2q\frac{V_{max}}{CR})\Delta f. \tag{2.13}$$

   where V_{max} is the maximum voltage in the ODMR curve in Fig. 2-25, which is 100 nV, C is the ODMR contrast ~ 0.02, and q is the electronic charge.

3. The amplitude noise converted from the microwave generator spectral purity is ~ 1 fV/$\sqrt{\text{Hz}}$ (see Eq. 2.14). The measured phase noise (ϕ_p) of the PLL is -90 dBc/Hz at an offset frequency of 1.5 kHz (FM modulation frequency f_m).

$$\bar{V_n^2} \approx (\phi_p f_m \beta)^2 \Delta f. \tag{2.14}$$

   Where β is the slope of the FM-ODMR curve.

Chapter 3

Scalable CMOS-Diamond Magnetometer

In our first CMOS-Diamond prototype presented in Chapter 2, we demonstrate the basic concept of chip-scale miniaturization of NV-center quantum sensors. As discussed in Section 2.7, the achieved sensitivity is still limited by two main factors:

1. The shot noise due to the green light, which is the dominant noise source in the experiment.

2. The sensing area used is only 50 μm × 50 μm. This limits the number of NV centers, N, and hence the SNR

In Fig. 3-1, we plot the magnetic sensitivity with the optical filtering and the sensing area (see Appendix A for more details). Ideally, this sensor would be limited to the red fluorescence shot noise and therefore, a higher green-to-red suppression ratio is required for the integrated photonic filter. As shown in Fig. 3-1, >50 dB green light filtering is required so that the majority of photodiode noise is no longer generated by the green background. In addition, increasing the sensing area enhances the sensitivity due to the increased number of NV emitters (N). Therefore a scalable design which can be extended to larger areas is required for ultimate sensitivity. Note that the SNR

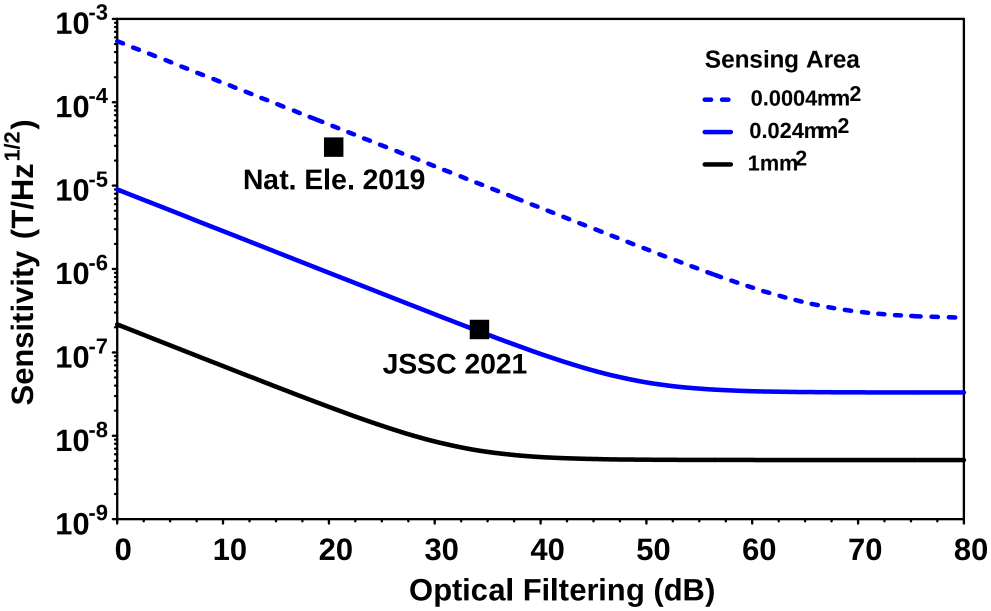

Figure 3-1: Estimation of sensitivity for hybrid CMOS-NV magnetometers with optical filtering and sensing area (NV density is 0.01 ppm).

has the following dependency with N:

$$SNR \text{ is} \begin{cases} \propto N & \text{when noise is green-light limited} \\ \propto \sqrt{N} & \text{when noise is red-light limited} \end{cases}. \tag{3.1}$$

3.1 A Scalable CMOS-NV Magnetometer for Enhanced Sensitivity

In this section, the design details of a new-generation CMOS-NV magnetometer [47, 48] are provided. The highly scalable architecture of our CMOS-NV magnetometer allows for the microwave driving of NVs over a large area. The photodiode noise is further reduced with the adoption of a new on-chip photonic filter. These structures are co-designed with the on-chip electronics.

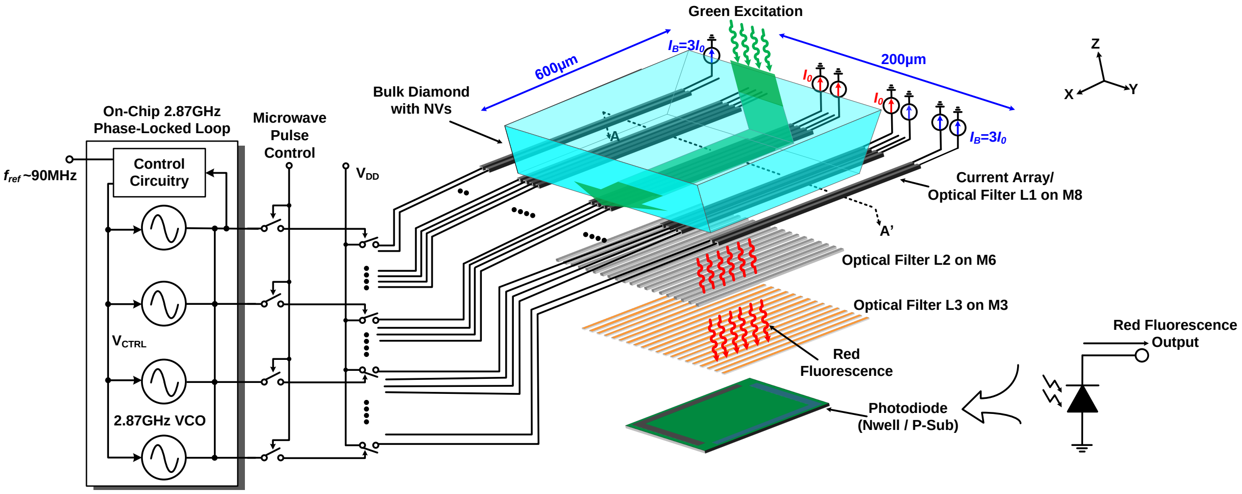

Figure 3-2: The overall schematic of the CMOS quantum magnetometer with high scalability.

3.1.1 Systematic Architecture of the Chip

The overall schematic of the CMOS-NV magnetometer is given in Fig. 3-2. Shown on the left of Fig. 3-2 is an on-chip phase-locked loop (PLL) which generates the 2.87-GHz microwave signal (see Section 3.1.5). To drive the NVs with the on-chip generated microwave field, an array of current-driven linear wires are implemented using the M8 of the chip, of which the driving currents are toggled by the PLL output. Such a design addresses a major challenge regarding the uniformity of the microwave magnetic field over a large area. In Section 3.1.2, detailed explanations of the microwave launcher are provided. In this work, a diamond area of ∼500 × 500 μm^2 is excited by the microwave. The sensing area with uniform microwave excitation is limited to 300 × 80 μm^2 as discussed in Section 3.1.4. Shown in Section 3.1.3 and 3.1.4, the current-driven wire array, along with additional two layers of metal gratings, also form a photonic filter in order to suppress the green light transmitted through the diamond placed on top of the chip. Finally, the spin-dependent red fluorescence of the NV centers is measured using an n-well/p-substrate photodiode.

3.1.2 Generation of High-Homogeneity Magnetic Field

Our NV-CMOS sensor interrogates an ensemble of NV centers to perform magnetometry. The microwave field strength determines both the ODMR resonance amplitude (contrast) and the resonance linewidth. Optimizing the sensitivity requires maximizing the contrast while minimizing the resonance linewidth [49]. For ensembles, the delivery of a homogeneous microwave magnetic field is critical in order to simultaneously perform this optimization across the entire area [50]. Such microwave homogeneity is also critical to pulse-based coherent quantum control protocols, such as Ramsey-type sequence, which can significantly increase the sensitivity to time-varying external magnetic fields [13]. Homogeneous microwaves *synchronously* rotate the spin states of a large number of NV centers on the Bloch sphere [51, 52]. Since the microwave-field strength determines the Rabi nutation frequency of each NV electron spin, spatial variation of the microwave field causes dephasing of the overall quantum ensemble.

Traditional microwave-launching structures include single straight wires [11, 49], metal loops [14, 19, 53] and split-ring resonators [51, 52]. They can only keep the field homogeneity in an area that is much smaller than the launcher size. That is undesired for compact chip implementation when excitation of a large-size diamond is pursued. Meanwhile, the above structures also have poor power-delivery efficiency, hence watt-level microwave input power is common [19, 51, 52]. We note the above solutions share one commonality in that they all rely on one piece of passive structure driven by a single electrical port. That, unfortunately, makes it extremely difficult, if not impossible, to synthesize a certain desired current distribution[1], because the only design variable is the structural geometry.

One distinct advantage of the implementation using integrated circuits is the highly flexible and tight integration between passive and active components. A large number of biased transistors, when forming current sources, can be used to mandate the complex current values at various particular locations on the passive structure (Fig. 3-3). Compared to the aforementioned passive-only structures, this new design methodology provides abundant additional degrees of freedom through the positions and currents of the embedded transistors. A finer control of near-field wave distribution is therefore

---

[1] For electrically-small structures (size$\ll\lambda_{2.87\mathrm{GHz}}$), the distributions of the current on the structure and the generated near-field magnetic wave follow a one-to-one mapping. Note that although displacement current also generates a magnetic field, our following discussions are constrained to structures mainly with conduction current.

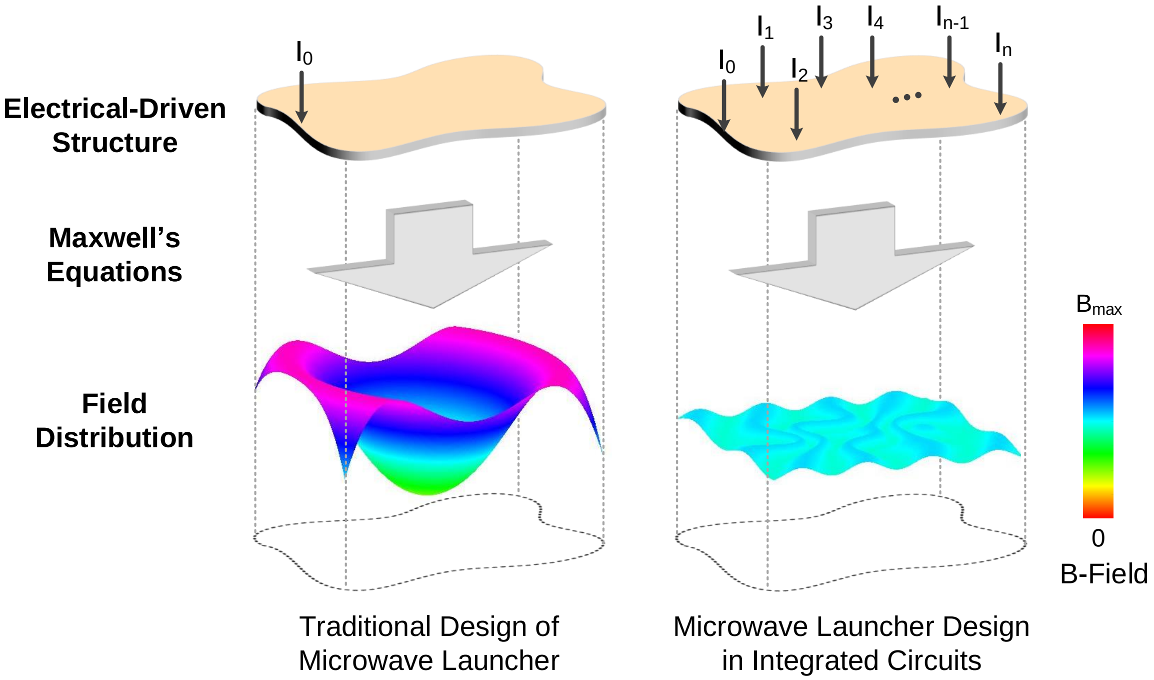

Figure 3-3: Comparison of design methodologies for the microwave launcher in a quantum sensor. A distributed co-design of passive and active components is equivalent to adding more boundary conditions to an electromagnetic-solving problem, hence providing better control of the near-field pattern.

much easier. Note that similar concepts were already proposed and applied to millimeter-wave and terahertz integrated circuit designs [54–56].

Following the above methodology, our microwave launcher design in Fig. 3-2 evolves from an ideal, infinite sheet of uniformly-distributed surface current density J_x (see Fig. 3-4a), which generates a homogeneous field B_y with a transverse (y-) direction and strength of $\mu_0 J_x/2$ (μ_0: permeability of vacuum). However, such current uniformity is hard to imitate in a single metal structure, due to the self-redistribution of current like skin effect. To prevent such redistribution, the current sheet is first transformed into an infinite array of wires, each driven by an identical current I_0 (Fig. 3-4b). With a tight wire center-to-center pitch d (or equivalent current density of I_0/d), a uniform transverse magnetic field can still be obtained, with a field strength of $\mu_0 I_0/2d$. The wire array also ensures high scalability in the longitudinal (x-) direction for large-area diamond.

In reality, only a finite wire array can be implemented. The introduced boundaries,

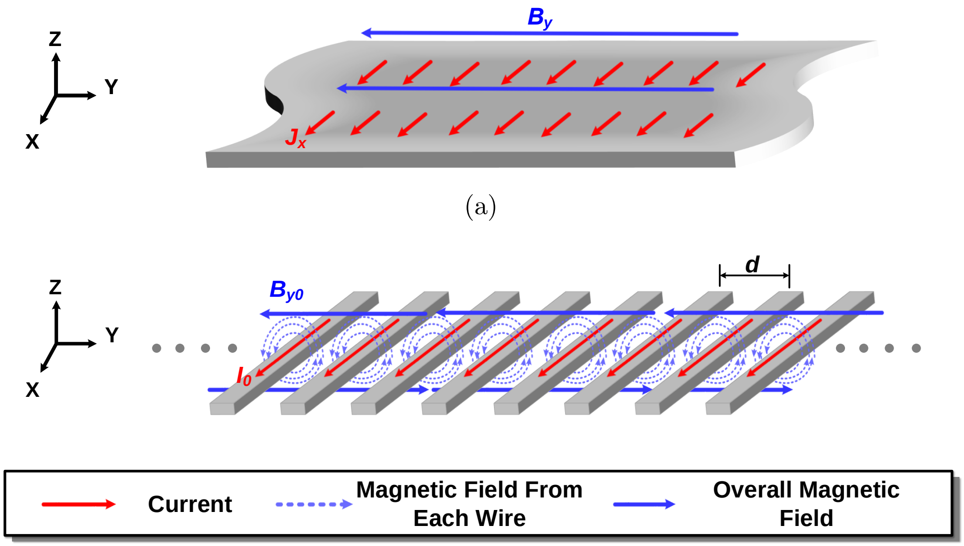

(a)

(b)

Figure 3-4: Approaches to generate homogeneous magnetic field: (a) an infinite sheet of uniformly-distributed current, (b) an infinite array of wires with uniform driving current.

however, break the above homogeneity. Figure 3-5 shows the simulated field distribution of a 48-wire array with d=4 μm. Although the transverse component of the field B_y maintains homogeneity, the vertical component B_z becomes non-zero and exhibits large gradient over y-axis. To understand that, we focus at a reference point (Point R) located above an array of N wires and closer to the left side (i.e. $y_R < 0$ in Fig. 3-6a). The wires are then divided to three groups: the n wires located between y_R and the left boundary $-L$ (Group A), another n wires symmetrically located at the right side of Point R (between y_R and $2y_R + L$, Group B), and the rest (Group C). Next, note that at Point R, the vertical magnetic fields generated by Group A and B cancel, and the B_z generated by Group C, by Ampere's Law, is:

$$B_{z,C}(y_R) = -\frac{1}{2\pi}\int_{2y_R+L}^{+L} \frac{\mu_0 J_x dy}{y - y_R} = \frac{\mu_0 J_x}{2\pi} \ln \frac{L + y_R}{L - y_R}, \tag{3.2}$$

where the discreteness of the array is approximated as a uniform current sheet with a current density of $J_x = I_0/d$. Note that Eq. 3.2 also applies for $y_R > 0$. Shown in Fig. 3-5, the result calculated from Eq. 3.2 well matches the simulation by HFSS [37]. Intuitively, $|B_z|$ increases towards the edges because the number of conductors in

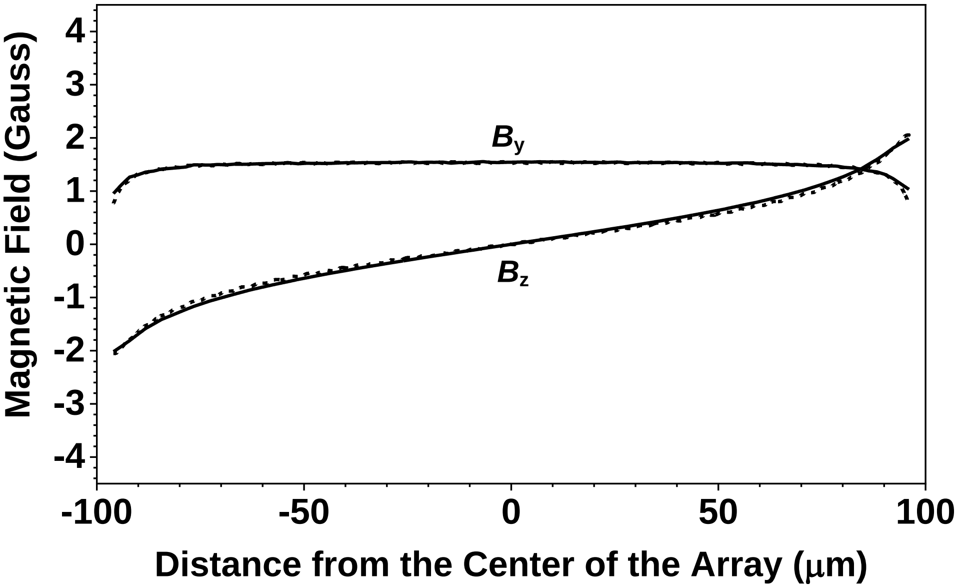

Figure 3-5: Simulated and calculated field distribution (f=2.87 GHz) of a wire array with uniform driving current (I_0=1 mA).

Group A and B decrease and the effect of the field due to the remaining Group C increases.

To create an opposite magnetic-field gradient for nulling the above B_z, a pair of additional m-wire arrays (Group D in Fig. 3-6b), which are driven by I_D per wire, are symmetrically placed at $y = -L - D$ to $-L$ and $y = L$ to $L + D$. Their combined impact on the vertical magnetic field at $y = y_R$ is derived as:

$$\begin{aligned} B_{z,D}(y_R) =& \int_{-L-D}^{-L} \frac{\mu_0 m I_D dy}{2\pi D(y_R - y)} - \int_{L}^{L+D} \frac{\mu_0 m I_D dy}{2\pi D(y - y_R)} \\ =& \frac{m\mu_0 I_D}{2\pi D} \ln \frac{(y_R + L + D)(L - y_R)}{(L + D - y_R)(y_R + L)}, \end{aligned} \tag{3.3}$$

of which some example plots (to be discussed more) is shown in Fig. 3-7, indicating the similarity of its curve shape to that from Group C. To further determine the value of I_D, we compare the derivatives of Eq. 3.2 and Eq. 3.3 around the center of the

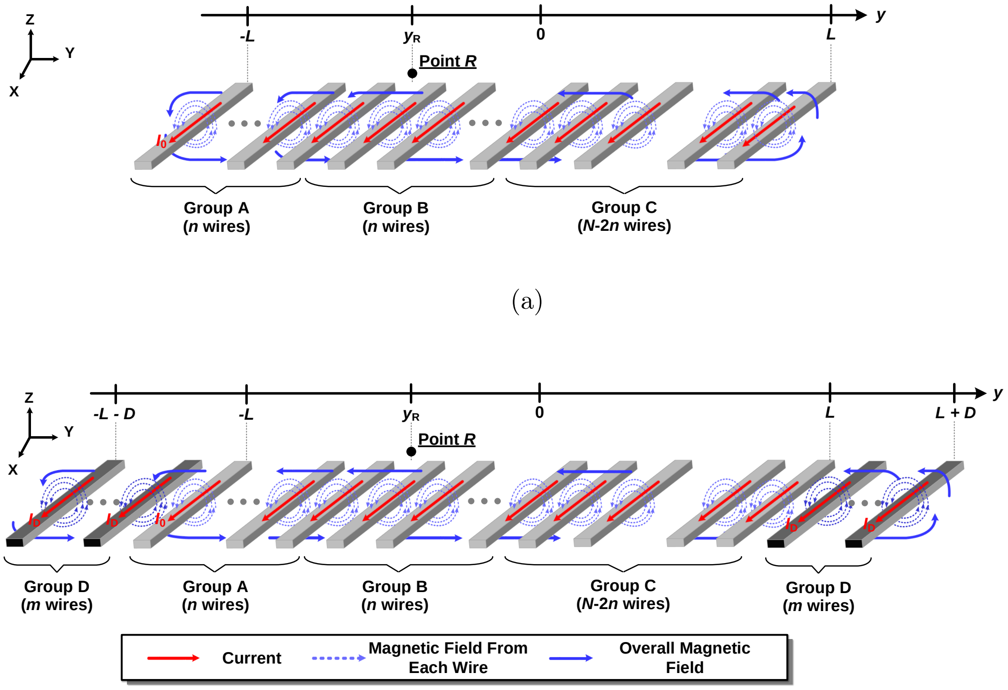

(a)

(b)

Figure 3-6: (a) A finite array of wires with uniform driving current. (b) An additional pair of boundary wire arrays (Group D) for nulling the vertical magnetic field between $-L$ and $+L$.

launcher:

$$\frac{dB_z}{dy}|_{y=0} = \begin{cases} \frac{\mu_0 J_x}{\pi L} & \text{for Group } C \\ -\frac{\mu_0 m I_D}{\pi L(L+D)} & \text{for Group } D \end{cases}. \tag{3.4}$$

Therefore, for zero B_z around the array center, the value of I_D should be:

$$I_{D,0} = \frac{L+D}{m} J_x = \frac{L+D}{md} I_0 = (1 + \frac{N}{2m}) I_0. \tag{3.5}$$

The last step of Eq. 3.5 assumes that the boundary arrays adopt the same wire pitch d as the N-wire uniform array in the center. For a 32-wire uniform array (N=32) with I_0=1 mA and d=4 µm, the vertical field $B_{z,D}$ generated by the boundary array pair with varying wire numbers m, as well as the residual of B_z after cancellation, are plotted in Fig. 3-7. We see that a larger m improves the area of uniformity at a modest expense of higher current consumption. Interestingly, if the I_D value is

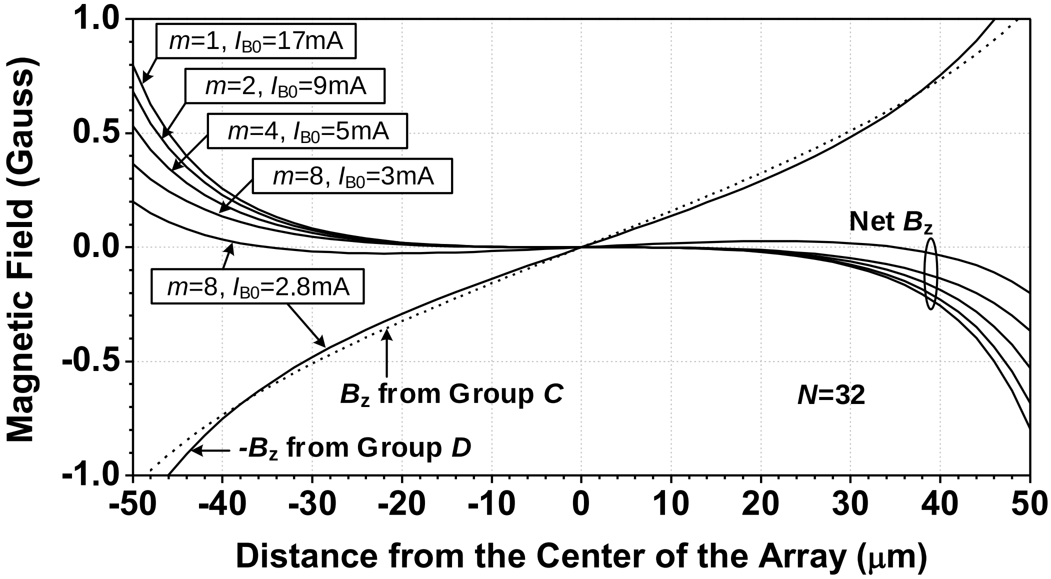

Figure 3-7: Calculated profiles of vertical field generated by Group C and D (and the residue after the cancellation) of the array shown in Fig. 3-6b. Note that the B_z of Group D is plotted with its polarity reversed, to facilitate a straightforward comparison with B_z from Group C.

slightly lower than the one calculated by Eq. 3.5 (e.g. for m=8, the calculated value for I_D is 3 mA), the B_z field around y=0 is not cancelled perfectly but the overall 95% uniformity area is extended to $y \approx \pm 40$ μm. Lastly, Fig. 3-8 shows the HFSS-simulated field distribution of the entire launcher (N=32, m=8, d=4 μm) including the current return path, which is implemented at the Metal 8 (M8) interconnect layer of our chip prototype. The calculated profile in Fig. 3-8 is achieved with $I_D=2.8I_0$. Note that the HFSS simulation is done with a slightly larger I_D ($I_D=3I_0$) to account for the uncalculated effect of current in the return path. Compared to Fig. 3-5, the overall homogeneity of the magnetic vector field is significantly improved.

3.1.3 Nano-Photonic Filter on CMOS

Based on the earlier discussion in this chapter, the rejection ratio of the photonic filter should be improved to enhance the magnetometry sensitivity. As discussed in Section 2.6, Increasing the slit thickness of the plasmonic filter by stacking more grating layers (in M7, M6...) is expected to further increase the suppression of the green light. However, that causes degradation of red-light transmission due to the scattering at

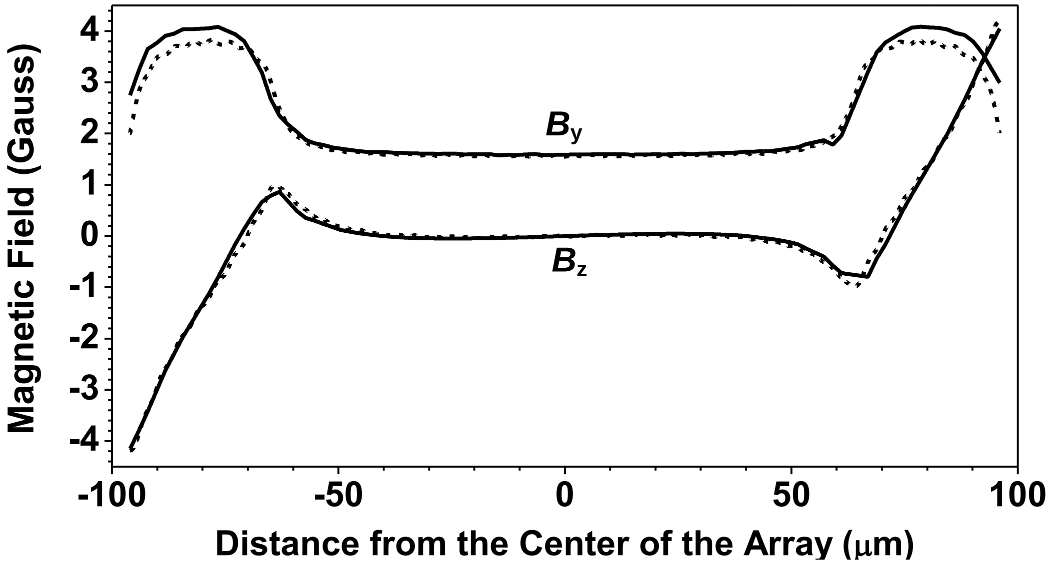

Figure 3-8: Simulated (solid line) and calculated (dashed line) field distribution of the entire launcher wire array. Here, f=2.87 GHz, N=32, m=8, L = 64 μm, D = 32 μm, I_0=1 mA, and $I_D \approx$3 mA.

the side walls formed by the sparse inter-layer via pillars. Moreover, as Section 3.1.4 describes, the grating structure in M8 is also used for the microwave wire array (Section 3.1.2). Connecting it to the lower metal layers would significantly decrease the density and the uniformity of the RF current inside the wires. In the scalable design described here, an alternative approach based on the wavelength-dependent diffraction pattern of the grating is adopted.

As the simulation in Fig. 3-9 shows, the diffraction of the light coming out of the grating in M8 causes repeated self-imaging patterns in the chip dielectric. That optical phenomenon is called Talbot effect [57] and the vertical (z-) period of the self-images (i.e. Talbot length) is:

$$z_T = \frac{\lambda}{1 - \sqrt{1 - \frac{\lambda^2}{t^2}}}, \tag{3.6}$$

where λ is the wavelength in the dielectric and t is the grating period (800 nm in our case). For the red (700 nm) and green (532 nm) light, z_T is ~2.5 μm and ~3.4 μm (see Fig. 3-9). That means we may strategically place additional metal structures at positions which are dark in red diffraction pattern (so that the light is not affected) but bright for green (so that the light is blocked). In the 65 nm CMOS process used for this work, the distance between M8 and M6 layers is close to the half Talbot length for red; therefore, a M6 grating with 400 nm strip width and pitch is placed. With the positions of the metal strips right under the slits of M8, the M6 grating has little interference with the red-light transmission, while blocking a significant portion of the green light (Fig. 3-10). It is noteworthy that the similar multi-grating concept was previously adopted for lensless 3D CMOS cameras [58], where the angle sensitivity of the structure is utilized. To the authors' best knowledge, this is the first time in CMOS that the idea of diffraction selectivity is applied into optical spectral filtering. Following the same principle, a third grating layer in M3, of which the distance to M8 is about one Talbot length at 700 nm, is added to further enhance the green-light rejection (Fig. 3-11). The same grating strip width and pitch of 400 nm are used. Figure 3-12 provides the normalized transmitted power (Poynting vector integrated over a x-y cross-sectional area) at varying chip depths. For green light, the plasmonic behavior attenuates the power by 9.7 dB, and the M6 and M3 gratings pose an additional 12.1 dB loss, leading to a total attenuation of 21.8 dB. Meanwhile, the total insertion loss for red light is only 2.1 dB. Note that the reflection loss at the top of M8, which is ∼3 dB due to the 50% metal fill factor, is not included in both cases. Lastly, the simulated transmission response (excluding the 50% surface reflection) of the filter from 500 nm to 750 nm is plotted in Fig. 3-13. The spectrum of the NV-center red

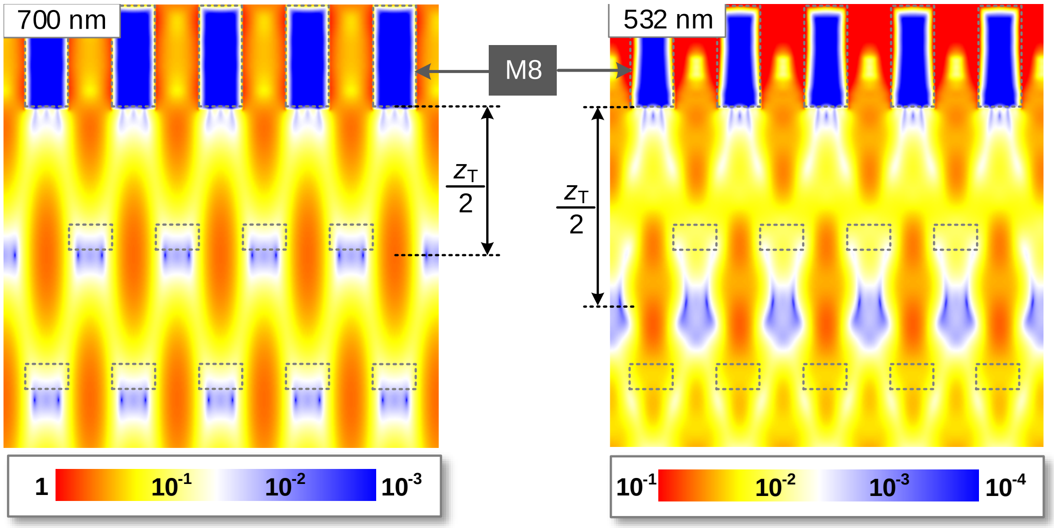

Figure 3-9: The simulated FDTD Poynting vector profile $|P|=|E \times H|$ for single-layer grating in M8. The scale bar for green (right column) is 10× lower than that for red (left column), in order to count for the ∼10-dB plasmonic loss in the M8 grating

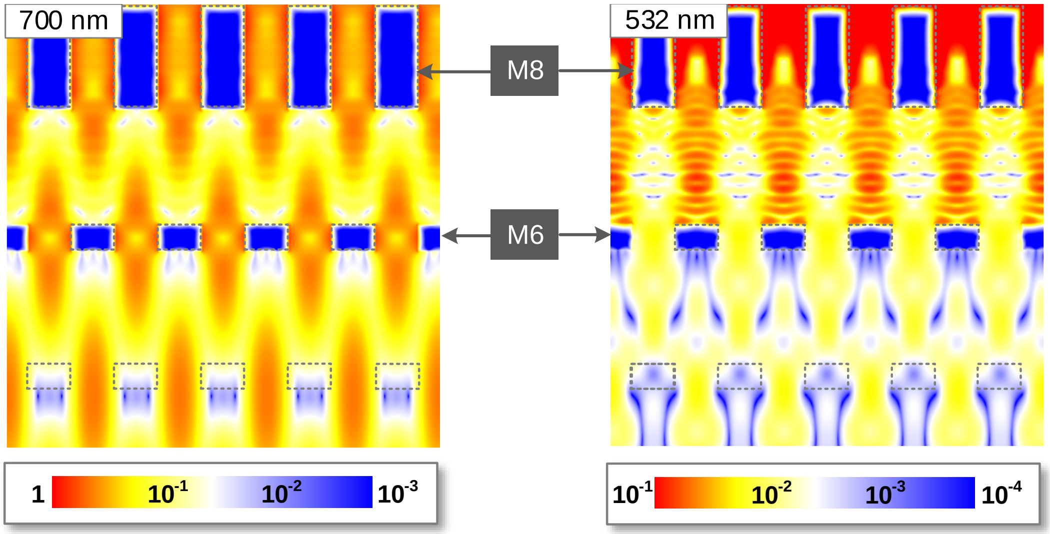

Figure 3-10: The simulated FDTD Poynting vector profile $|P|$=$|E \times H|$ for double gratings in M8 and M6. The scale bar for green (right column) is 10× lower than that for red (left column), to better show that the M6 gratings further suppress the transmission at 532 nm.

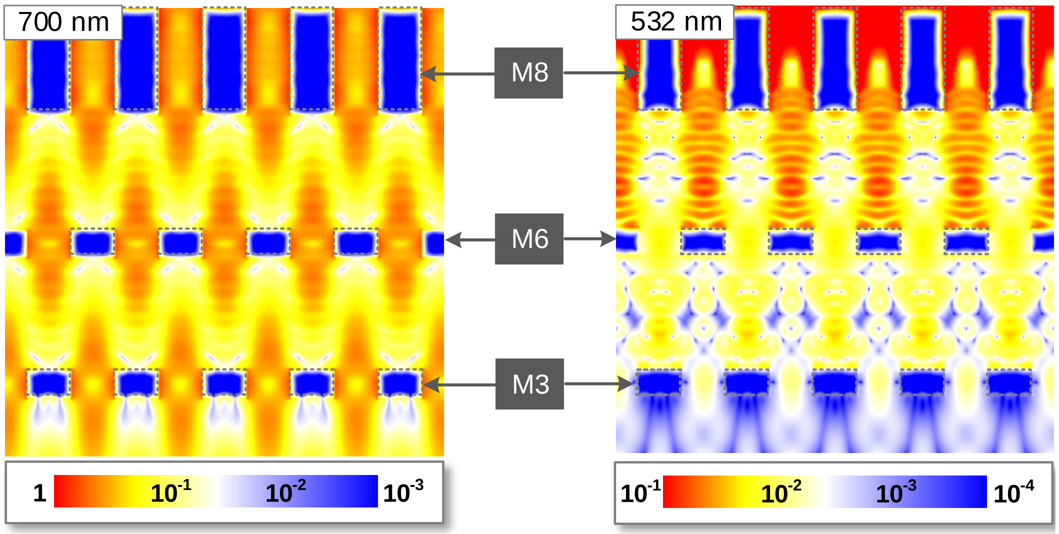

Figure 3-11: The simulated FDTD Poynting vector profile $|P|$=$|E \times H|$ for triple-layer gratings in M8, M6 and M3. The scale bar (add scale bar to the figures) for green (right column) is 10× lower than that for red (left column), to better show that the M6 and M3 gratings further suppress the transmission at 532 nm.

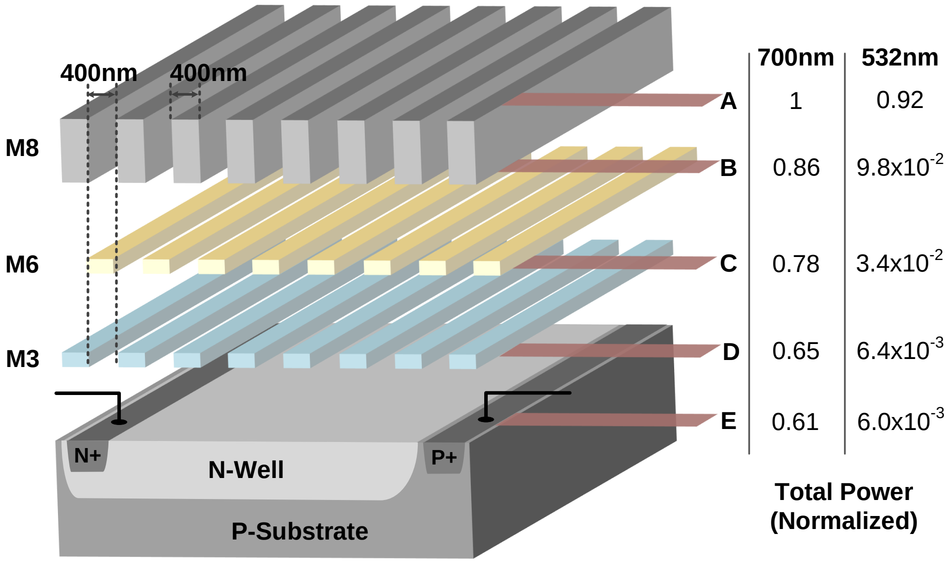

Figure 3-12: Simulated transmission values through the filter. The total power is derived by surface integrals of Poynting vectors at varying depths of the chip.

fluorescence is also shown. It can be seen that the majority of the fluorescence power between 650 to 725 nm is transmitted efficiently to the photodiode beneath the filter.

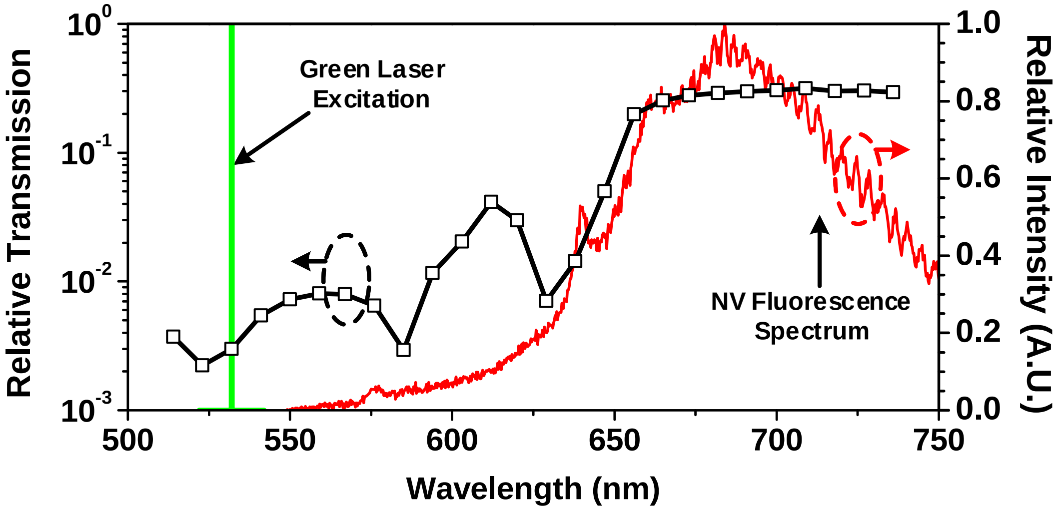

Figure 3-13: The transmission through the filter at different wavelength.

In general, the topmost layer of the filter should be as thick as possible and the separation between the metal lines should be as small as possible to increase the coupling to the plasmonic mode, hence larger green rejection. Note that there is normally a trade-off between the above two parameters due to the limited aspect ratio in CMOS technologies. The lower metal layers have to be placed in alignment with the maxima of the green and the minima of the red diffraction patterns. The vertical distance between metal layers in many CMOS processes is sufficient for the above requirement, although that in some more advanced technology nodes may not.

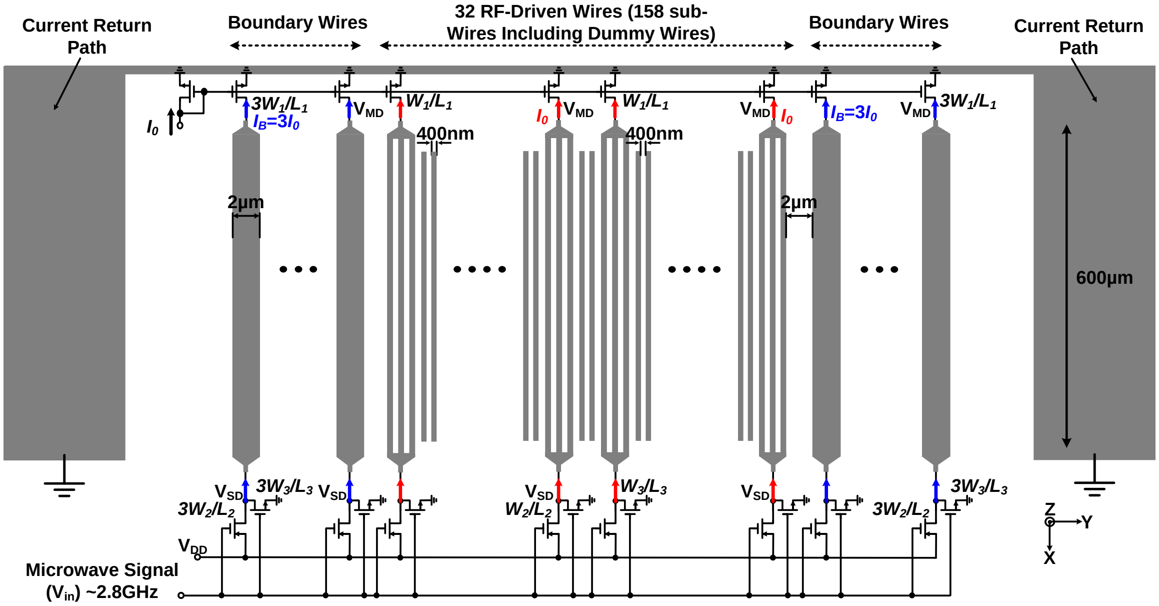

Figure 3-14: Schematic of the microwave launcher with the switches and the current sources.

3.1.4 Co-Design of the Circuits, Microwave Launcher and Photonic Filter

The full schematic of the microwave launcher with the switches and current sources banks is shown in Fig. 3-14. NMOS current mirrors are used to control the current in each individual wire of the array. PMOS switches are used to convert the rail-to-rail square-wave output voltage of the PLL into microwave square-wave currents in the array. It is worth mentioning that the higher harmonics of the square-wave microwave field is not sensed by the NV centers. Only the fundamental component ∼2.87 GHz dominates the operation of driving the electronic transitions. The current sources are designed to enable microwave square-wave current (I_0) control from 0.1 mA to 1 mA.

This corresponds to microwave field strength of 0.1 Gauss to 1 Gauss[2].

At low current values our simulation in Fig. 3-15 indicates that when the PMOS switches are off, the current of wire returns to zero at a slow speed. This is due to the parasitic capacitance of the wire array, the transistors in the current sources and switches, as well as the limited discharging current. The parasitic capacitance is estimated to be ∼5 fF from Fig. 3-15, assuming a linear discharging current of 0.1 mA flowing in each wire. To increase the pull down speed, a row of NMOS switches are also used (see Fig. 3-14) to provide a fast discharging (see the comparison in Fig. 3-15). The transistors dimensions (W_1/L_1, W_2/L_2, and W_3/L_3) are scaled up by a factor of 3 at the boundaries. As described in Section 3.1.2, the microwave launcher is implemented on M8 with wire width and spacing of 2 μm. Therefore, all the transistor layouts are designed in a multiplier fashion so that they can fit in the tight wire pitch. In addition, the layout of the transistors is fully symmetric to minimize the mismatch. A pair of wide return ground paths are used to close the current loop.

Part of the photonic filter is also implemented on M8 with unit width and spacing of 400 nm (shown in Fig. 3-12). The smallest dimension limited by the design rule of the technology is selected to enhance the coupling to the surface plasmon polariton mode. To cater the needs of both components, shown in Fig. 3-14, each of the microwave launcher wires other than the boundary wires is divided into three sub-wires with their two ends electrically connected. The width and the spacing of these sub-wires are 400 nm. In addition, each of the 2 μm spacing in the microwave launcher is filled with another two electrically floating dummy wires with 400-nm width and spacing (Fig. 3-14). These dummy wires do not affect the microwave generation/delivery operation, but along with the other sub-wires, they form the desired photonic filter geometry. The metal gratings implemented at M6 and M3 are also electrically floating and have very small thickness (∼0.2 μm). Therefore, the eddy currents generated due to the microwave field in the horizontal direction is negligible and does not affect the

---

[2] Note that the I_0 used in Section 3.1.2 refers to the current of a sinusoidal wave at $f_0 \approx 2.87$ GHz. To be consistent with the values given here, the simulated/calculated magnetic-field strength in Fig. 3-8 should be multiplied by a factor of $2/\pi$ to count for the amplitude difference between a square wave and its fundamental sinusoidal component.

uniformity of the microwave field. In the current design, the local metal density rules around the sensing area are waived. The filter area is 350×130 µm^2. In this prototype, we implement blocking walls around the photodiode area and a conservative size was adopted for the sensing area, to minimize the leakage of light into the photodiode. The size of the photodiode placed under the filter is 300×80 µm^2. In future designs, the photodiode area may increase for better SNR.

This array generates >95% field homogeneity over $\sim$ 50% of its area compared to 25% in [38]. Uniform array spacing is adopted in this design, however, in Chapter 5, we show that a certain gap between group D and group A/C can achieve homogeneity across a larger area. The design is only enabled by CMOS technologies, where we can integrate a very tight wire array with efficient switching and current control.

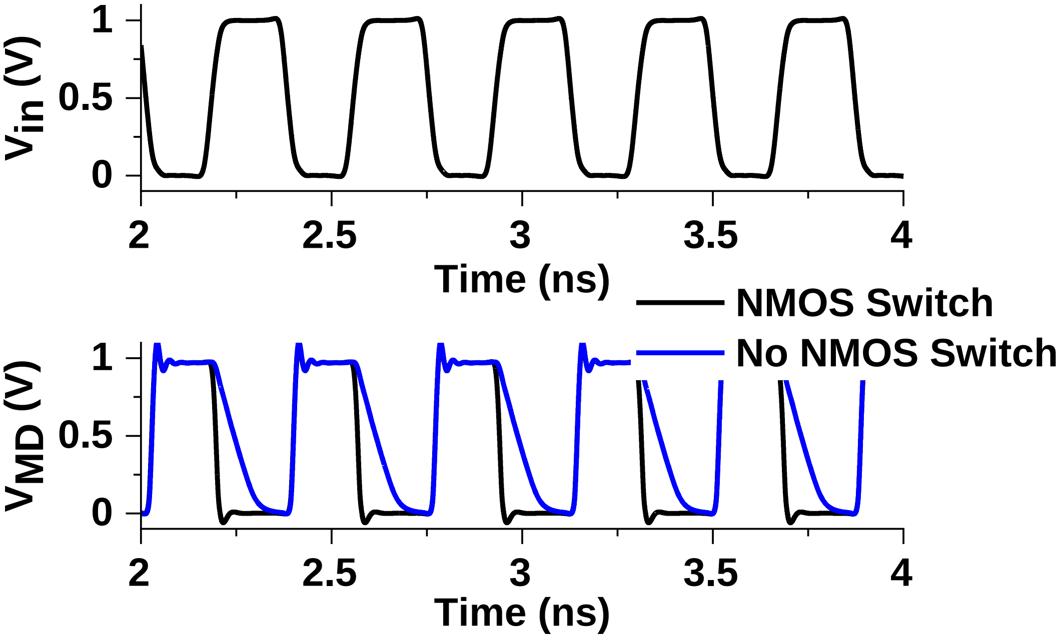

Figure 3-15: Comparison the switching performance with and without extra NMOS switch. The first plot shows the input microwave signal (V_{in}) and the second one shows the voltage at the drain of the NMOS current source (V_{MD}).

3.1.5 On-Chip Synthesis of the Microwave Frequency

A PLL loop is used to stabilize the output of the voltage-controlled oscillator (VCO) that drives the NV centers. The full schematic of the PLL is shown in Fig. 3-16. To ensure a uniform phase of the magnetic field across the wire array, the VCO is based on a tightly-coupled ring-oscillator array. Four sub-oscillators are placed with a spacing of ∼50 µm (see Fig. 3-2). The two oscillators in the middle drive 32 wires, while the other two oscillators on the array boundaries drive 8 wires each. Compared to a centralized signal-generation scheme, the coupled-oscillator eliminates the phase variation caused by different lengths of the microwave-distributing traces. In addition, careful placement and routing are done to ensure uniform phases at the wire array. Our simulations show that the uniformity of the horizontal component of the microwave field (B_y) is >95 % for 5° random phase mismatch, which is the expected maximum phase mismatch at the wire array inputs. Here, ring oscillators, instead of LC oscillators, are chosen, in order to eliminate the need for extra inductors, as well as any magnetic coupling and degradation of field homogeneity in the diamond-sensing area. A ring oscillator also offers wider tuning range and layout compactness. Its inferior phase noise is improved by 6 dB due to the oscillator coupling, and in fact our analysis indicates that our sensor sensitivity is currently limited by the green and red light noise, as explained in Section 3.2.2. The VCO frequency is tuned using varactors (C_v=9 to 42 fF) with a coefficient of 1.2 GHz/V. The charge pump current of the PLL is 5 mA and the loop filter parameters are C_1=1 nF, R_6=220 Ω, and C_2=20 pF.

3.2 Chip Prototype and Experimental Results

The chip prototype is fabricated using a TSMC 65-nm CMOS technology. The chip micrograph is shown in Fig. 3-17a. The chip has an area of 1×1.5 mm^2 and consumes 40 mW of power. In the experiment the amplitude of the square wave current in the microwave launcher (I_0 in Fig. 3-14) is set to 0.5 mA, which corresponds to 0.5 Gauss of microwave field strength. This field efficiently couples to a diamond slab with NV centers placed and attached directly onto the top of the CMOS chip as shown in

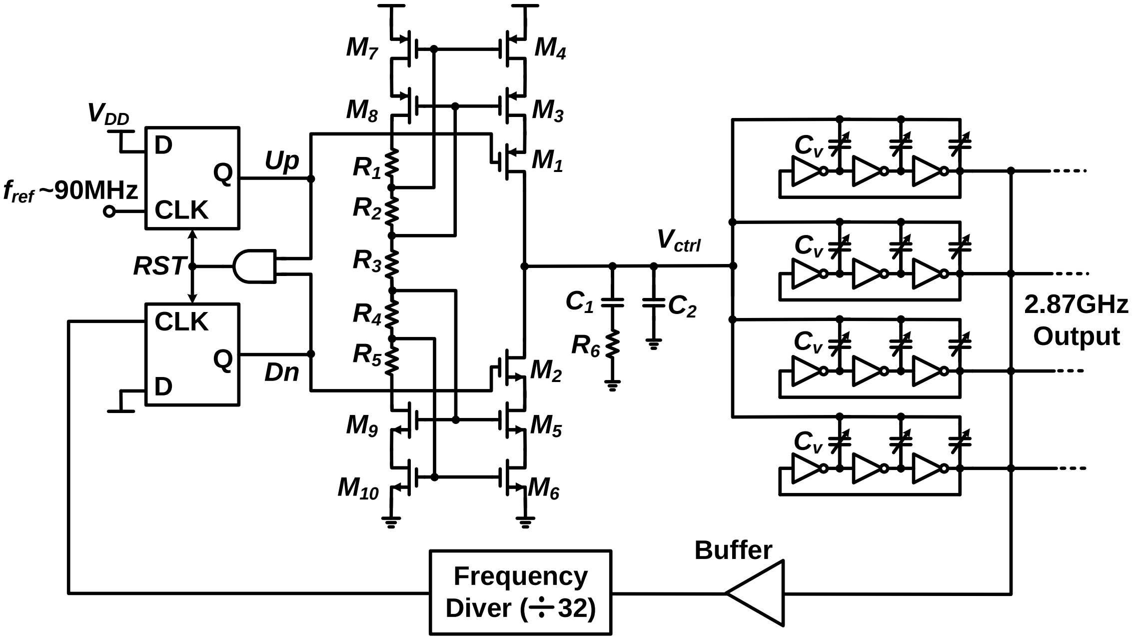

Figure 3-16: Schematic of the 2.87-GHz PLL.

Fig. 3-2 and 3-17b. This diamond is a single crystalline CVD-grown diamond from Element 6. It is electronically irradiated with a dosage of 10^{18} e^-/cm^2 at 1 MeV, and then annealed for 2 hours at 850°C. This results in 0.01 ppm of NV density in the diamond. Immersion oil is used to adhere the diamond slab to the chip. By bridging the difference of the refractive index, the oil also minimizes the fluorescence loss. The measured filter rejection for green light (532 nm) is ∼25 dB, which well matches the simulation results in Section 3.1.3. We measure the green light rejection of the filter using two test photodiodes as shown in Fig 3-17a. One of them is covered by the photonic filter. Then we compare the output current in both cases at the same laser intensity level. A 45° cut is introduced in the diamond's corner to direct the vertical incident green laser horizontally to further enhance the overall green rejection ratio to ∼33 dB. The extra green light rejection is measured by comparing the output current of the photodiode due to the green laser with and without diamond slab. The measured responsivity of the on-chip photodiode is 0.19 A/W at the green laser wavelength (532 nm). This corresponds to a quantum efficiency of 45%.

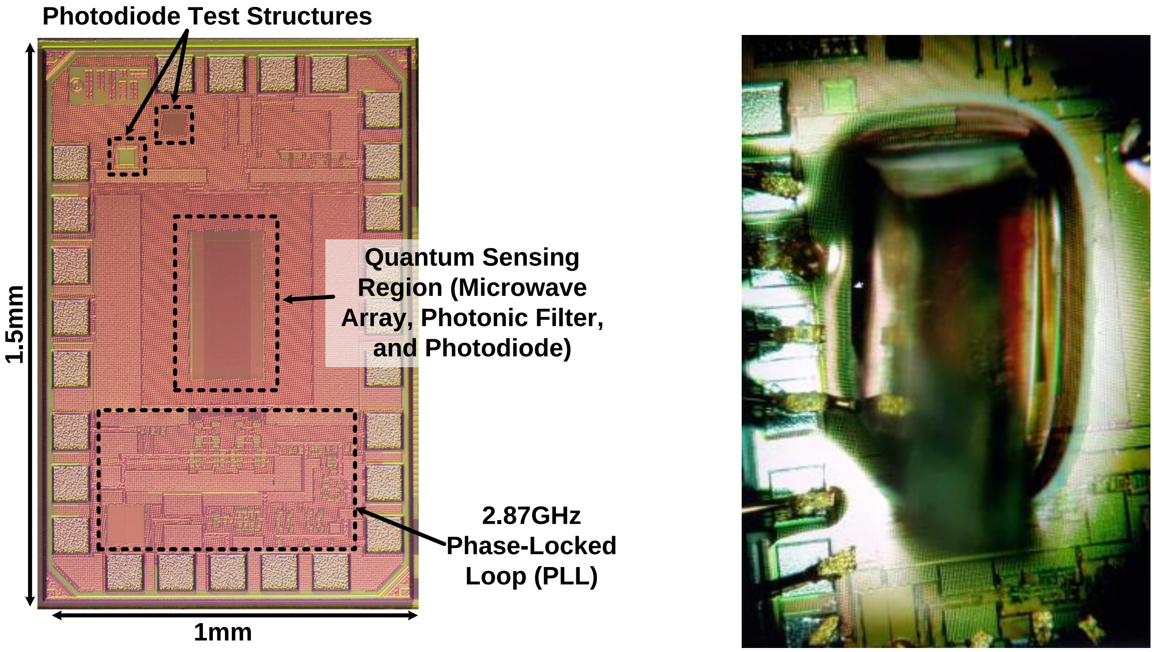

(a) (b)

Figure 3-17: (a) The micrograph of the CMOS quantum magnetometry chip. (b) The chip with a diamond placed on the top.

3.2.1 Optical Detected Magnetic Resonance Measurements

The measurement setup to generate the ODMR spectral line is shown in Fig. 3-18a. A 532-nm gaussian laser beam is used to excite the NV centers in the diamond. The laser beam diameter and power are 100 μm and 200 mW, respectively. This corresponds to 40 μA of current due to the green laser pump. The beam is focused on the diamond slanted edge, which then directs it horizontally. The red fluorescence detected by the on-chip photodiode is recorded while sweeping the reference signal (∼90 MHz) of the on-chip PLL. Due to the limited green-red suppression ratio of the on-chip filter, the red fluorescence signal is still superposed on a large green-light background at the output of the photodiode. Meanwhile, we notice the green-light excitation exhibits large power fluctuation, so to remove the fluctuating background signal, a frequency-modulation (FM) scheme is used, where the chip-generated microwave probing frequency $f_p(t)$ is periodically varied with a deviation of 6 MHz and repetition frequency f_m of 3 kHz. That is done by modulating the ∼90-MHz reference signal of the on-chip PLL. As shown in Fig. 3-18b, the corresponding photodiode output changes at f_m (with harmonics at $2f_m$, $3f_m$, etc.), which is then readily measured by a lock-in amplifier (SR865) with the reference at f_m. The lock-in amplifier also provides narrow-band filtering around f_m. Note that the FM technique is common in

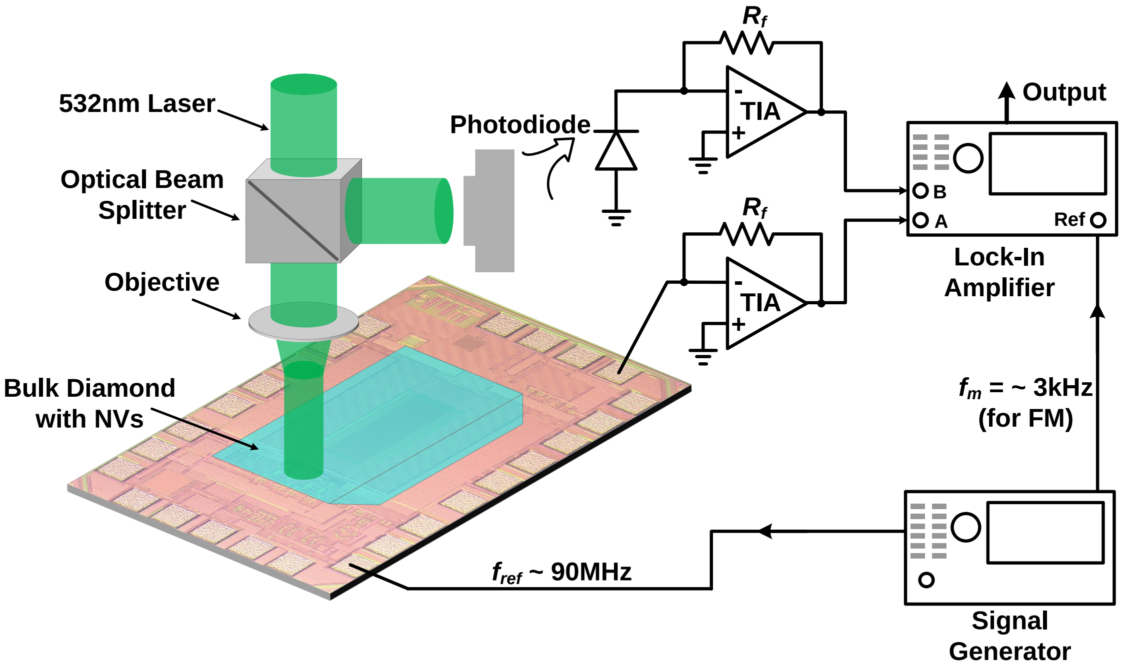

(a)

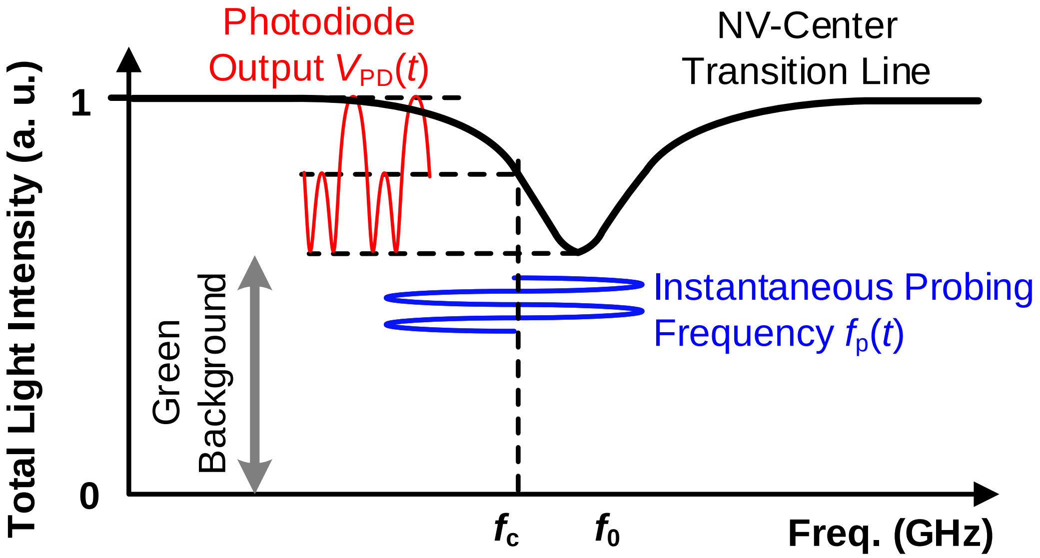

(b)

Figure 3-18: (a) The test setup for the hybrid NV-CMOS magnetometer. (b) The frequency-modulation scheme used in the setup.

spectroscopy [59] and atomic/molecular clocks [4]. Lastly, to further de-embed the excitation noise within the lock-in amplifier bandwidth, a differential detection scheme is adopted, where a split beam of the same laser is measured by an off-chip photodiode; such a duplicated noise signal is then taken by the lock-in amplifier and is subtracted from the chip output. Two identical off-chip resistive transimpedance amplifiers (TIA) with transimpedance gain of 10 kΩ are used to convert the photodiode currents into voltage. This gain is chosen to prevent the saturation of the amplifier due to the green current background (40 μA)

First, without an externally applied magnetic field, an ODMR plot is obtained as shown in Fig. 3-19a. A strong spin resonance, which results from all four NV centers in the diamond lattice, is detected at 2.87 GHz. The FM technique introduced previously can be interpreted as taking the first-order derivative of the regular Gaussian-shape transition line; as a result, the measured curve has the zigzag shape shown in Fig. 3-19a. The zero-crossing point corresponds to the actual transition frequency. Next, a 5.4-mT DC magnetic field is applied to the sensor from a nearby permanent magnet. This results in the Zeeman splitting for the spin states of the NV centers. As shown in the measured ODMR plot in Fig. 3-19b, four pairs of resonances are observed. They correspond to the four NV-center orientations of the single crystalline diamond. The difference of the transition frequencies (i.e. zero-crossing points) in each resonance pair is proportional to the external static magnetic field along the associated NV-center orientation. The proportionality constant, as described in Section 2.2, is γ_e=28 GHz/T. Accordingly, the magnetic fields along the four NV-center orientations are 0.77 mT, 2.27 mT, 3.25 mT, and 4.77 mT, respectively. Lastly, as the comparison between Fig. 3-19a and 3-19b shows, the chip output signal with external magnetic field is reduced due to the breaking of the degeneracy of the resonances from 2.87 GHz. Figure 3-19b clearly indicates that, by mapping the projections of the external magnetic field along the four NV-center orientations and certain frame of reference, one can construct the full vector magnetic field.

One practical way to use the sensor for vector-field sensing, is to first “bias" the sensor with a static magnetic field (e.g. a permanent magnet), which allows for the four

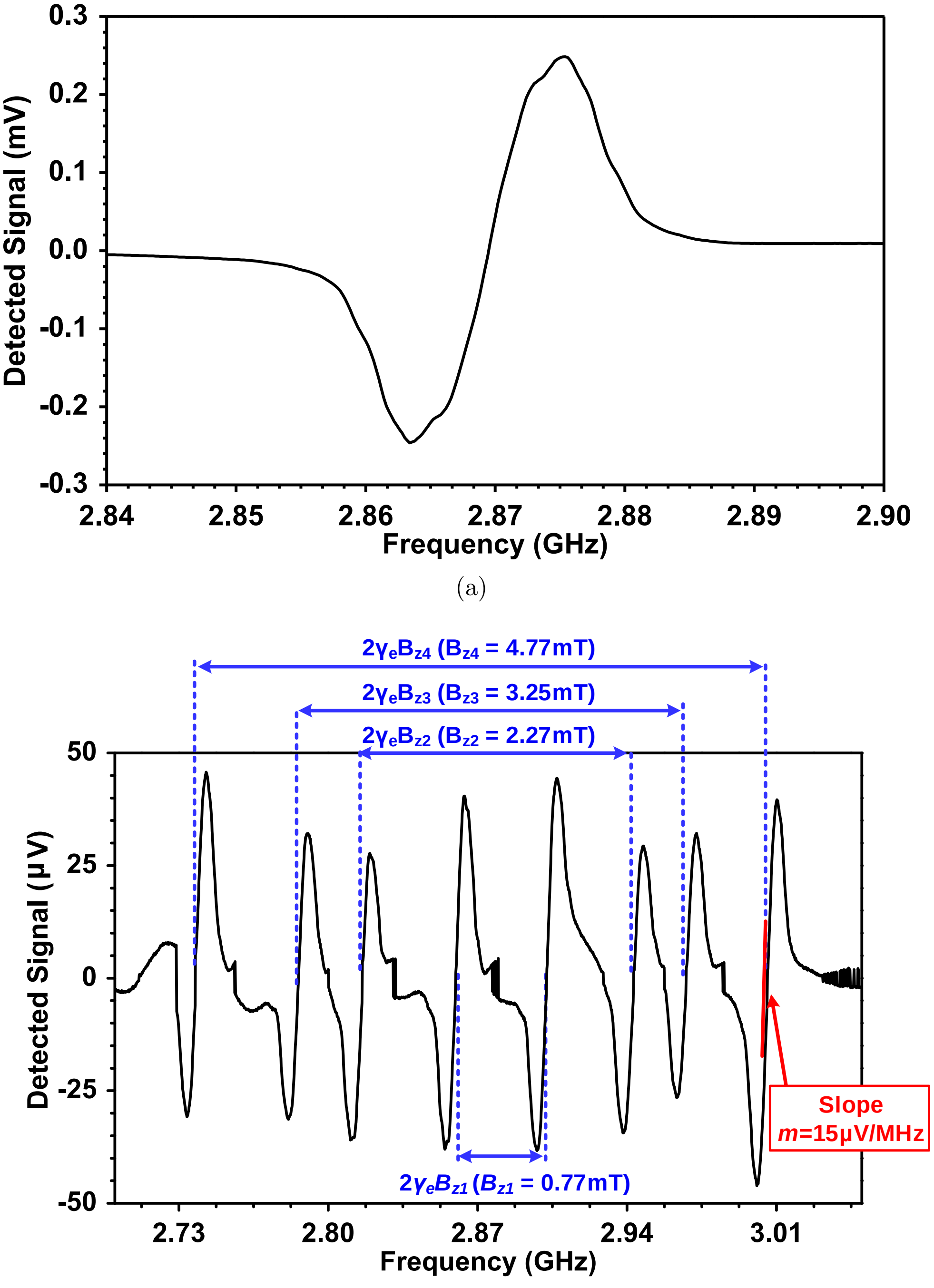

(a)

(b)

Figure 3-19: Measured optically-detected magnetic resonance (ODMR) plot from the CMOS chip, when (a) no external magnetic field is applied, and (b) a 5.4-mT external magnetic field is applied from a certain angle.

resonances to be completely split (such as shown in Fig. 3-19b). Then, we record the additional change of the sensor output voltage $\Delta v_{out,i}$ (i=±1, ±2, ±3, ±4) around each zero-crossing point of the FM-based ODMR curve. Note that $\Delta v_{out,i}$ is caused by the shift of each resonance frequency Δf_i due to the projection of the added field on the associated NV-center axis ΔB_{zi} (to be measured) on top of the bias static field, its expression is (for positive i):

$$\Delta v_{out,i} = m\Delta f_i = m\gamma_e \Delta B_{zi}, \tag{3.7}$$

where m is the slope of the ODMR curve at each transition zero-crossing point (~15 μV/MHz in our case, see Fig. 3-19b). The value of ΔB_{zi} can be derived from $\Delta B_{zi} = \Delta v_{out,i}/(m\gamma_e)$. Note that the transition frequencies of both $|m_s = \pm 1\rangle$ sublevels are also temperature dependent (with a coefficient of -74 kHz/K [60]). To cancel such temperature-induced drifts, it is better to measure the differential change of each pair of $|m_s = \pm 1\rangle$ transitions, and use the following equation for ΔB_{zi} [39]:

$$\Delta B_{zi} = \frac{\Delta v_{out,i} - \Delta v_{out,-i}}{2m\gamma_e} \quad (i = 1, 2, 3, 4). \tag{3.8}$$

3.2.2 Magnetic Sensitivity Estimation

In order to calculate the magnetic sensitivity of the sensor, the noise floor, σ (unit: V/Hz$^{1/2}$), is measured. The sensor noise is measured by monitoring the read-out of noise in the lock-in amplifier while sweeping the modulation frequency f_m. The results are shown in Fig. 3-20, where the sensor noise floor is ~0.1 μV/Hz$^{1/2}$. The noise below 3 kHz is mainly flicker noise. However there are some points where the noise peaks abruptly. Those are caused by the interference from the unshielded testing environment. This does not affect the noise performance of the sensor, since we are only interested in the noise around f_m (3 kHz) due to the lock-in detection used in the experiment. The magnetometer sensitivity S (unit: T/Hz$^{1/2}$), which is the minimum detectable magnetic field with 1-s integration time, is calculated using the following

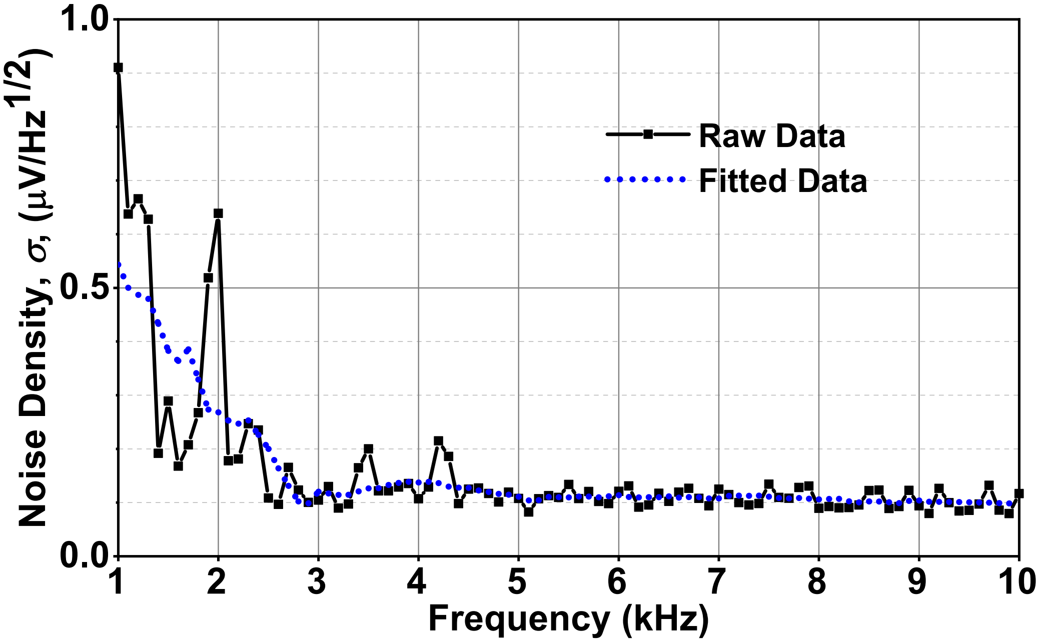

Figure 3-20: The measured output noise floor of the sensor.

equation:

$$S = \frac{\sigma}{\gamma_e m}. \tag{3.9}$$

The measured magnetometry sensitivity of this sensor at f_m=3 kHz is 245 nT/Hz$^{1/2}$. The sensor performance is limited by the green light fluctuations and the thermal noise of the TIA. The theoretical magnetic sensitivity (S_{th}) of the sensor can be estimated using the following:

$$\begin{aligned} S_{th} =& \frac{\sigma_{th}}{\gamma_e m} = \frac{\sqrt{2(\bar{V}^2_{n_g}) + \bar{V}^2_{n_r} + 2(\bar{V}^2_{nt})}}{\gamma_e m} \\ =& \frac{\sqrt{2(2qi_g R_f^2) + 2qi_r R_f^2 + 2(4KTR_f)}}{\gamma_e m}, \end{aligned} \tag{3.10}$$

where σ_{th} is the theoretical noise limit due to the green light shot noise ($\bar{V}^2_{n_g}$), the red fluorescence shot noise ($\bar{V}^2_{n_r}$) and the TIA thermal noise ($\bar{V}^2_{nt}$) referred at the output of the TIA. For the first term of σ_{th}, q is the electronic charge, i_g is the current measured at the photodiode due to the green light (∼40 μA), and R_f is the feedback resistor of the TIA (10 kΩ). i_r in the second term of σ_{th} represents the the detected red fluorescence current by the photodiode. This current i_r equals $\frac{V_{max}}{CR_f}$, where V_{max} is the maximum voltage (∼45 μV) of the ODMR curve in Fig. 3-19b, and C is the ODMR contrast of ~ 0.01. Therefore, i_r equals 450 nA. In the third term of σ_{th}, we assume that the TIA output referred noise is mainly limited by the feedback resistor R_f, K is the Boltzmann's constant, and T is the temperature. The factor of 2 used in the first and third terms of σ_{th} is due to the addition of the noise power from the two detection branches. Based on Eq. 3.10, the calculated theoretical sensitivity value is ∼150 nT/Hz$^{1/2}$, which agrees to a good extent with the measured value, and the difference is due to the residual un-canceled green light fluctuation. Even though this differential measurements technique increase the total shot noise limit by a factor of $\sqrt{2}$, it helps in canceling almost all the external laser fluctuation, which is almost one order of magnitude larger than the shot noise limit in our case. Moreover, $\bar{V_{n_g}}$, $\bar{V_{n_r}}$ and $\bar{V_{n_t}}$ in Eq. 3.10, equal 36 nV/Hz$^{1/2}$, 3.8 nV/Hz$^{1/2}$ and 12 nV/Hz$^{1/2}$, respectively. This confirms that the contribution of the green light shot noise is the dominant source of noise in our system.

The magnetic sensitivity S_m due to the amplitude noise converted from the microwave generator spectral purity also does not limit the sensitivity and its effect is negligible. The microwave signal that drives the NV centers can be represented as:

$$V_{RF} = V_0 \cos\left(\omega_0 t + \phi_n(t)\right), \tag{3.11}$$

where V_0, and ω_0 are the microwave signal amplitude and frequency, respectively. $\phi_n(t)$ is the phase noise of the microwave frequency. The instantaneous frequency can be represented as:

$$\omega(t) = \omega_0 + \frac{d\phi_n(t)}{dt}, \tag{3.12}$$

The frequency fluctuations around the operating frequency (ω_0) is related to the phase noise by:

$$\delta\omega = \frac{d\phi_n(t)}{dt}, \tag{3.13}$$

In our case, a lock-in amplifier is used to observe the noise around the modulation frequency (ω_m). Therefore, $\phi_n(t){=}\phi_n \cos 2\pi f_m t$ can be assumed to have a sinusoidal form, where ϕ_n is the phase noise of the microwave source at the modulation frequency (f_m) in dBc/Hz. This means the peak frequency fluctuation is $\approx 2\pi f_m \phi_n$. Therefore the voltage spectral density due to the PM to AM noise conversion is represented as:

$$\sqrt{\frac{\bar{V}_n^2}{\delta f}} \approx 2\pi f_m \phi_n m, \tag{3.14}$$

where m is the slope of the FM curve in V/Hz.

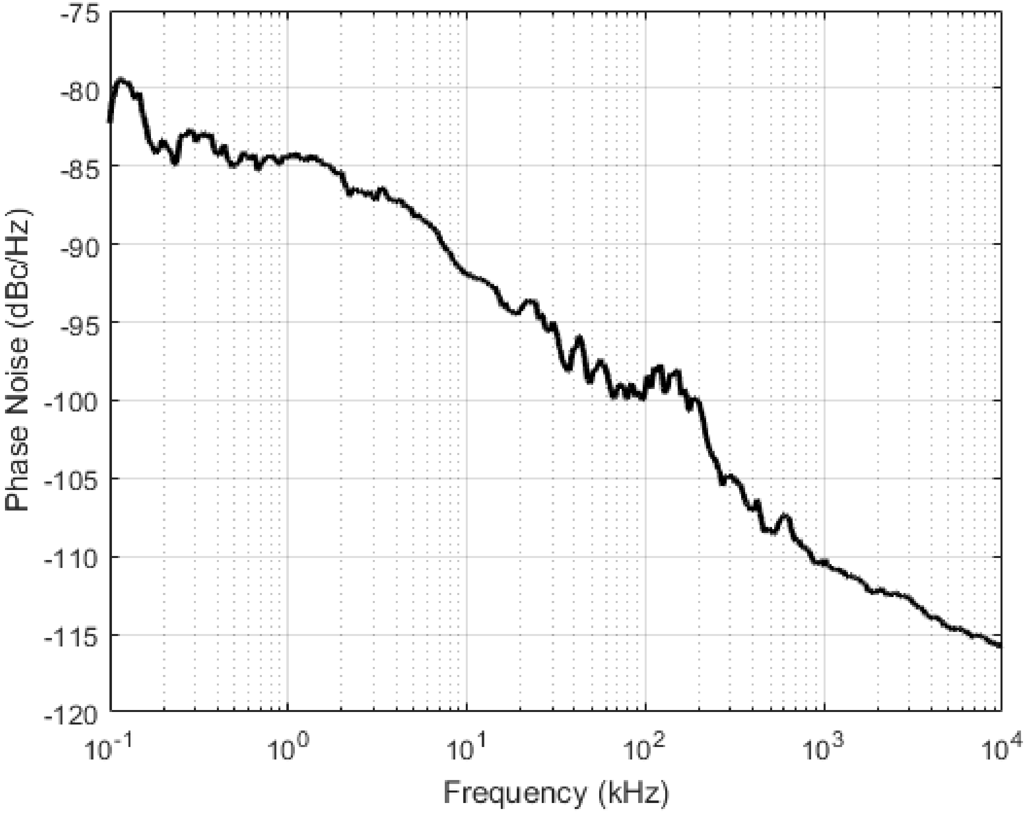

Figure 3-21: The measured phase noise of the PLL.

Therefore S_m is given by the following equation:

$$S_m = \frac{\sigma_m}{\gamma_e m} \approx \frac{2\pi f_m \phi_n m}{\gamma_e m} \approx \frac{2\pi f_m \phi_n}{\gamma_e}, \tag{3.15}$$

where m is the slope of the FM-ODMR curve, and ϕ_n is the PLL phase noise with a measured value of -88 dBc/Hz (see Fig. 3-21) at an offset equal to the FM modulation frequency (f_m=3 kHz). The magnetic sensitivity calculated from Eq. 3.15 is ~30 pT/Hz$^{1/2}$, which is much smaller than that from Eq. 3.10 and confirms that the PLL noise does not limit the sensitivity.

3.2.3 Performance Comparison

The prototypes in Chapter 2 and Chapter 3 [38, 39, 47, 48] present vector-field magnetometers, which are based on a CMOS chip-scale platform with a hybrid integration of color centers (NV centers) in diamond. The hybrid chip-scale implementation consists of the essential components for manipulation and detection of the spin states of the NV centers in diamond. In our second prototype (Chapter 3 [48]), we demonstrate room-temperature magnetic field sensing with a sensitivity of 245 nT/Hz$^{1/2}$, which is 130× better than our previous prototype [39]. This enhancement is mainly due to the following: (i) the microwave launcher with uniform microwave generation that can be scaled up for large diamond area (i.e. large SNR). The area in this work increases by ~10×, resulting in ~10× better SNR. (ii) An enhanced multi-layer nanophotonic filter for lower background noise. The green rejection is enhanced by ~20×. This translates to $\sim\sqrt{20}\times$ or 4×-5× less green shot noise. (iii) The extra ~10× rejection of the external laser fluctuation due to the differential measurement. It is important to note that, the direct comparison between the two systems is not straightforward, due the discrepancies between the two test setups. For instance, less laser pump power is used in this scalable prototype (200 mW) compared to the one in [39] (500 mW), and there is an extra $\sim\sqrt{2}\times$ increase of readout-circuitry noise due to the two paths used in the differential measurement presented in this chapter. Table 4.1 shows a summary of the performance of the two prototypes.

Table 3.1: Summary of the hybrid CMOS-NV magnetometer performance and comparison with the prior art

References	Scalable Hybrid Magnetometer [48]	First Hybrid Magnetometer Prototype [39]
CMOS Process	65 nm	65 nm
Microwave Launcher	Wire Array (Scalable)	Loop Inductor (Non-Scalable)
Photonic Filter	Three-Layers (Plasmonic & Talbot Effect)	One-Layer (Plasmonic Effect)
Overall Green Light Rejection †	33 dB	20 dB
Sensing Area	80 µm × 300 µm	50 µm × 50 µm
Vector Field Sensing	Yes	Yes
Sensitivity	245 nT/Hz$^{1/2}$	32 µT/Hz$^{1/2}$

†The overall green rejection due to the on-chip filter and the diamond cut.

Chapter 4

Package-Less Cryptographic THzID

Radio-frequency identification (RFID) tags have been widely adopted in tracking, authentication, localization, supply-chain management, etc. [61]. At present, commercial RFID chips rely on external antenna or inductor packaging to facilitate efficient coupling of the RF waves. That, however, significantly increases the overall size of the tag, making it impossible to be attached to small objects such as medical pills, tooth implants and semiconductor chips. The associated authentication and recording of manufacturing data, therefore, can only be realized indirectly through special treatments (e.g. holographic patterns) on the goods packages, which leave loopholes for counterfeiting. Another barrier for RFID applications is the additional cost associated with the chip packaging, which takes up to two thirds of the total tag cost [62, 63]. That makes RFID technologies much less competitive than, for example, printed barcodes for low-cost products (e.g. a 50-cent candy bar) [61]. Lastly, it is noteworthy that pervasive electronic tagging raises serious privacy concerns related to inadvertent and malicious tracking of the tagged assets. Other sensitive data related to, for example, finance and personal health, are also increasingly generated by RFIDs. However, high-security encryption and authentication protocols normally require intensive computing, making reliable data protection difficult to realize in power/hardware-constraint RFID operation environments.

In order to enable secure and ubiquitous asset tagging, fully-passive, particle-sized cryptographic chips without external packaging are highly desired. However, the

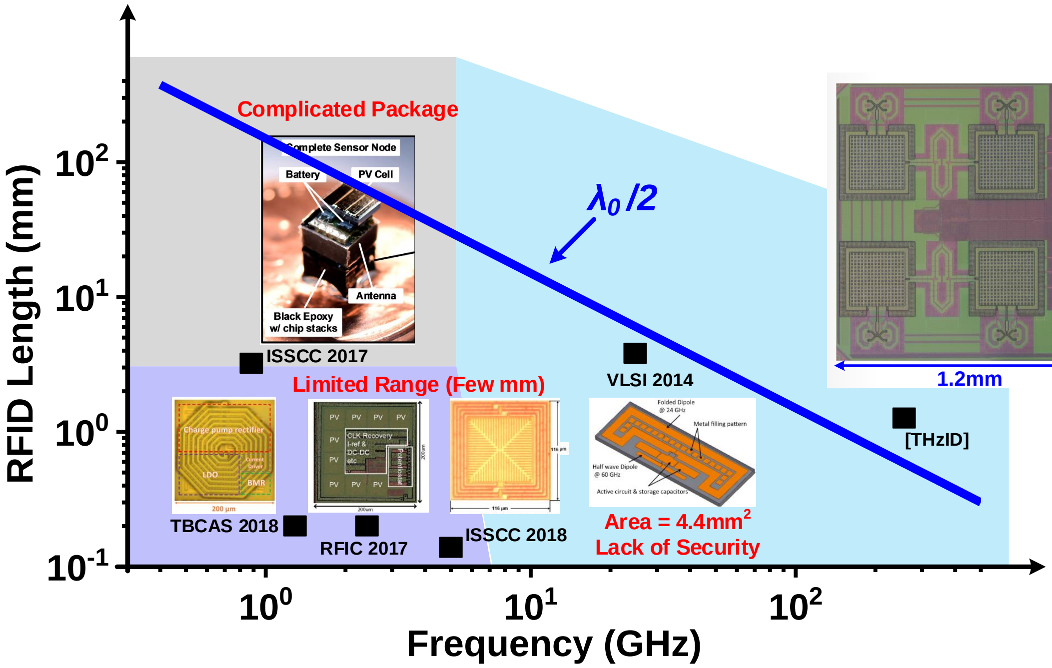

Figure 4-1: Comparison of the on-chip RFIDs.

recently demonstrated prototypes [64–70] (summarized in Fig. 4-1) that took the above path face either size, energy, communication or security limitations. In [64], a 9-mm^2 sensor node (volume=27 mm^3) is implemented out of a stacked packaging of multiple functionality layers for photo-voltaic powering, battery, antenna, etc, which increases the overall cost. The size can be pushed to ∼100 µm as demonstrated in [65–67]. However, the communication range is very limited (∼1 mm). For instance, in [65], a 116×116 µm^2 monolithic radio chip is demonstrated, but it relies on near-field inductive coupling at 5.8 GHz, which severely limits the operation range to ∼1 mm. In comparison, far-field tag interrogation using resonant antennas effectively increases the range. Using this principle, a pad-less chip with 24-GHz downlink and 60-GHz uplink boosts the range to 50 cm [68], but the chip-integrated transmitter (Tx) and receiver (Rx) antennas also increase the chip size to 3.7×1.2 mm^2. While this is already an impressive form factor, to fully enable the applications described previously, a further miniaturization is desired. It is also noteworthy that the above three works [64, 65, 68] also do not support cryptographically secure identification. To this end, [69] demonstrates a secure authentication tag, but the chip requires an

8-mm^2 external antenna; moreover, only a symmetric-key cryptography is realized due to the limitations of size and energy.

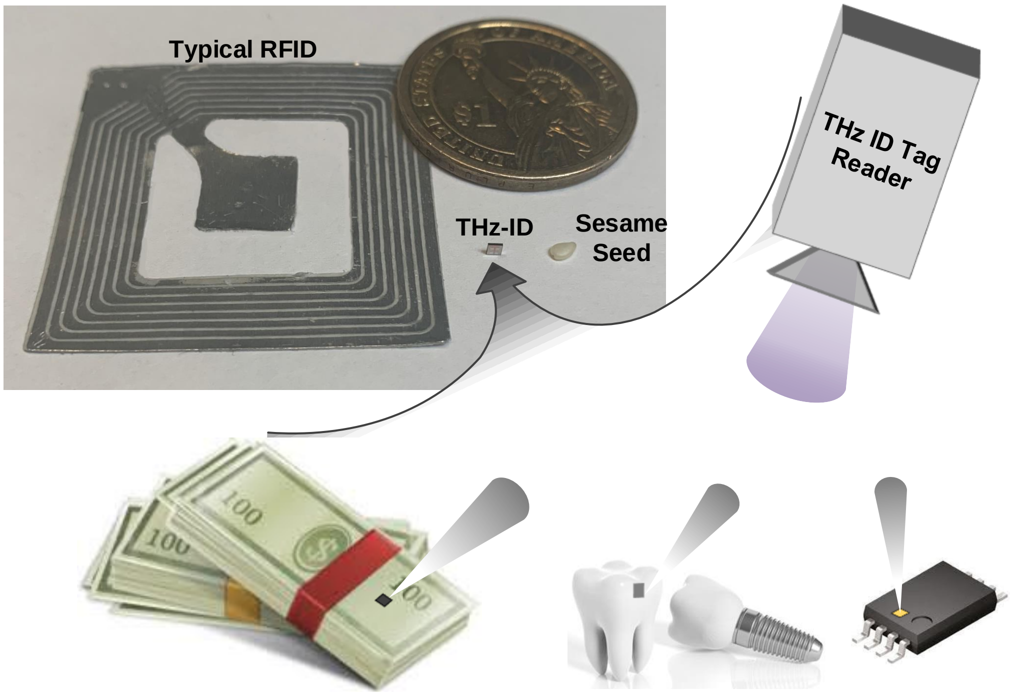

Figure 4-2: Cryptographic THz-ID tag: a size comparison and its potential applications.

In this chapter, we present a package-less, monolithic tag chip in CMOS, that has a size of 1.2×1.3 mm^2 (shown in Fig. 4-2) [71, 72]. To enable far-field operation with such a small form factor, the downlink/uplink carrier frequency is pushed into the low terahertz (THz) regime (260 GHz). That, along with a Tx-Rx antenna sharing technique, allow for an on-chip integration of a 2×2 antenna array and a tag-side, beam-steering capability. An operation range of 5 cm is demonstrated, which makes barcode-reader-like applications possible. Meanwhile, an ultra-low-power elliptic-curve-cryptography (ECC) dedicated processor is integrated in the THz-ID chip, which provides high-security compact asymmetric encryption. The whole chip consumes a peak power of 21 μW, which is provided by an array of chip-integrated photodiodes.

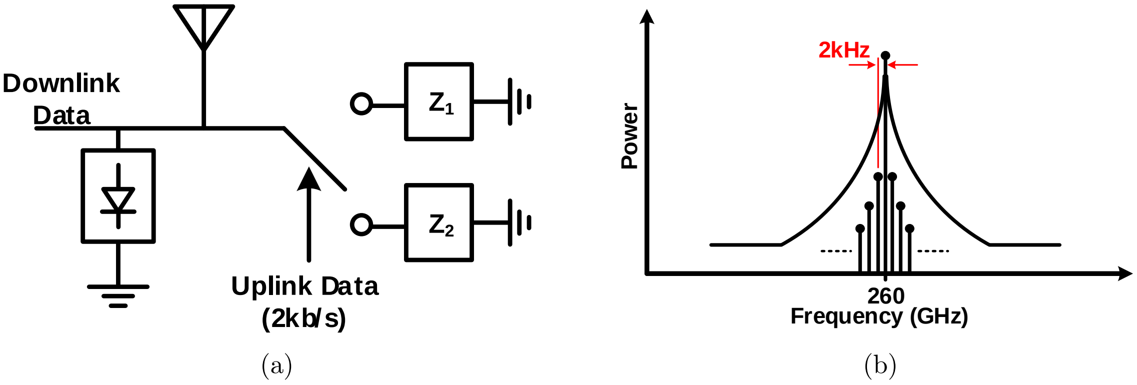

Figure 4-3: (a) Conventional RFID architecture. (b) A conceptual spectrum of OOK modulated back-scattered signal with data rate of 2 kbps

4.1 Proposed THzID Hardware Architecture

Conventional RFIDs are based on antenna impedance modulation to back-scatter the tag data (Fig. 4-3a). By changing the antenna impedance, the amplitude or the phase of the reflection coefficient changes. To enable THz operation (260 GHz), the carrier frequency of conventional RFIDs (few GHz) increases by $\sim$100×. Consequently, the phase noise increases by $\sim$40 dB. Therefore the signal can be submerged in the phase noise skirt, degrading the *SNR*. A conceptual plot of the spectrum of ON/OFF-shift-keying (OOK) back-scattered signal with data rate of 2 kbps is shown in Fig. 4-3b.

In this thesis, we propose a novel architecture to avoid the previously mentioned limitations. As shown in Fig. 4-4a, the downlink continuous wave beam (260 GHz) from the reader is received using one polarization (Pol. 1). Then, this signal is frequency-shifted by 2 MHz using a single-sideband mixer (SSB). Finally, the back-scattered signal is transmitted back on the orthogonal polarization (Pol. 2). As you can see in Fig. 4-4b, the proposed architecture helps in boosting the *SNR*, since the wanted modulated signal is pushed away from the high phase noise. In addition, the carrier phase noise is further reduced by $\sim$20 dB due to the cross polarization rejection.

The schematic of the overall architecture of the tag chip is shown in Fig. 4-5. The incident 260-GHz wave (red) from the reader is coupled to a 2×2 array of on-chip

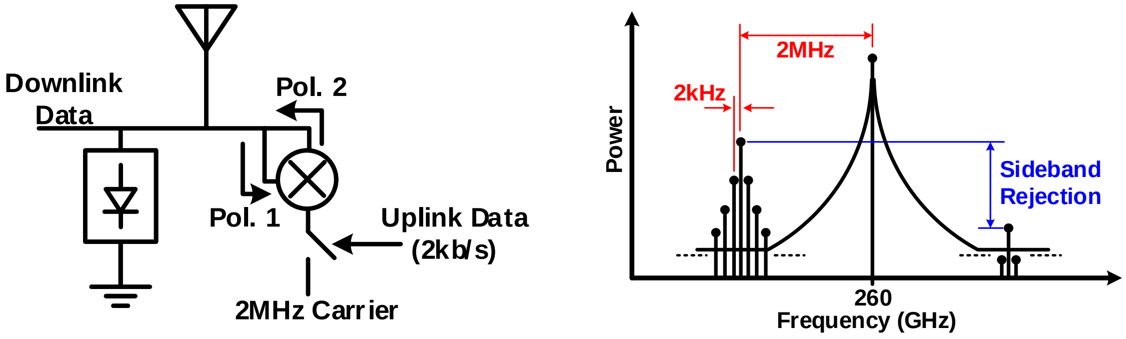

(a) (b)

Figure 4-4: (a) Proposed THzID architecture. (b) A conceptual spectrum of OOK modulated back-scattered signal with data rate of 2 kbps and a frequency-shift of 2 MHz

patch antennas. The THz signal with a particular linear polarization received by each antenna is extracted from two sets of antenna feeds with a power-splitting ratio of ∼1:1. Half of this power, used for the downlink, is rectified to baseband via four THz square-law detectors. The other half of the input power is used for the back-scatter uplink communication. It is noteworthy that a strong, direct reflection of the incident downlink wave, due to the large surface of the object to be tagged, is inevitable. It is, therefore, critical to eliminate the interference of such reflected waves to the actual data-modulated signal, which is back-scattered by the chip. To this end, single-sideband (SSB) frequency mixing is added to the back-scattering process, so that the final carrier frequency for the uplink (f_{UL}) is ∼2 MHz below that for the downlink (f_{DL}). Meanwhile, the chip is designed so that the polarization of the back-scattered wave (blue in Fig. 4-5) is also rotated by 90°, so that the tag reader's receiver antenna with a linear polarization aligned with the back-scattered wave can further suppress the directly reflected wave by >20 dB. The cross-polarization scheme also allows for re-using the downlink antennas for uplink antennas, which reduces the tag area by ∼2x. More details of the antennas will be given in Section 4.2.1.

Both the downlink and the uplink utilize OOK modulation, and offer data rates at 100 kbps and 2 kbps, respectively. The THz SSB mixers for the frequency shifting of the uplink carrier are driven by four 2-MHz local-oscillator (LO) signals generated by an integrated cryptographic processor. With independent, digital control of the

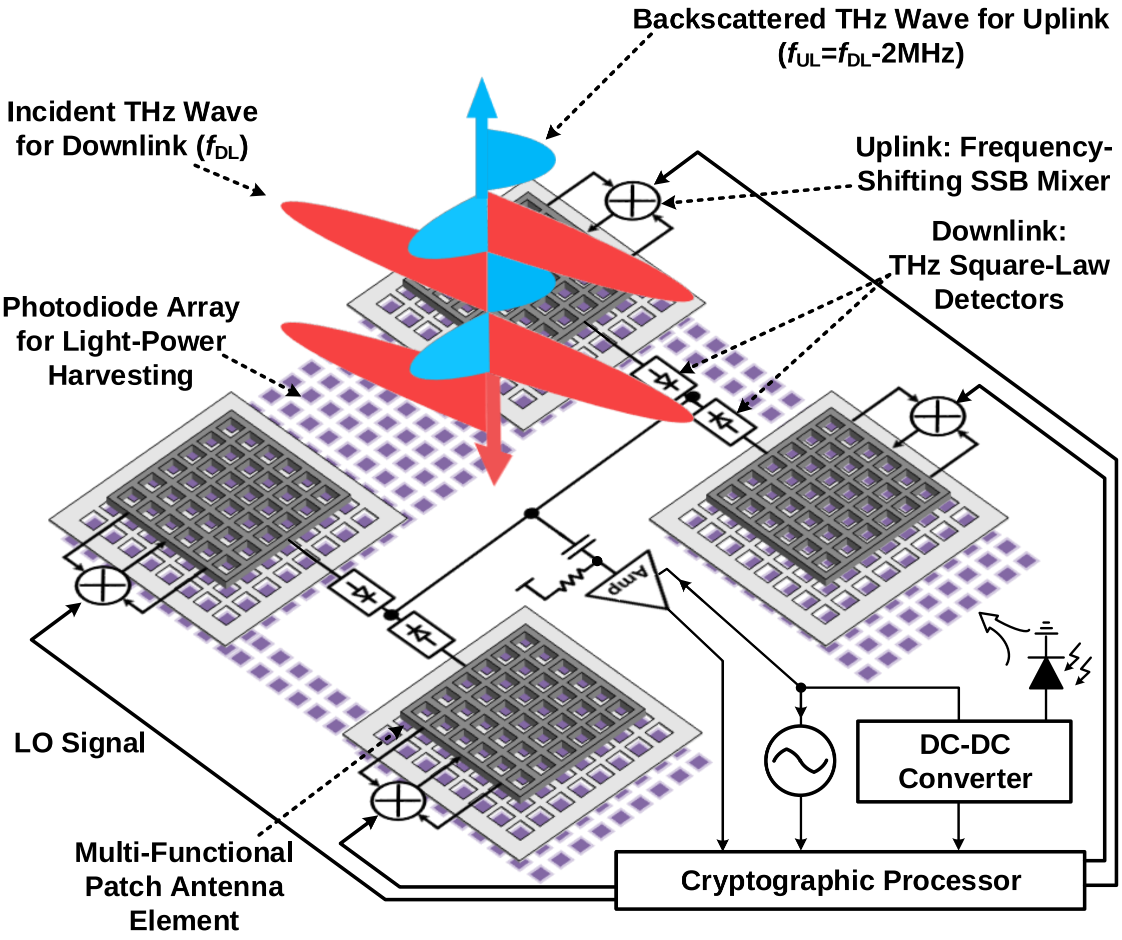

Figure 4-5: Overall architecture of the THz-ID tag.

phase in each LO, beam-steering for the THz uplink wave is achieved. That enhances the link budget when the tag is not perpendicularly facing the tag reader. Moreover, without the beam-steering capability, the tag would act like a mirror and make the backscatter communication more prone to eavesdropping.

In our protocol, the cryptographic processor first sweeps the uplink beam direction until reliable communication is established. Then it will work with the reader to perform a narrow-strong private identification protocol [73] under a public-key cryptography scheme (specifically elliptical-curve cryptography). It guarantees that any eavesdropper who does not possess the reader's private key cannot identify which tag participates in the protocol by merely monitoring the wireless link.

The photo-voltaic powering of the tag is realized through a large array of P-N photodiodes placed under and beside the antennas. To allow the incident light to reach the photodiodes, the patch and the ground plane of the antenna possess a fishnet pattern (Fig. 4-5). A DC-DC converter is implemented in order to boost the photodiode output voltage to ∼1 V. A 8-MHz oscillator is integrated to provide the LO signal for the THz SSB mixers, as well as the clock signals for the DC-DC converter and the cryptographic processor.

4.2 THz Downlink and Uplink

In this section, we describe the design of various tag components that enable 260-GHz communication with very small power consumption and chip area.

To enable front-side radiation, the tag integrates 2×2 patch antennas that are shared between the downlink and uplink. To realize such sharing, a near-square shape is adopted for the patch, so that its two dominant excitation modes i.e. TM_{100} and TM_{010} with orthogonal polarizations have the same resonance frequency (∼260 GHz). As Fig. 4-6 indicates, to excite a certain mode (TM_{100} in this case), we can either use a differential feed symmetrically connected to the patch edge along the x-direction (i.e. Feed 1), or a single-ended feed connected to the center of the patch edge along the y-direction (i.e. Feed 2). Therefore, when both feeds are used and the downlink wave aligns with the TM_{100} mode of antenna, the received power is split into the two feeds for backscatter (Feed 1) and downlink demodulation (Feed 2), respectively. Accordingly, the THz SSB mixer has a differential input, while the THz square-law detector for the OOK demodulation of downlink has a single-ended input (Fig. 4-6).

4.2.1 Multi-Functional On-Chip Patch Antenna

Next, to radiate the uplink signal with orthogonal polarization, the TM_{010} mode of the same antenna is used (Fig. 4-7) and is excited by a single-ended feed (Feed 3) at the center of the patch edge along the x-direction. Accordingly, the THz SSB mixer provides a single-ended output, as described later in Section 4.2.2. Note that the electrical field distribution of the associated TM_{010} mode has a null at Feed 2, so the leakage of the uplink signal to the THz square-law detector is very small. Similarly, the

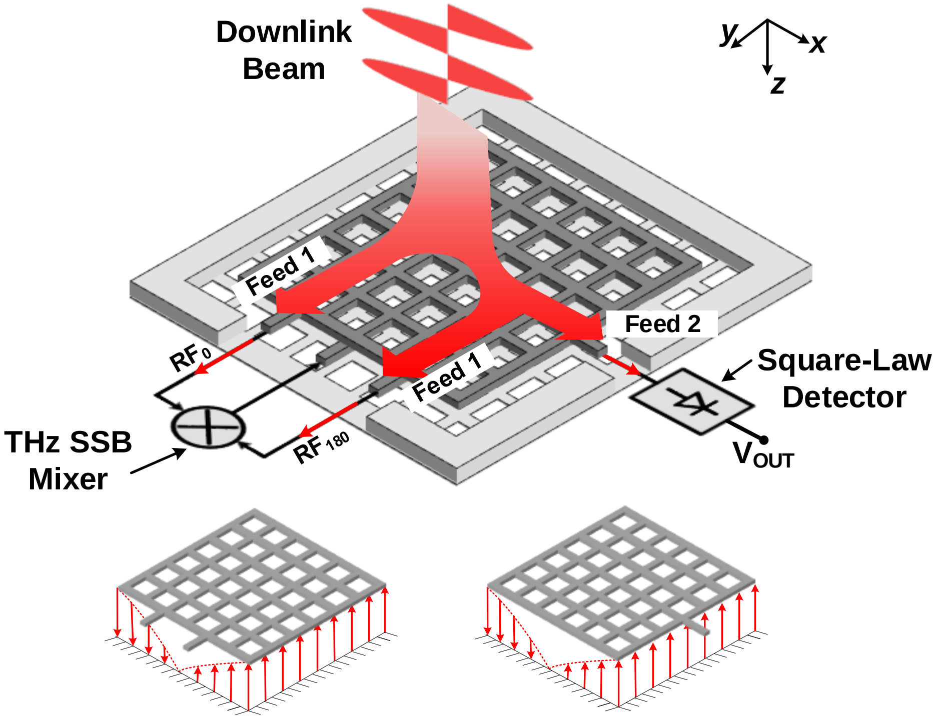

RX Mode (TM$_{100}$)
Differential Mixer Input

RX Mode (TM$_{100}$)
Common-Mode Detector Input

Figure 4-6: Schematic of the multi-port patch antenna with excited TM$_{100}$ for downlink.

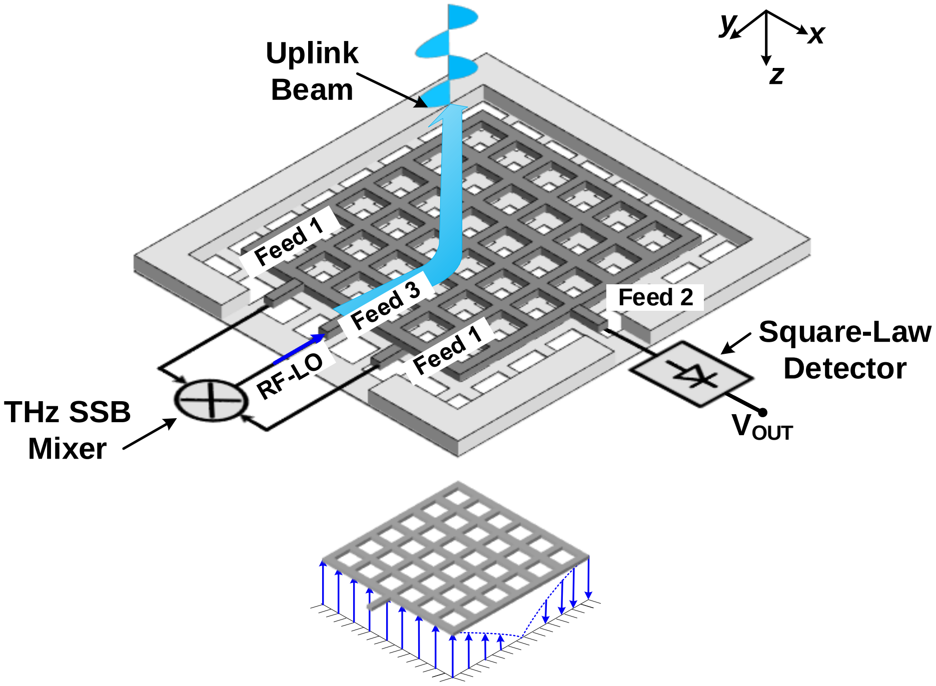

TX Mode (TM$_{010}$)
Common-Mode Mixer Output

Figure 4-7: Schematic of the multi-port patch antenna with excited TM$_{010}$ for uplink.

received downlink signal does not leak into the SSB mixer output either (Fig. 4-8a)[1]. To ensure the reliability of both the downlink de-modulation and the backscattering, the power splitting ratio in Fig. 4-6 is set to about 1:1. The value of the ratio is controlled by the termination impedances at Feed 1 and Feed 2 (i.e. Z_1 and Z_2 in Fig. 4-8a). To determine the optimal values of Z_1 and Z_2, we first derive the desired ratio of $K{=}Z_2/Z_1$. Note that for the TM_{100} resonance mode, the distribution of the electrical field (hence the local voltage with respect to ground) along x-direction approximately follows an anti-symmetric sinusoidal pattern (Fig. 4-8a), and can be expressed as [74]:

$$V(x) = V_0 \cdot \sin\frac{\pi x}{2L_{ANT}}, \tag{4.1}$$

where V_0 is the maximum RMS voltage at the edge of the antenna, and L_{ANT} is the dimension of the antenna. Therefore, the power injected into Z_1 and Z_2, respectively, is:

$$P_1 = \frac{4V_0^2}{Z_1}(\sin\frac{\pi L_1}{2L_{ANT}})^2 \quad \text{and} \quad P_2 = \frac{V_0^2}{Z_2}, \tag{4.2}$$

where L_1 is the distance of each Feed 1 wire from the antenna edge center (Fig. 4-8a). For equal power splitting (i.e. $P_1{=}P_2$), the required ratio K is derived:

$$K = \frac{Z_2}{Z_1} = \frac{1}{4(\sin\frac{\pi L_1}{2L_{ANT}})^2}. \tag{4.3}$$

In our design, the value of L_1/L_{ANT}, limited by the circuit floorplan, is about 0.18, which leads to $K{\approx}3$. Next, to further determine Z_1 and Z_2, we note that their optimal values should provide matching between the entire downlink structure and the incident plane wave. This scenario is emulated in a full-wave electromagnetic simulator, HFSS [37], with a far-field half-wave dipole antenna (Port 3 in Fig. 4-8a). The dipole has a gain of 2 dB and is located at 2 cm from the on-chip patch antenna. The absolute values of Z_1 and Z_2 are then swept (while keeping their ratio of $K{=}3$). When $Z_1{=}150\ \Omega$ and $Z_2{=}450\ \Omega$, maximum total power transfer from the feed dipole

---

[1] We, however, note that the uplink signal injected at Feed 3 can *couple back* to the SSB mixer through a *common-mode* leakage in Feed 1. Techniques to prevent such leakage are described in Section 4.2.2.

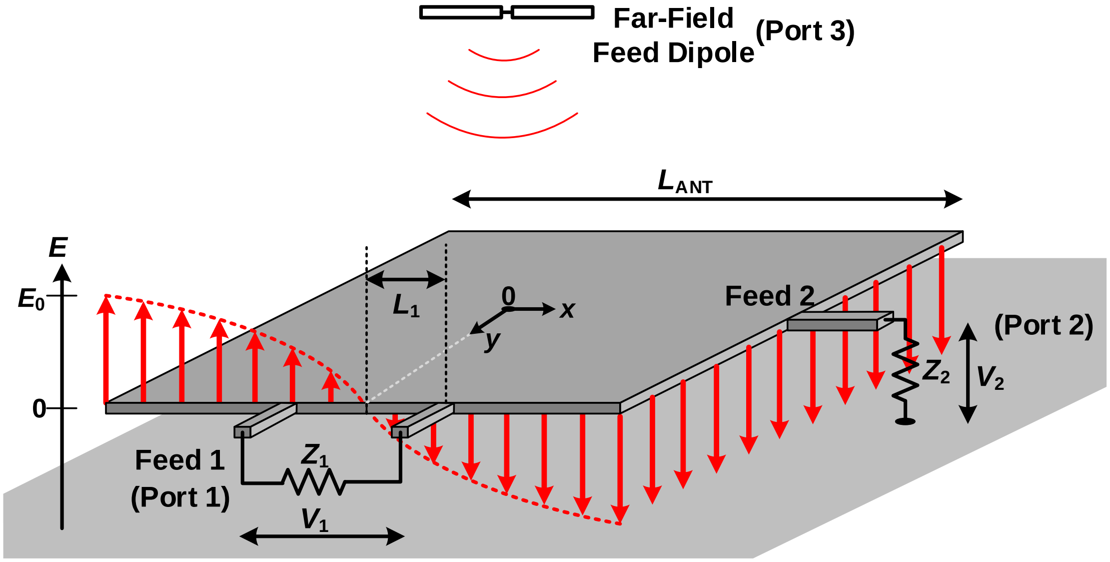

(a)

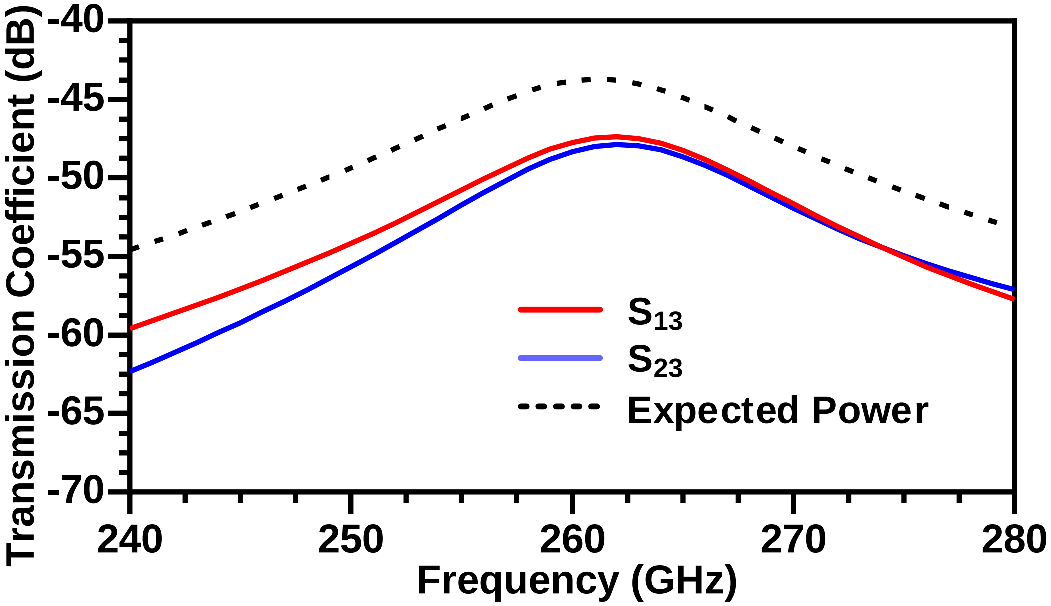

(b)

Figure 4-8: (a) The electrical-field distribution of the TM_{100} mode in the multi-port antenna. (b) The simulated power transmission coefficients from a far-field feed dipole (2 cm away) to the two ports associated with the downlink, when they are terminated by Z_1=150 Ω and Z_2=450 Ω, respectively. The dotted line shows the expected total received power, which includes the free-space propagation loss and the gains of two antennas. Ideally, it should be 3-dB higher than S_{13} and S_{23} when the power transmissions to Port 1 and 2 are equal and maximized.

to the two patch antenna ports (S_{13} & S_{23} in Fig. 4-8) is obtained, meaning that the wave reflection on the antenna is minimum. Figure 4-8b shows the simulated power transmission coefficient (including free-space propagation loss) when the above optimal impedance values are applied.

Regarding the implementation of the patch antenna, its radiator uses the top aluminium (Al-pad) layer of the CMOS process, and has a size of 271 μm in the x-direction and 235 μm in the y-direction. These dimensions, along with the additional feed ports, lead to the same resonant frequency for both TM_{100} and TM_{010} modes. The patch would have a square shape if only Feed 2 and Feed 3 were present but the differential Feed 1 necessitates a non-square shape. The ground plane of the antenna is made out of the M3 layer. The antenna is also enclosed by a ground wall (M3 to top aluminum layer), which is 20-μm away from the patch at all sides. That reduces the coupling with neighboring electronics and antennas while its effect on the antenna performance is negligible. Using HFSS the peak directivity and radiation efficiency of the antenna in the simulation are 6.7 dBi and 27%, respectively, in both resonant modes.

4.2.2 THz Frequency-Shifting Backscatter Module

Instead of using a dedicated Tx signal source on a tag [68], which is too power hungry to be practical for THz IDs, our uplink adopts an energy-efficient backscatter scheme for the incident wave. As described in Section 4.1, the backscatter module applies a frequency shifting to the THz signal. Shown in Fig. 4-9, the backscatter module consists of a passive single-sideband (SSB) mixer, two 90° Lange couplers and a balun. It takes the differential RF signal from the antenna, generates its quadrature phases, and then mixes it with a set of 2-MHz quadrature LO signals. The mixer output is finally injected back to the antenna. Next, details of the components in the backscatter module are given.

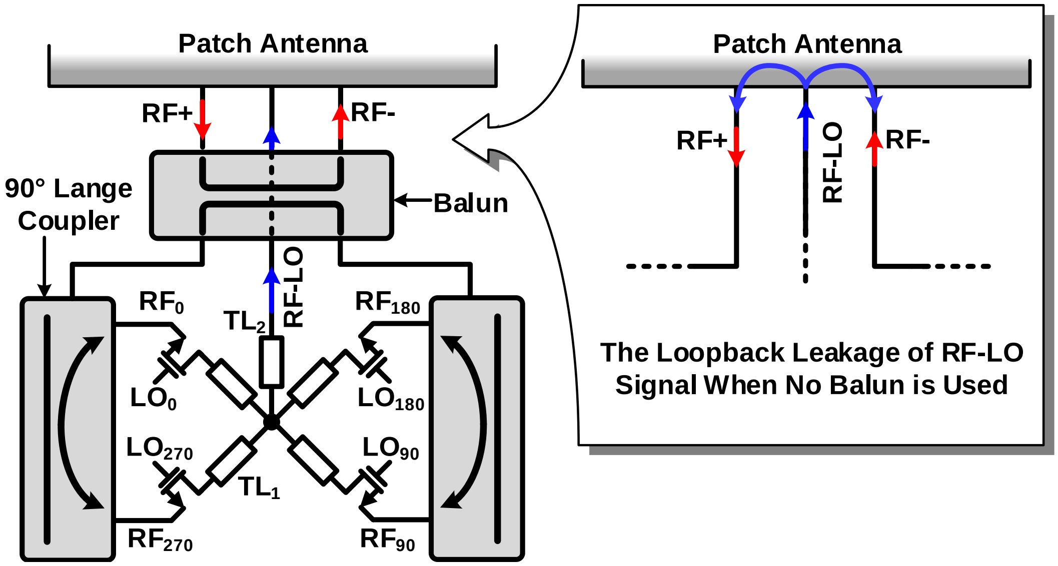

Figure 4-9: Schematic of the backscattering module consisting of a passive SSB mixer, a balun, and two 90° Lange couplers. The loopback effect with the absence of the input balun is also shown.

Input Balun

In Fig. 4-7, the TM$_{010}$ mode excited by the SSB mixer output presents a common-mode electrical field at the two wires of Feed 1. As a result, the mixer output will be fed back to the mixer and undergoes an extra down-shift by f_{LO} in each round trip. Such loopbacks therefore cause excessive signal loss and undesired LO harmonic spurs. To avoid it, between Feed 1 of the antenna and the SSB mixer input, a balun is inserted, which only allows the transmission of differential signal from the antenna, and blocks the common-mode leakage from the mixer output. A return-path-gap-based balun introduced in [75] is used, which consists of two microstrip lines coupled via a slot in the ground plane (i.e. return-path gap or RPG, see Fig. 4-10a). The RPG slot, closed by four quarter-wavelength slot resonators in the ground plane, only allows transmission (hence input-output coupling) of quasi-TE-mode wave, which is excited by a differential signal in the input microstrip lines. That is illustrated in the electromagnetic simulation shown in Fig. 4-10b, and we can see that the common-mode signal is effectively rejected. The simulated insertion loss for the differential mode is $\sim$1 dB and the rejection for the common mode is $>$10 dB from 240 to 280 GHz. The balun is implemented using 2-μm-wide M9 microstrip lines and slots in a shunted

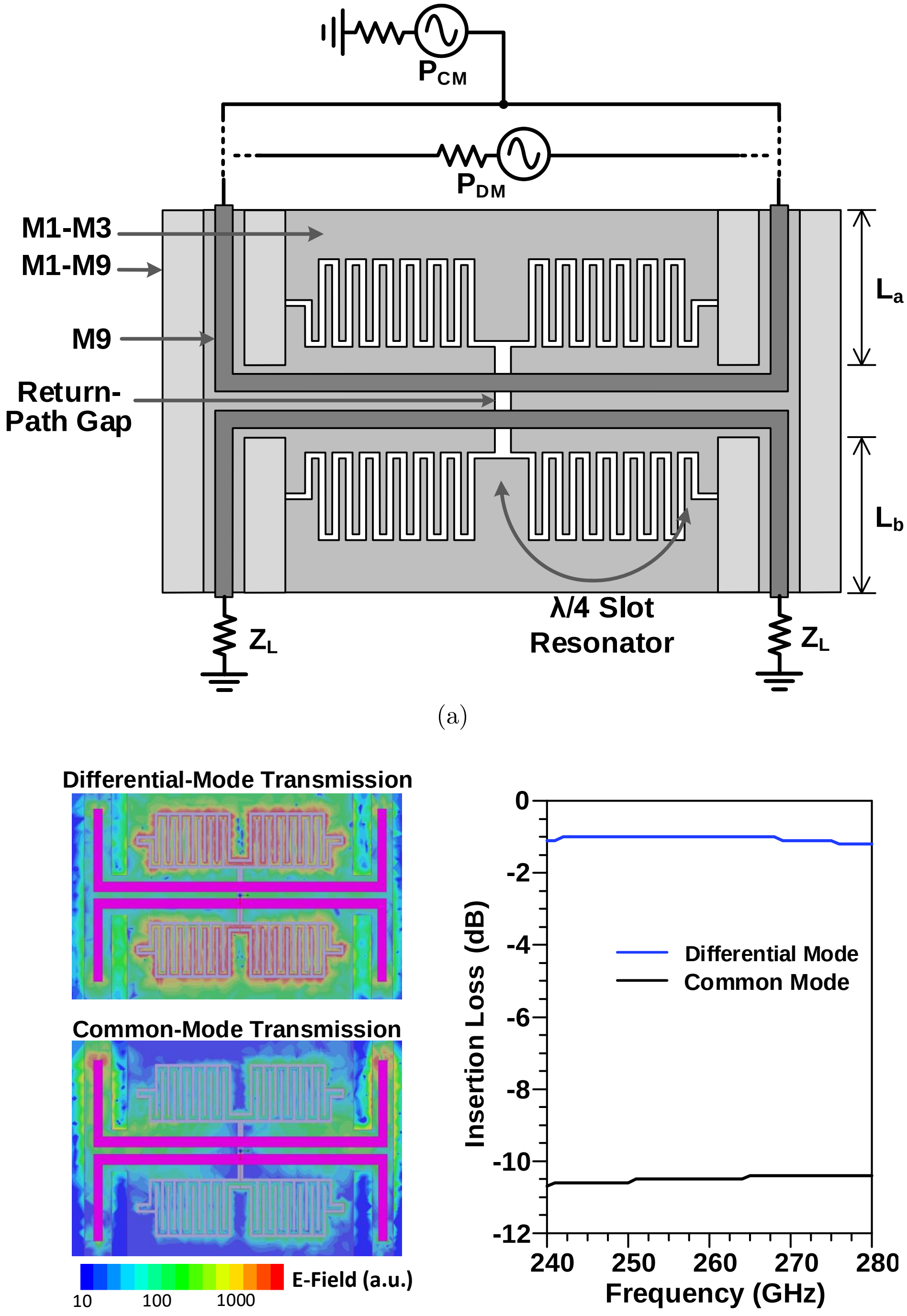

(a)

(b)

(c)

Figure 4-10: 260-GHz balun based on a return-path gap: (a) structure, (b) simulated electrical-field distribution, and (c) simulated insertion loss from the input to one load Z_L.

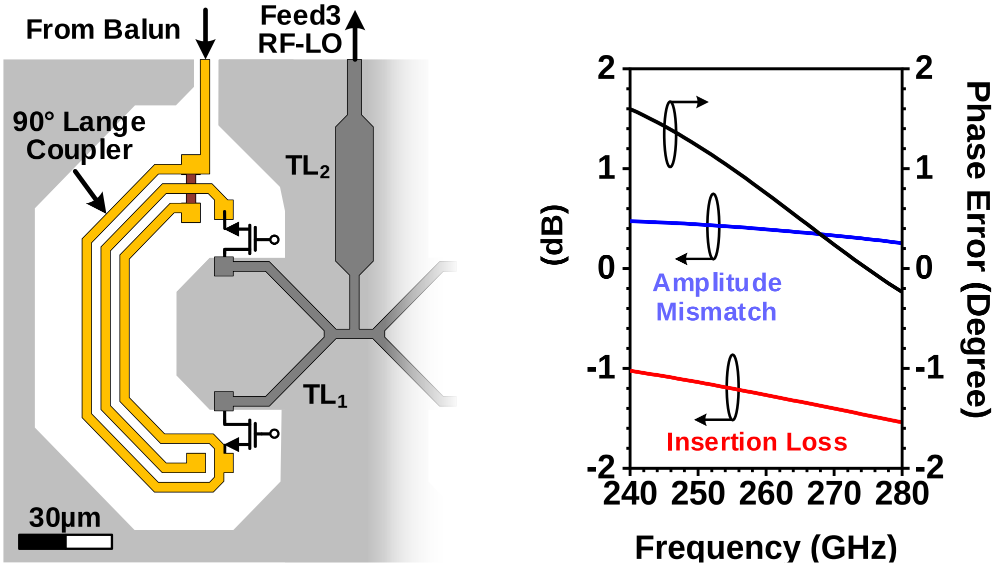

(a) (b)

Figure 4-11: (a) The structure of the 260-GHz Lange coupler in the backscatter module. (b) Simulated insertion loss and output mismatch of the coupler.

M1-M3 ground. Note that a wire placed along the central line of the balun connects the SSB mixer output (f_{RF}-f_{LO}) and the antenna (Fig. 4-9); since the balun central line can be treated as the virtual ground for the differential-mode transmission, the above wire does not interfere with the balun operation.

Coupler

The Lange coupler that generates the quadrature phases for the input 260-GHz signal is shown in Fig. 4-11a. The electromagnetic simulation results are shown in Fig. 4-11b; at 260 GHz, the simulated insertion loss excluding the ideal 3-dB power splitting factor is 1.2 dB, and the amplitude/phase mismatches at the two output ports are 0.5 dB and 0.5°, respectively. The couplers are implemented using the M9 layer, with 3-μm-wide lines and 3-μm spacing among the lines. The couplers are also enclosed by a ground plane (with a spacing of 15 μm to provide the signal's return path and to minimize the coupling to surrounding structures.

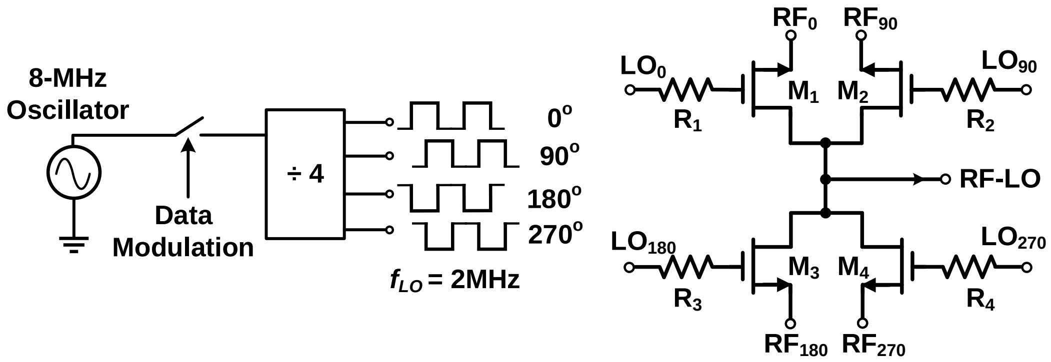

Figure 4-12: Schematic of the 260-GHz passive SSB mixer.

Passive Single-Sideband Mixer

Although a double-sideband (DSB) mixer involves simpler hardware implementation, we note that the generated upper and lower sidebands are applied with opposite phases from the LO; in our tag, therefore, their associated uplink beams would point to different directions in the beam-steering. That lowers the security and causes signal loss and interference. In our design, a SSB mixer based on passive quad switches is adopted to not only suppress the upper-sideband of the output, but also to minimize the power consumption. Shown in Fig. 4-12, the 2-MHz quadrature LO signals of the mixer are from an 8-MHz on-chip oscillator cascaded by a divide-by-4 static frequency divider[2]. The phases of the RF and LO signals of the MOSFETs are arranged in the way that at the central current-summing node, the lower-sidebands of all branches add up constructively, while the upper-sidebands cancel. MOSFETs in 65-nm bulk CMOS process have poor switching performance at THz; although wider channels provide smaller ON-resistance, there is also stronger coupling of THz signal from the channel to the LO wire through the gate-channel capacitance. To block such coupling, a set of 1.5-kΩ resistors ($R_1 \sim R_4$ in Fig. 4-12) are added in series with the transistor gates, which improves the mixer insertion loss from 15.5 dB to 13.5 dB in the simulation. Lastly, the OOK uplink modulation is realized by a data-controlled gating of the LO signals.

---

[2] Although a divide-by-2 operation for a 4-MHz signal also provides the 2-MHz quadrature LO signal, the additional availability of LO phases (e.g. 45°, 135°, 225°, 315° in Fig. 4-12) provided in our divide-by-4 scheme is utilized to demonstrate the beam-steering of uplink wave.

Shown in Fig. 4-11a, microstrip TL_1 lines combine the drain nodes of the MOSFETs and TL_2 is used to assist the impedance matching to Feed 3 of the antenna. But TL_2 falls short to provide ideal transformation and the limited space (due to the presence of the balun) hinders the placement of additional matching network components. This impedance mismatch leads to an insertion loss of 2 dB from the mixer to antenna Feed 3.

The simulated differential impedance of the whole backscattered module is very close to the desired 150 Ω (see Section 4.2.1) without any additional matching network. If necessary, the impedance matching can be fine tuned by controlling the lengths (L_a and L_b, see Fig. 4-10a) of the transmission lines connecting the balun to the antenna and coupler, respectively. The simulated common-mode impedance of the backscattering module is largely capacitive (4.2-347.4j Ω). The small real impedance ensures that the radiation efficiency for uplink signal is not affected by the loading at Feed 1.

In Fig. 4-13, we show the eletromagnetic-circuit co-simulation results of the entire backscatter module. An overall conversion loss of 18 dB (including the 2-dB impedance mismatch loss) is achieved at f_{RF}=260 GHz, at the expense of zero static DC power. The conversion loss should be improved with more advanced CMOS technologies. The module also effectively suppresses the components at $f_{RF}+f_{LO}$ and $f_{RF}\pm 2f_{LO}$. The component at $f_{RF}+3f_{LO}$, due to its constructive summation at the mixer output node, appears at the output spectrum, with 10-dB rejection ratio. In the future, this may be improved by adopting a polyphase N-path mixer structure. Also note that the phase noise of the backscattered signal, being the sum of the RF and LO phase noise, is not deteriorated by the ultra-low-power tag LO; because the simulated tag LO phase noise is still smaller than that of the RF signal, due to the large difference between the two signal frequencies (i.e. 2 MHz versus 260 GHz).

4.2.3 THz Downlink Circuits

For the de-modulation of the 260-GHz OOK downlink signal, a THz square-law detector is used to first rectify the input to baseband, then a low-power amplifier is

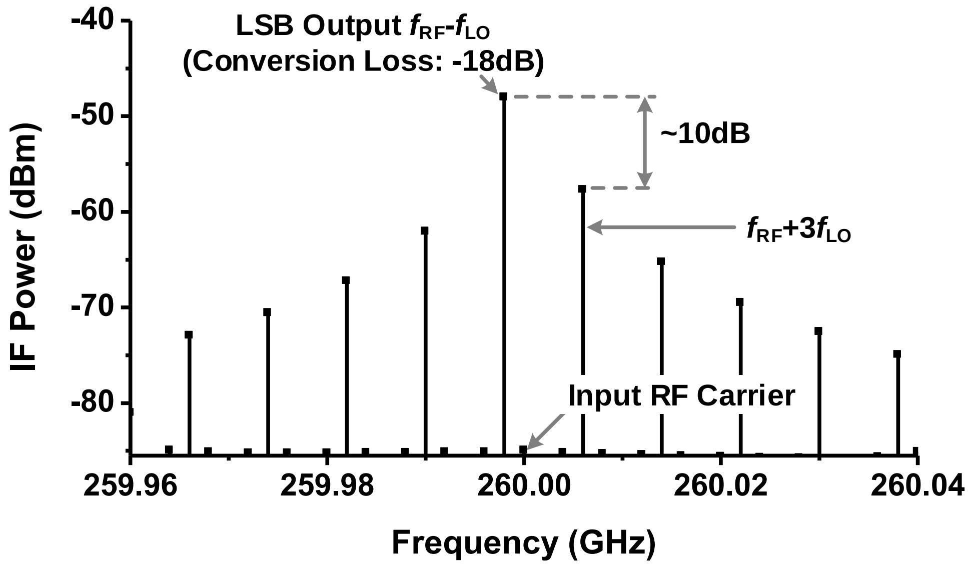

Figure 4-13: Simulated output spectrum of the THz backscatter module with a -30-dBm RF input (f_{RF}=260 GHz) and quadrature LO signals at f_{LO}=2 MHz.

used to boost the baseband signal to a few hundred mV, so that the subsequent digital circuits can operate reliably (Fig. 4-5).

THz Square-Law Detector

To achieve zero DC power and low flicker noise, our 260-GHz square-law detector is based on a 2.4 µm/65 nm NMOS device with zero drain bias. Similar to other FET-based THz detectors [76, 77], the optimal responsivity and noise-equivalent power (NEP) occur at a gate bias around the threshold voltage V_T of the transistor. Conventional VDD-powered circuits, due to the tag's energy harvesting operation, have large bias voltage fluctuation. Fortunately, in our CMOS process, the threshold voltage ($V_T \approx 0.4$ V) is close to the light-insensitive, open-circuit voltage of a P-N photodiode ($V_{PD} \approx 0.47$ V). Therefore, a simple photovoltaic-biasing circuit shown in Fig. 4-14 is adopted. Next, we note that any THz-power leakage to the biasing photodiode and detector baseband output should be avoided. To this end, a dual-detector scheme shown in Fig. 4-14 is used, which utilizes the property that the THz downlink signals extracted respectively from the adjacent edges of two patch antennas (see Fig. 4-5) are differential. As a result, in the symmetric circuit topology in Fig. 4-14, virtual RF grounds are formed at Node A and B. Furthermore, TL_2 and

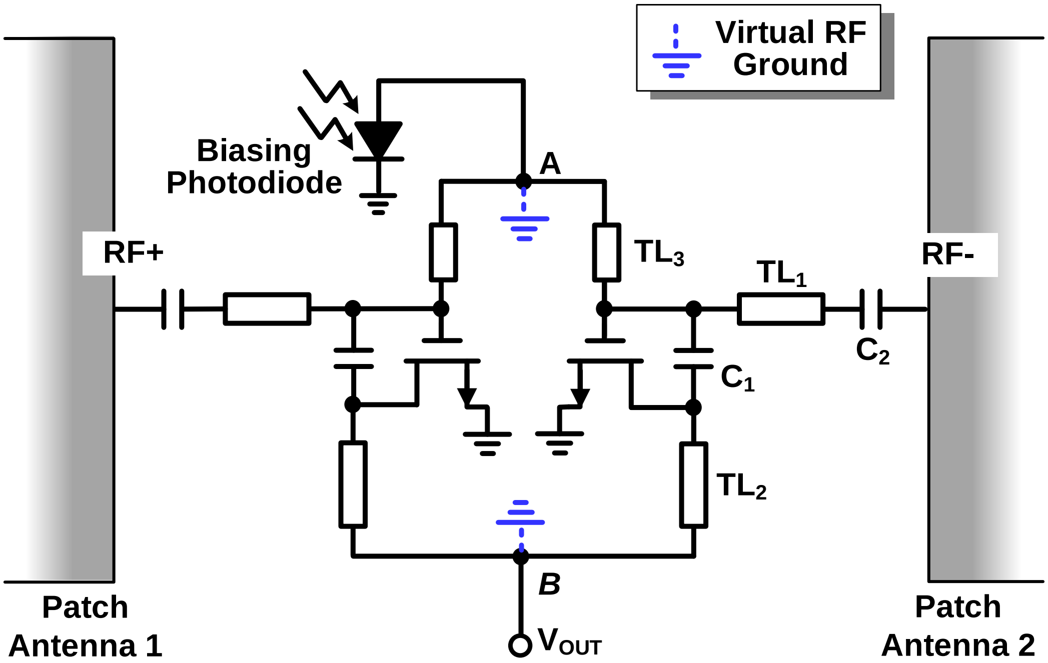

Figure 4-14: Schematic of a photovoltaically-biased THz square-law detector pair.

TL$_3$ are quarter-wavelength transmission lines; they transform the virtual ground to high impedances at the drain and gate of the MOSFET and therefore, highly confine the THz wave within the device. It is noteworthy that since the two differential THz inputs carry the identical OOK envelope, the baseband output from the two MOSFETs is in-phase, and is therefore combined and extracted at Node B.

In Fig. 4-14, C_1 ($\sim$50 fF) creates an AC short and therefore facilitates THz self-mixing in the diode-connected MOSFET. C_2 ($\sim$15 fF) provides DC isolation from the uplink backscatter module, and together with TL$_1$ (0.35λ) forms a matching network to present an impedance that is derived in Section 4.2.1 for equal power splitting. The insertion loss of the matching network is 1 dB. TL$_1$$\sim$TL$_3$ are 75 Ω coplanar-waveguide (CPW) transmission lines implemented using the M9 layer. As shown in Fig. 4-15a, the simulated overall impedance of the detector circuit is close to the desired impedance value of 450 Ω. Lastly, Fig. 4-15b shows that, at the photodiode bias voltage of $\sim$470 mV, the simulated responsivity and noise equivalent power (NEP) are 1 kV/W and 32 pW/Hz$^{1/2}$, respectively. Note that the NEP is limited by the channel thermal noise of the transistor. The noise voltage from the photodiode, calculated in [72], is

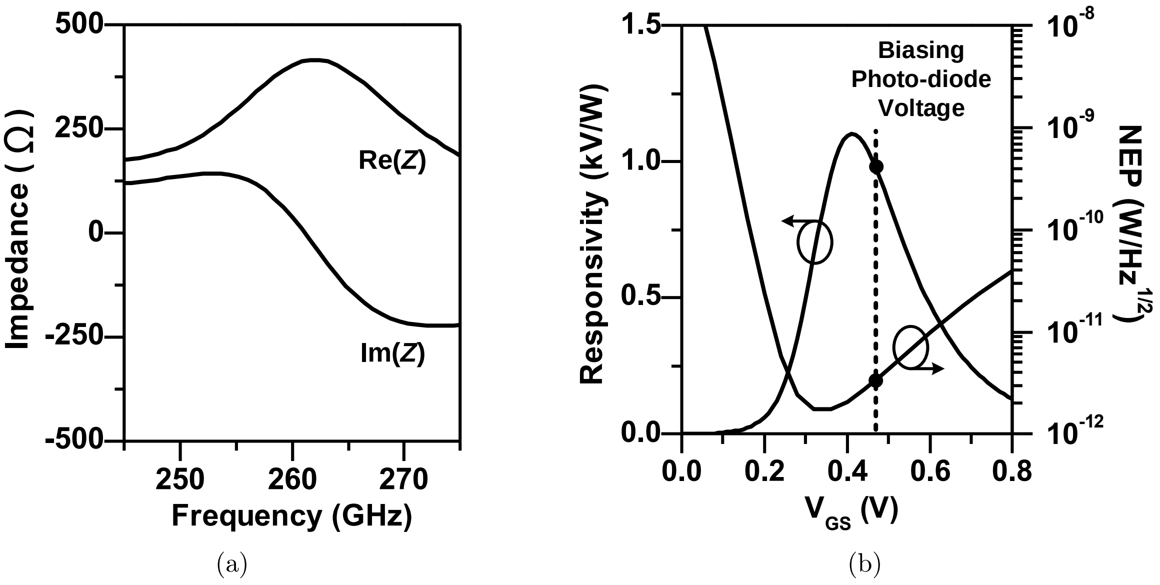

Figure 4-15: (a) Simulated impedance of the detector presented to Feed 2 of the antenna. (b) Simulated responsivity and NEP of the detector.

small, and does not transfer to the transistor output, given that the transistor is in the triode mode.

Ultra-Low-Power Amplifier

Shown in Fig. 4-16a, the demodulated signal from the detector is injected into a chain of amplifiers through a high pass filter. The filter, consisting of a 5 pF capacitor and a 5.7 MΩ resistor, has a low cut-off at 5 kHz, and provides not only the input bias of the amplifier but also DC isolation from the THz detector. The amplifier consists of three stages and two inverting buffers, and are separated by the same high-pass filters; this way the inevitable amplifier offset due to PVT variations and layout asymmetry is not amplified and saturates the circuits near the amplifier output.

Each amplifier stage consists of an input NMOS differential pair, which is preceded and followed by source-follower stages acting as voltage shifters. To save power, all amplifier stages are biased in the subthreshold regime. The bias voltage V_{BIAS} in Fig. 4-16a is generated from a cascode constant-g_m circuit (Fig. 4-16b). A reset signal RST from the tag's DC-DC converter is used to ensure that the biasing circuit jumps from an undesired meta-stable state to the normal state, when VDD ramps up to

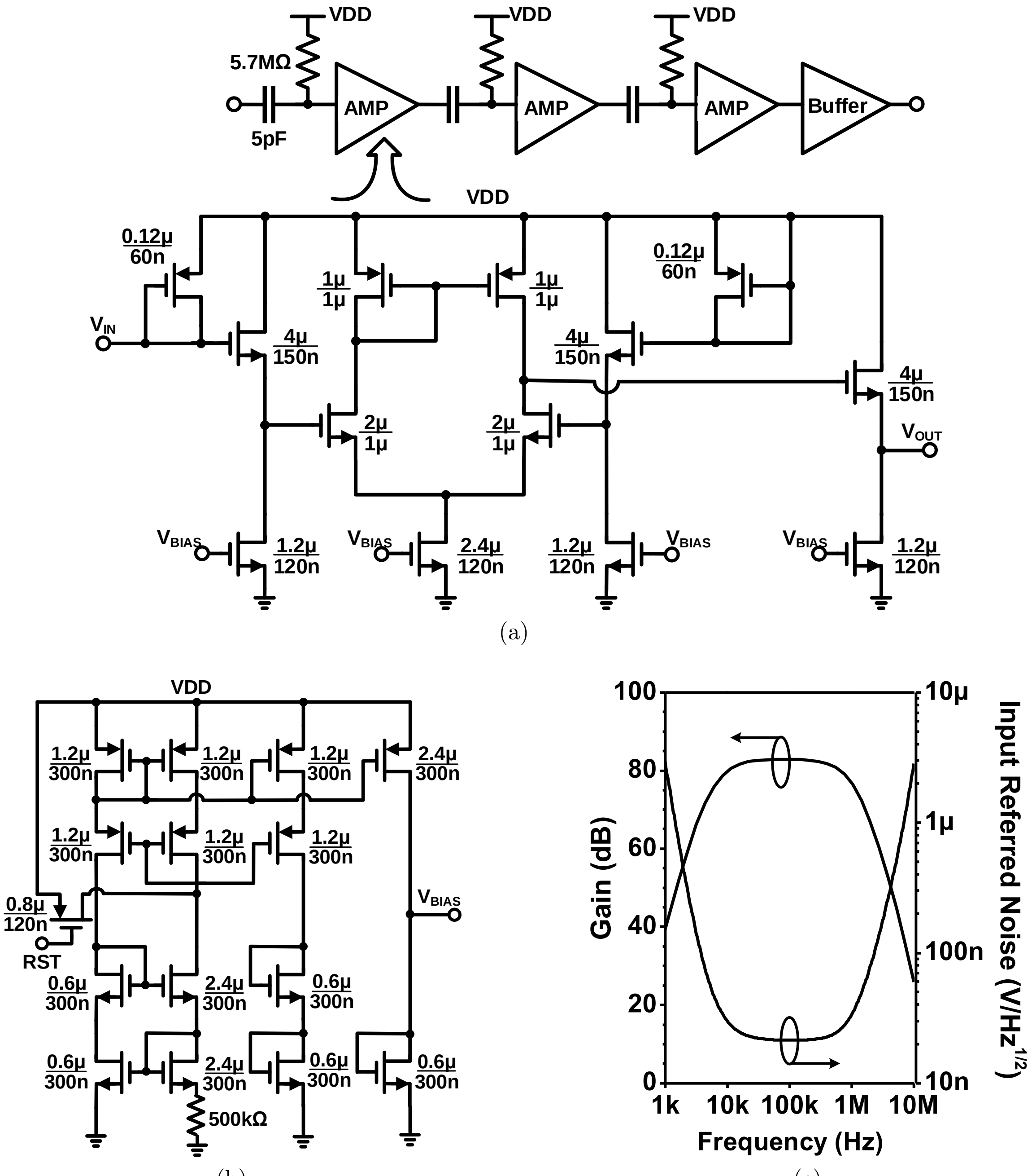

(a)

(b)

(c)

Figure 4-16: The ultra-low-power amplifier in the tag downlink: (a) the schematic of the main amplifier chain, (b) the cascode constant-g_m bias generation circuit, and (c) the simulated voltage gain.

$\sim$1 V. As shown in Fig. 4-16c, the simulated gain and the input-referred noise of the amplifier chain are 80 dB and 21 nV/Hz$^{1/2}$, respectively. The whole amplifier-buffer chain, including the biasing circuit, consumes only 1.5 μW.

The high gain is to ensure reliable toggling of subsequent digital circuits. It, however, also amplifies the noise, so when the THz detector is idle, the amplifier output has a low but non-zero probability of falsely toggling the succeeding digital buffer. To mitigate its impact, before taking any downlink message, the on-chip processor always first validates a 16-bit preamble in front of the message. When the THz detector outputs normal data in the downlink mode, the amplifier output level is sufficiently far away from the digital trigger threshold, and the noise impact is suppressed.

4.3 Cryptographic Security Processor

A cryptographic processor which implements a 128-bit secure ECC-based private ID scheme [73, 78] is used in the THzID. The scheme is a 3-move protocol where the tag chip uses its private key and the reader's public key in order to identify itself to the valid readers. The scheme guarantees that any eavesdropper who does not possess the reader's private key cannot identify which tag participates in the protocol by merely monitoring the wireless link. Fig. 4-17 shows the flow of the direction optimization and the authentication protocol between a THz secure tag and the THz tag reader. When powered using light, the tag wakes up and signals the same to the reader via a beacon. The beam direction is optimized by adjusting two antenna parameters, azimuth angle (ϕ) and elevation angle (θ), to maximize the link budget for data transmission. To this end, the whole space is divided into 25 possible angular positions: five in each azimuth and elevation directions with a step size of 45° from 0° to 180°. The tag wakes up with ϕ=0° and θ=90° by default, and then starts scanning. It takes $\sim$20 ms (limited by uplink data rate of 2 kbps) to complete the exchange of one beam direction message between the reader and tag. The total time for the beam search is therefore $\sim$500 ms. All THz tags are initialized with a unique private and public key pair (t, T=tP) and the reader has the tag's public key (T) registered in its database. The reader also

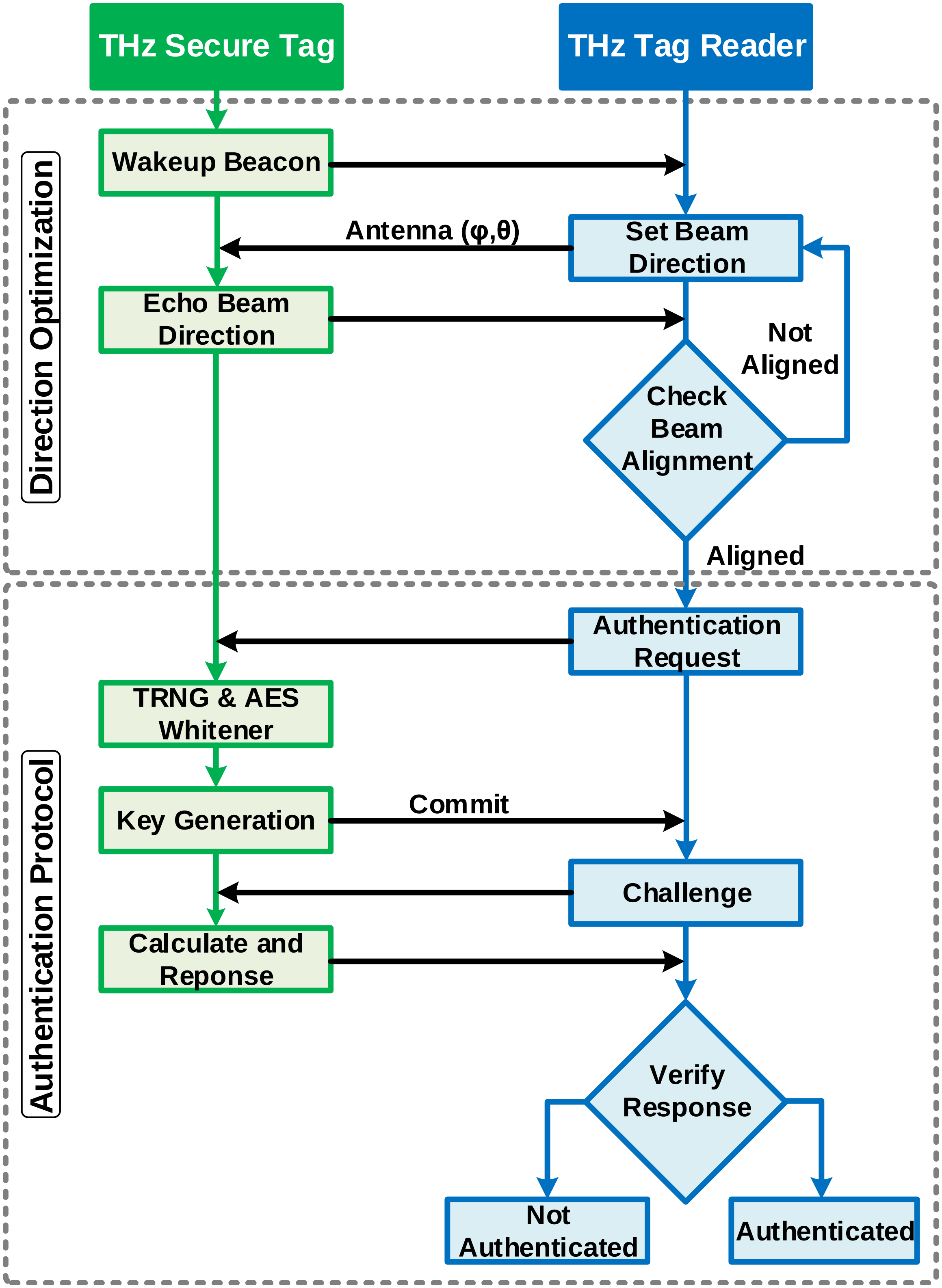

Figure 4-17: The security protocol between the THz secure tag and the tag reader.

has a private and public key pair (y, $Y{=}yP$) and the reader's public key Y is known to all tags. If the reader requests authentication of the THz tag, the tag commits a fresh random value ($R_1{=}r_1P$) where the randomness (r_1) is generated using the RO-TRNG and the 8-bit AES whitener. The reader responds to the tag's commit message with a random challenge ($R_2 = r_2P$) that is utilized by the tag to compute a Diffie-Hellman share (r_1r_2P). The tag then applies a one-way function to this share and calculates its response. This response is then verified on the reader side through a similar computation to authenticate the tag.

4.4 Integrated Photo-voltaic Powering

The antenna array, when incorporated on the tag chip, occupies most of the die area. In this section, we describe how the silicon under the antennas, along with an integrated DC-DC converter, are exploited to perform photo-voltaic powering for the tag.

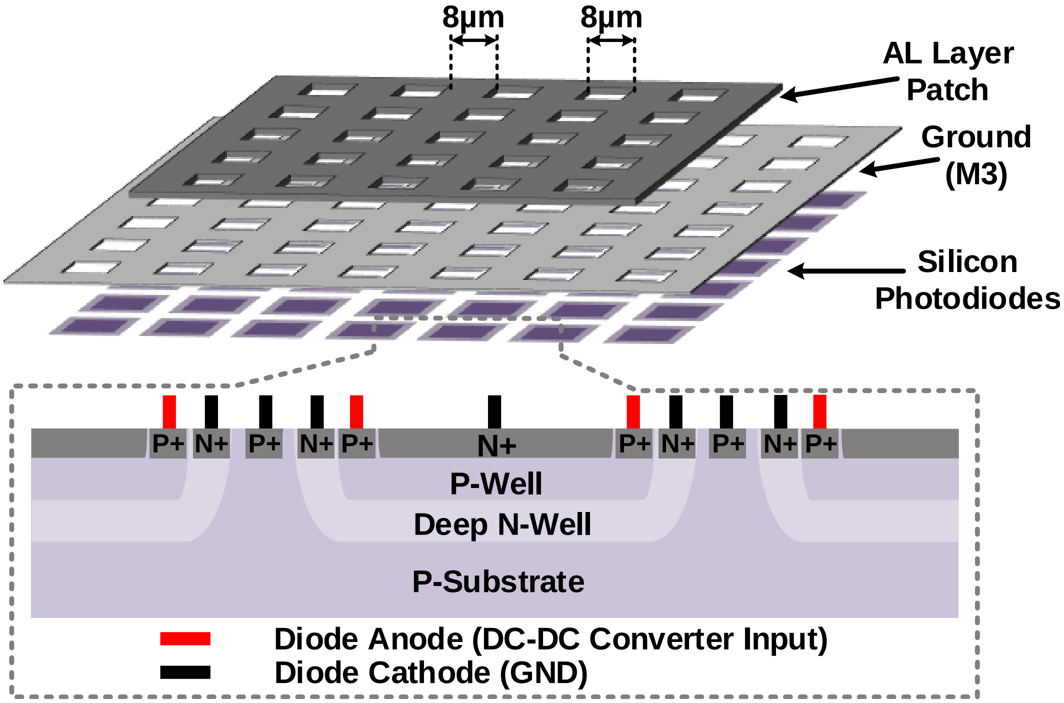

Figure 4-18: Photodiodes placed below patch antenna with fishnet pattern

The CMOS technology used for the chip provides a Deep N-well structure, normally for increased isolation between analog and digital circuits. This feature is utilized in the THz-ID tag, where silicon photodiodes are built based on a vertical stack of N+, P-well, Deep N-well and P-substrate, as shown in Fig. 4-18. As a result, three P-N junctions are formed, which maximize the absorption of incident light. For chip compactness, an array of shunted photodiodes are placed both beside and underneath the antennas. Correspondingly, the patch radiators and the ground planes of the antennas are implemented with a fishnet pattern (Fig. 4-18). A simulation tool based on a finite-difference time-domain (FDTD) method, Lumerical [44], is used to examine the hole size of the fishnet pattern. The simulation results in Fig. 4-19a assume that 25% area of antenna are holes to allow light transmission (refereed as fill factor of holes henceforth), and show that the through-hole light transmission for hole size smaller than 4 μm undergoes significant plasmonic and scattering loss. On the other hand, the hole size should remain a small fraction of the THz wavelength, so that the THz-field distribution over the antenna is not affected. As a result, a hole size of 8 μm, which leads to a through-hole light transmission rate of 92% is selected. For larger effective illumination areas, the fill factor of the holes should increase. That, however decreases the equivalent conductivity of the antenna metal layers, and lowers the radiation efficiency, as is shown in the HFSS simulation in Fig. 4-19b. In the tag chip, a fill factor of 25% is used, which slightly degrades the antenna efficiency from 31% to 27%.

The loaded photodiode output voltage at about 0.3 V is converted to the chip supply at 1 V using a DC-DC converter. The converter achieves a simulated conversion efficiency of 60% during peak power conversion, only using a tiny space (0.096 mm^2) between two patch antennas.

4.5 Experimental Results

The tag chip is fabricated using a TSMC 65-nm bulk CMOS process. The micrograph of the chip is shown in Fig. 4-20. The chip has an area of 1.3×1.2 mm^2. The two rows of pads, which can be cut, are for debugging purposes. In our testing, the chip is

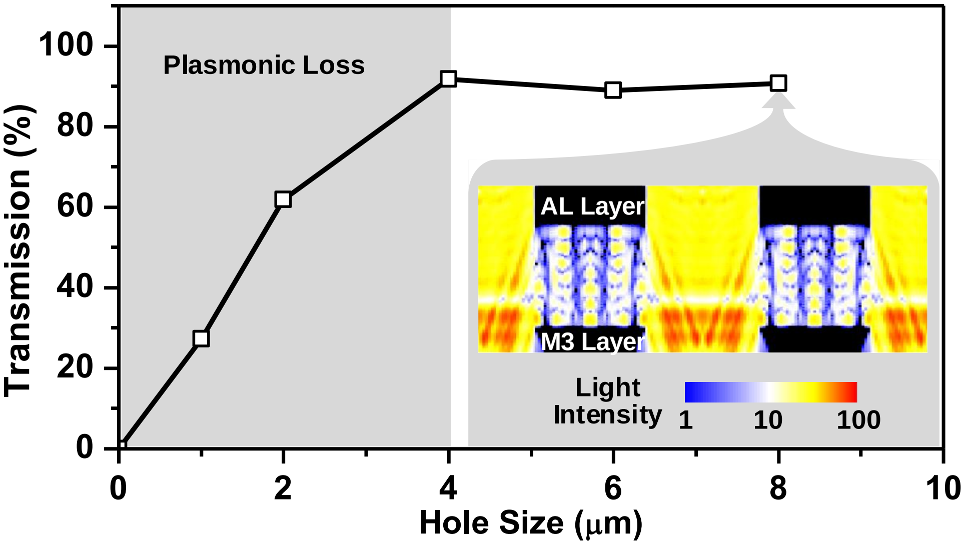

(a)

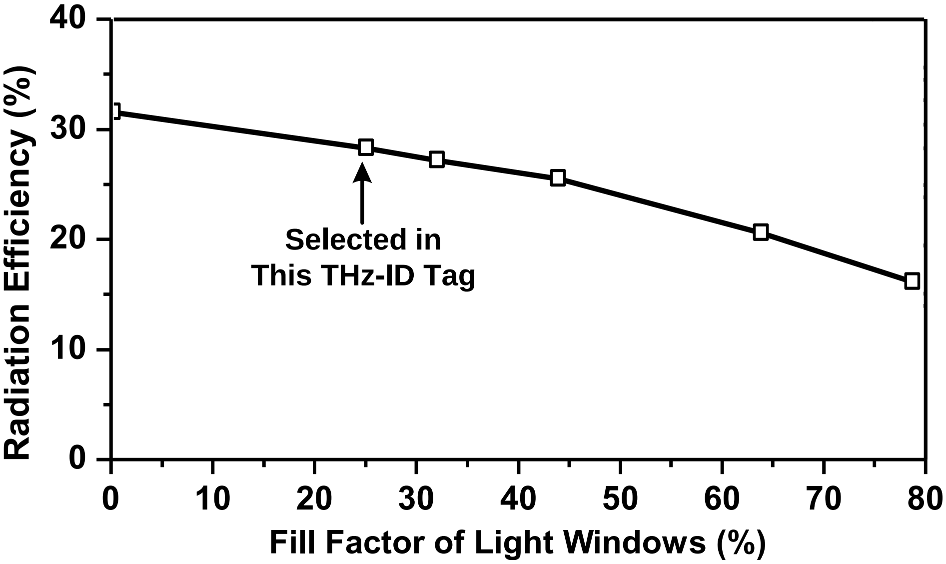

(b)

Figure 4-19: (a) FDTD-simulated light (λ=700 nm) transmission through different hole size. The cross-sectional view of intensity distribution for the hole size of 8 μm is also shown. (b) Simulated antenna radiation efficiency with different hole opening fill factor while keeping 8-μm hole size.

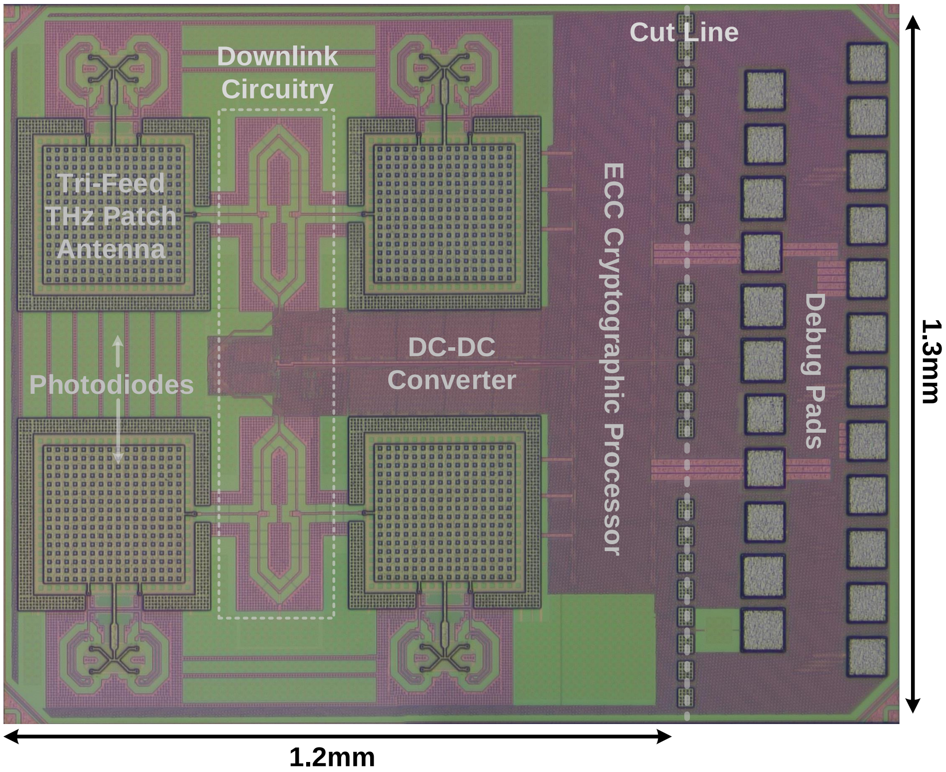

Figure 4-20: THzID chip micrograph

mounted and wire-bonded on a PCB.

4.5.1 Measurement Setup

First, a custom-designed THz-ID reader is constructed, as shown in Fig. 4-21. It communicates with the chip at a distance of 5 cm using two WR-3.4 horn antennas. The antennas are placed in the way that their E-planes are orthogonal to each other, in order to match the cross-polarizations of the THz-ID antennas (Fig. 4-6, and Fig. 4-7). For the reader-to-tag downlink, an amplifier-multiplier chain (AMC) from Virginia Diodes Inc. (VDI) is used, which converts a 10.9414-GHz input signal to a 20-dBm output at 262.5936 GHz. The input of the VDI AMC is OOK modulated by the 100-kbps data generated from a FPGA board (XEM 7001). According to the Friis formula [79], the power impinging on the THz-ID chip is about -5 dBm.

For the tag-to-reader uplink, a VDI spectrum analyzer extender (SAX) mixes the tag-backscattered signal with the 48^{th} harmonic of its 5.4632-GHz LO, and downconverts

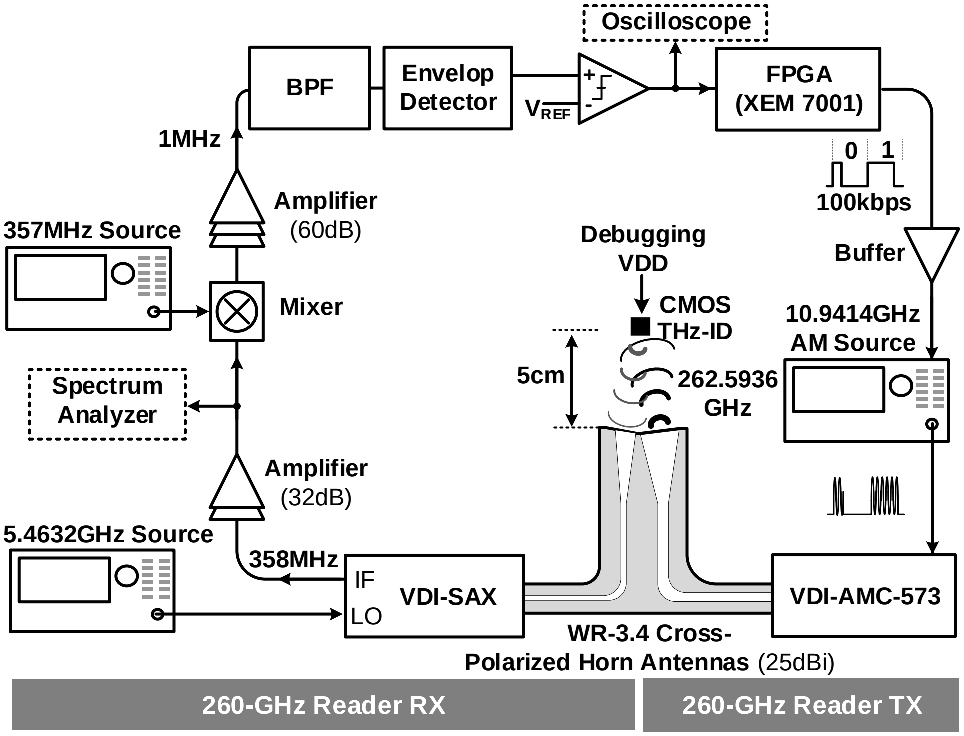

Figure 4-21: Diagram of the testing setup. Note that when light powering is used, the debugging VDD is disconnected.

to 358 MHz. The signal is then amplified by 32 dB and observed on a spectrum analyzer. To close the communication loop, the signal is also further downconverted to 1 MHz, amplified by 60 dB and bandpass filtered. Finally, an envelope detector cascaded by a comparator recovers the 2-kbps data and feeds to the FPGA (Fig. 4-21). Fig. 4-22 shows the photograph of the setup. The THz-ID reader head also includes an illumination source, which consists of a CREE XP-L-V6 LED and a lens that converge the light to ~1 cm^2 spot on the PCB. The chip PCB is mounted on a rotational stage, which is used for the beam-steering measurement. In the uplink and downlink modes, the tag consumes 13 µW of power; that includes 4 µW of static leakage power of the digital circuits. In the most power-hungry security mode, when the cryptographic processor is running RO-TRNG and AES, the power consumption rises to 21 µW.

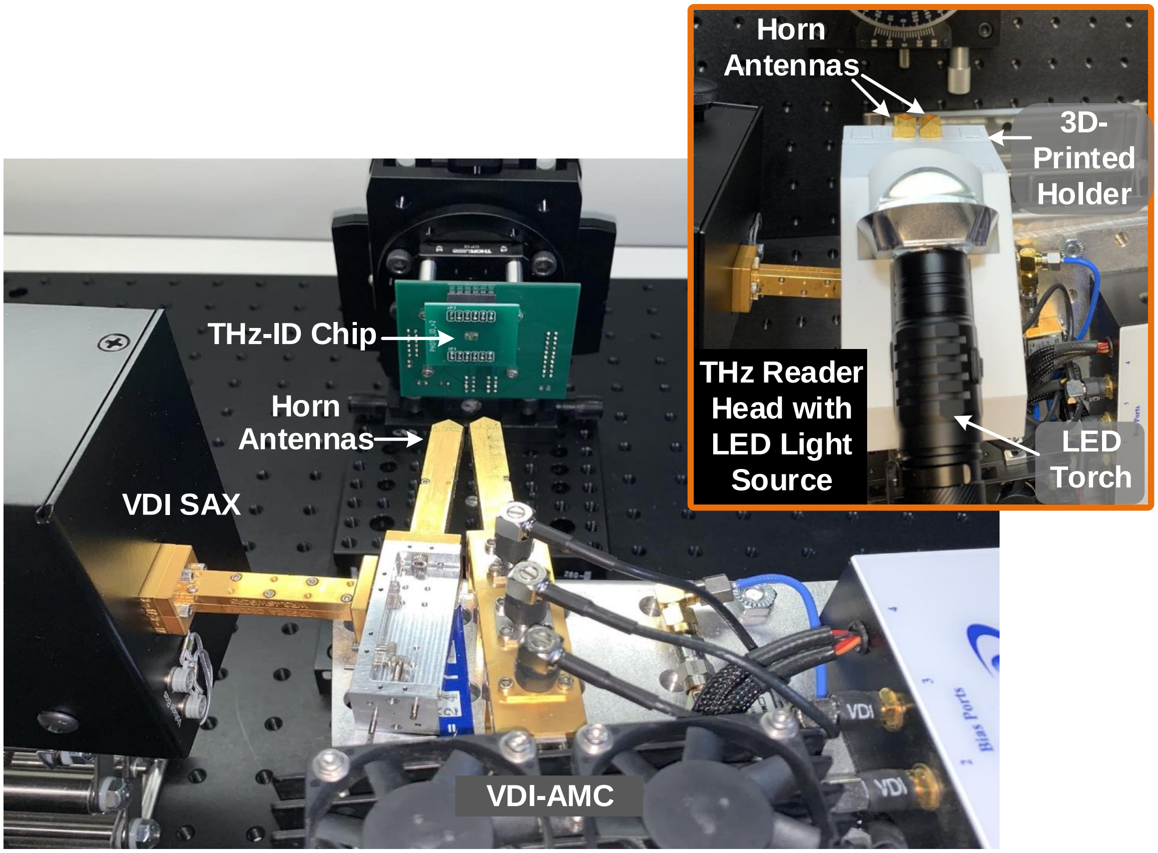

Figure 4-22: Photos of the testing up with and without a LED torch for photovoltaic powering of the CMOS chip. The power electronics inside the LED torch, which generates large switching noise, is by-passed in the setup.

4.5.2 Characterization of the Circuits

First, to characterize the 260-GHz backscatter module in a basic continuous-wave mode, the chip is externally powered and clocked (at f_{LO}=2 MHz) via the debugging pads. With the incident wave generated by the VDI AMC, a down-converted spectrum shown in Fig. 4-23 is obtained from the VDI SAX. The tone at 358 MHz is the expected signal backscattered by the THz-ID. It has a SNR of 36 dB at 1-kHz bandwidth, indicating the feasibility of an uplink with the designed 2-kbps data rate. The tone at 362 MHz is the upper-sideband image due to the limited image rejection ($\sim$10 dB) of the SSB mixer in the tag. The central tone at 360 MHz is the reader-generated 262.5-GHz signal directly reflected from the chip and its surroundings. Note that although this signal is already attenuated by $\sim$25 dB due to the cross-polarization of the reader antennas, it is still >30 dB higher than the tag-backscattered signal in

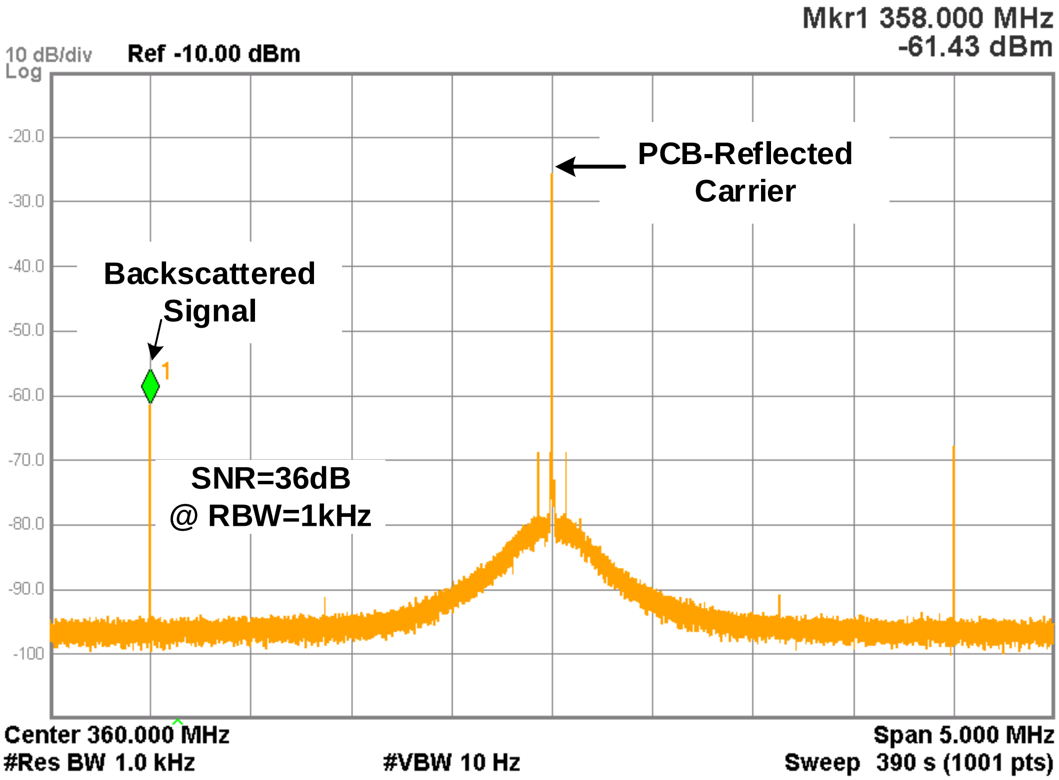

Figure 4-23: Measured spectrum of the backscattered signal

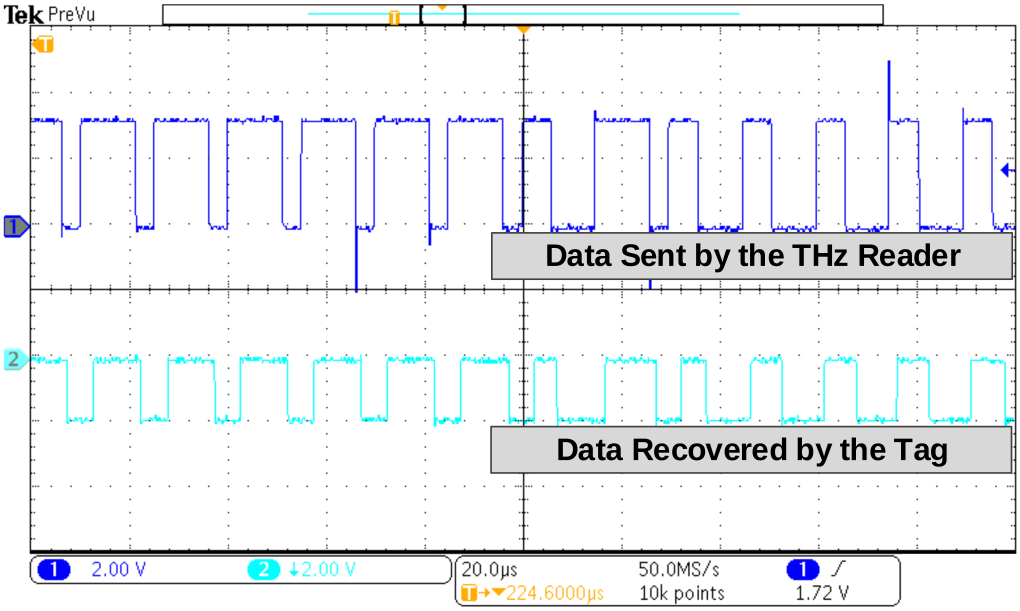

Figure 4-24: Measured downlink waveform from the tag.

Fig. 4-23. That in turn justifies our backscatter scheme using cross-polarization and frequency shifting. The scheme ensures that the phase noise of the directly-reflected signal is below the reader's thermal noise floor, hence does not degrade the uplink *SNR*. The scheme also avoids the saturation of the reader's baseband amplifier caused by the undesired reflected tone with large power.

Then, with OOK modulation to the VDI AMC, the tag downlink output is measured via a debugging pad. Pulse-width modulation is adopted for the encoding of the system, where duty cycle <45% represents bit 0 and >55% represents bit 1. In our measurement setup, the reader uses 40% duty cycle for bit 0 and 75% for bit 1. The results in Fig. 4-24 indicate that the tag downlink correctly recovers the original data created by the FPGA in the THz reader (Fig. 4-21). To achieve the gate bias of the downlink MOSFET detector, ambient lighting is found to be sufficient in the testing.

Next, we test the beam-steering capability of the THz-ID chip. Note that it is different from conventional beam-steering of phased arrays, due to the unique back-scattering operation of the chip, and the co-location of the reader's transmitter and receiver. Shown in Fig. 4-25a, the goal of the beam-steering of this tag is to ensure that when the chip does not face the reader perpendicularly, its backscattered wave can still be re-directed towards the reader. Figure 4-25a indicates that, with a chip tilting angle of θ and on-chip antenna spacing of $\lambda/2$, the following phase gradient (in degree) should be applied in order to compensate the total propagation-path difference related to the waves handled by the two patch antennas:

$$\varphi_A - \varphi_B = 2 \cdot (\frac{\lambda}{2} \sin\theta) \cdot \frac{360^\circ}{\lambda} = (\sin\theta) \cdot 360^\circ \tag{4.4}$$

This is verified in our experiment, where the LO phase of each THz SSB mixer is digitally controlled by the on-chip processor. Figure 4-25b shows the backscatter-wave power, which is received by the reader in the measurement, at varying chip tilting angle θ. Two tag phase-gradient settings requested by the reader, φ_A=φ_B and φ_A-φ_B=180°, are tested. The measured peak responses of the reader occur at θ=0° and θ=30°, respectively, which well agree with Eq. 4.4. This also shows that the maximum

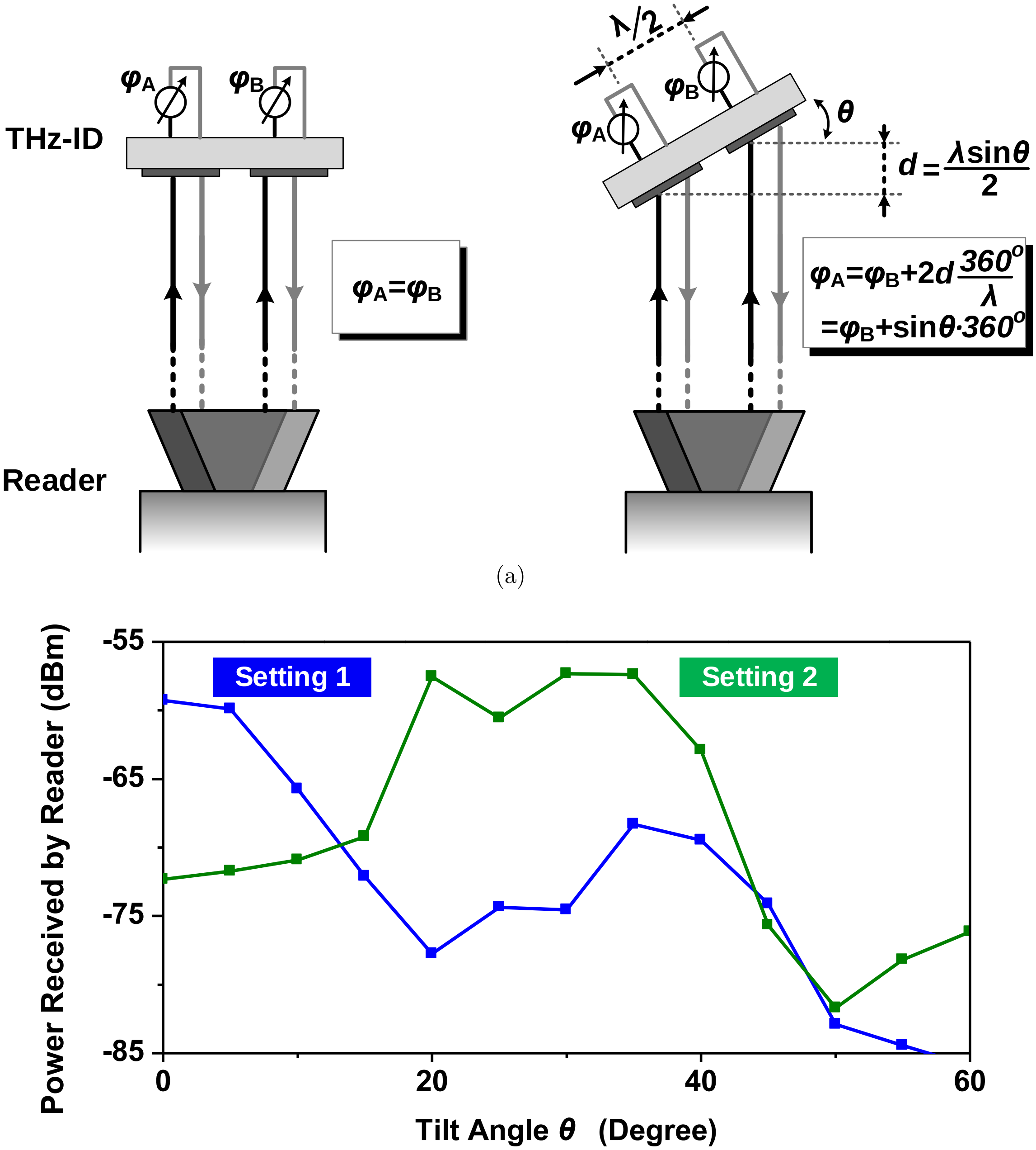

(a)

(b)

Figure 4-25: (a) Phase-shifting (φ_A-φ_B) conditions in the tag to ensure that the backscattered wave points to the reader when the tag is tilted by θ. (b) Measured backscattered-wave power, which is received by the reader, at different chip tilting angle θ. Here, two digital settings of φ_A-φ_B are applied.

beam-steering angle (in both azimuth and elevation directions) is ±30°. It should be noted here that, when an antenna is tilted, the effective aperture decreases by a factor of $\cos\theta$. At θ=30°, ∼1.2 dB two-way power loss should occur. However, in the measurements we received almost the same peak power in both settings. This can be attributed to either a better alignment in Setting 2 or measurement error.

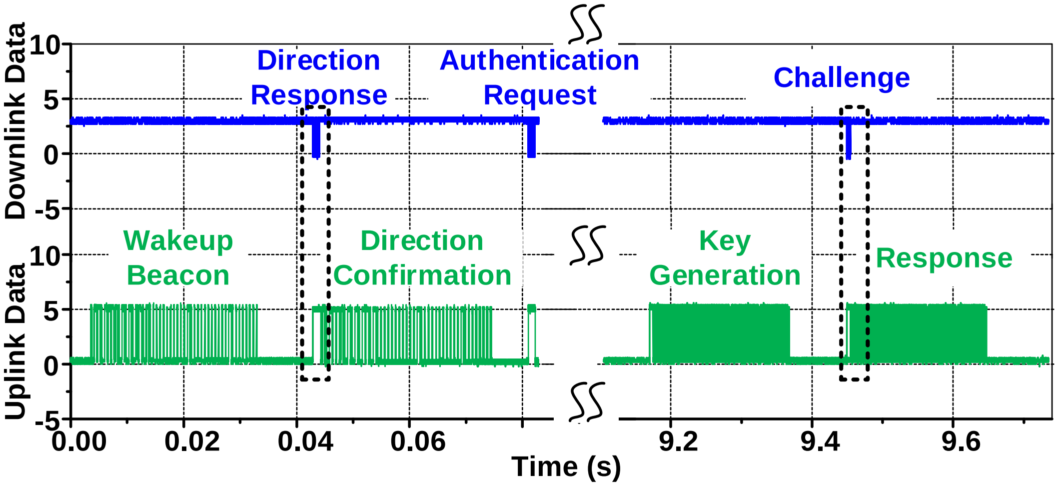

Figure 4-26: Measured downlink and uplink data in the protocol.

We also verified the protocol and the cryptographic function with an external power and the tag internal clock (Fig. 4-26). When the reader receives the tag's beacon message, the FPGA starts a feedback loop to request a change of uplink beam angle until the *SNR* is maximized. The measured waveforms associated with this operation are shown in Fig. 4-27. Then the reader sends a trigger to the chip to start the authentication process described in Section 4.3. Figure 4-28 shows the measured waveforms of the challenge-response protocol that the tag takes towards the end of the authentication process, in order to identify itself to the valid reader. In Fig. 4-27, when THz reader is transmitting data, the tag's downlink circuit recovers the exact same data and during the idle time random output pulses are observed, as explained in Section 4.2.3. Due to the preamble validation in the processor, those random pulses are rejected.

Lastly, with external LED illumination and photodiode powering, the chip is entirely power-autonomous and interrogated by the THz reader (see Fig. 4-29). It can be seen that, when the converter-startup is completed, the on-chip processor sends a

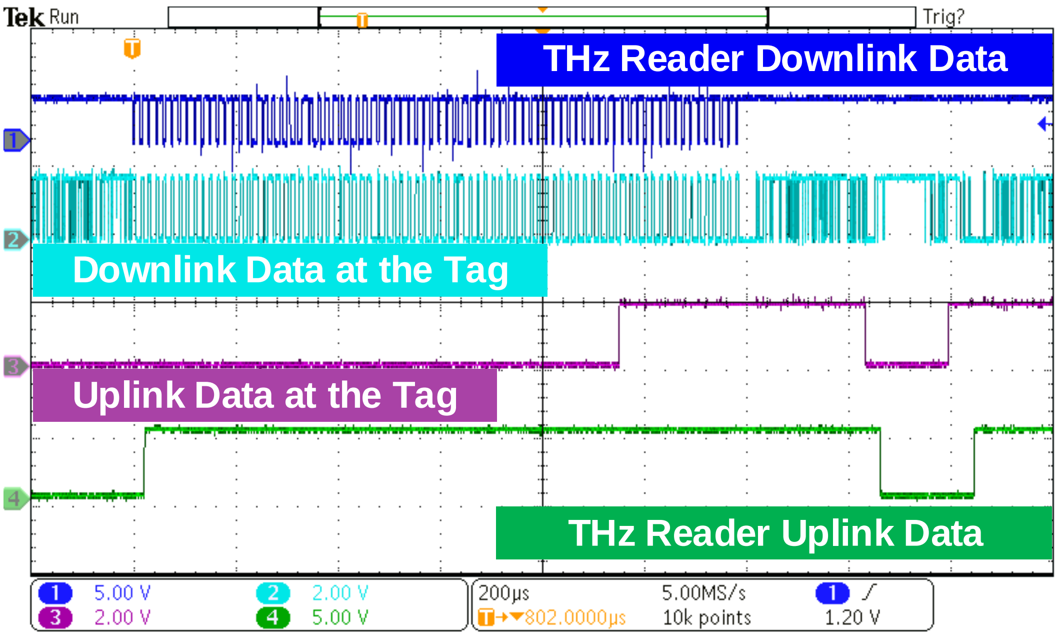

Figure 4-27: Zoom-in views of dotted regions representing the phases of direction response and confirmation.

tag-wakeup beacon signal through its 260-GHz backscatter uplink, and the signal is successfully received and recovered by our reader. Since the downlink amplifier consists of transistors operating in the subthreshold regime, the large photoelectric effect causes bias drift of the amplifier and excessive noise, which prevents the completion of the entire security protocol in the test. The static current of the processor also increases with the illumination. In the future development iterations, we should be able to optically power the complete protocol by enclosing the downlink and processor circuitry with a cover formed by the Al-pad layer and sidewalls formed by M1-to-Al stack.

The work presented in this chapter demonstrates a new application of THz CMOS electronics, which utilizes its advantages in compact size and packageless chip integration. We also show that silicon THz transceivers, which are long considered to be power hungry, can be applied in ultra-low-power systems, if a backscattering communication scheme is adopted. A comparison of our work with the prior state-of-the-art is given in Table 4.1. Our presented tag is built entirely on a low-cost CMOS chip, and is around 3× smaller than the smallest package-less, far-field chip reported previously [68]. It also offers multi-antenna beam-steering functionality for the first time in RFIDs. Com-

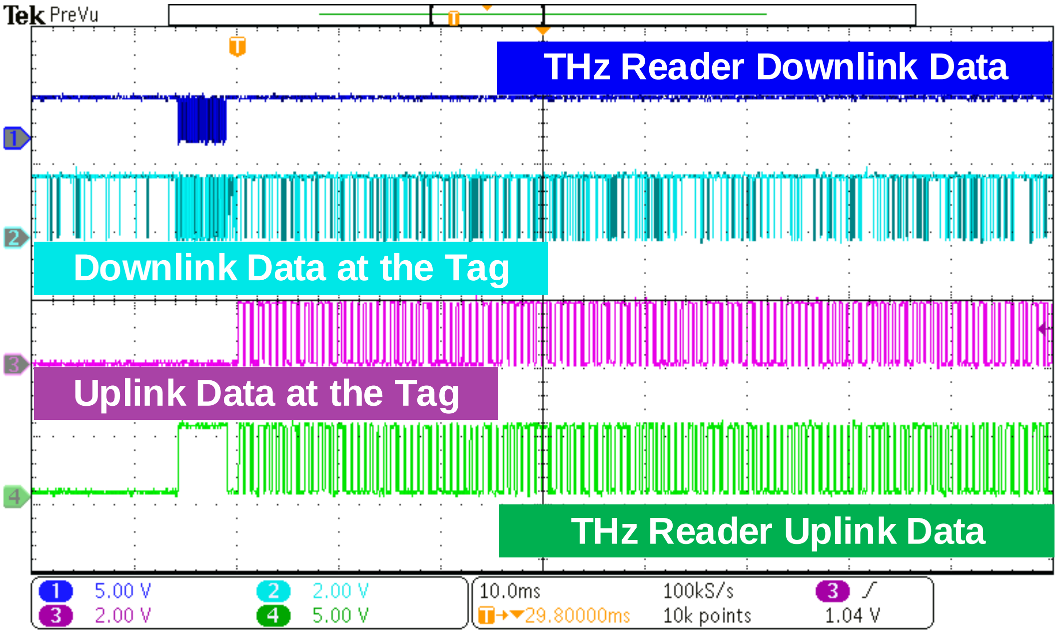

Figure 4-28: Zoom-in views of dotted regions representing the phases of challenge and response message.

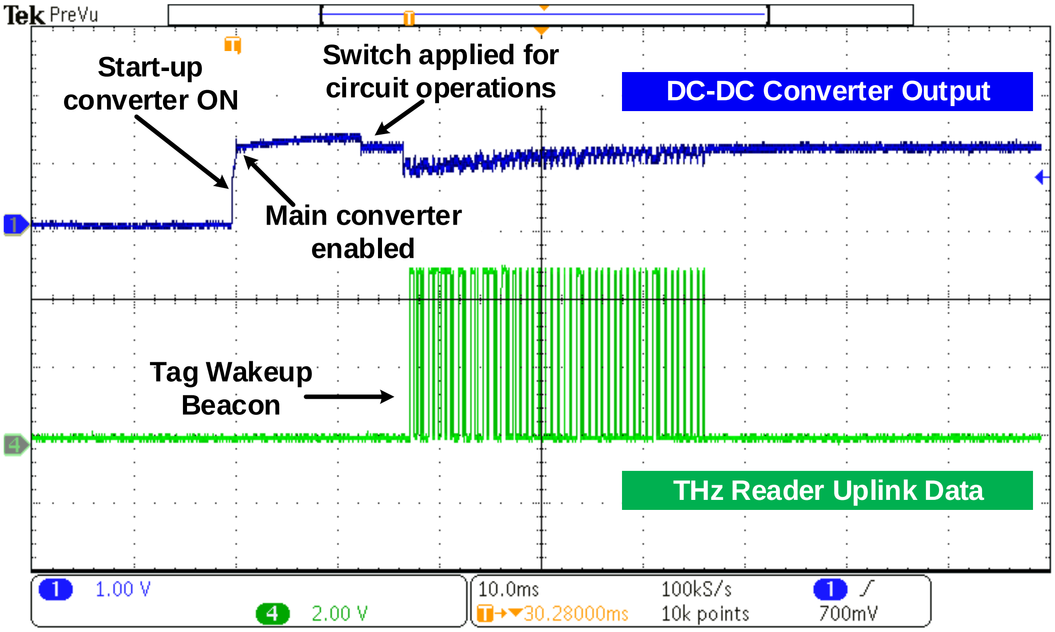

Figure 4-29: Measured startup behavior of THz-ID with optical powering.

pared to [69], the asymmetric public-key cryptography provides higher-level security, and makes the THz-ID tag suitable for privacy-sensitive applications.

Table 4.1: Summary of the THz-ID performance and comparison with other state-of-the-art RFIDs in CMOS

References	**CMOS Process**	**Carrier Freq. (GHz)**	**Modulation**	**Data Rate**	**Peak Power**	**Security**	**Range**	**Beam-Steering**	**Area (mm^2)**
This Work	65 nm	260	PWM 100% ASK	DL: 100 kbps UL: 2 kbps	21 μW	Yes (Elliptic Curve)	5 cm	Yes	1.6
[64]† ISSCC'17	180 nm	0.915	PPM	DL: 62.5 kbps UL: 30.3 kbps	2 mW	No	20 m	No	9†
[65] ISSCC'18	65 nm	5.8	DL: <4% ASK UL: HIMIL	DL: 5 Mbps UL: 4 kbps	10 μW	No	1 mm	No	0.01
[68] VLSI'14	65 nm	DL: 24 UL: 60	DL: 75% ASK UL: PPM	DL: 6.5 Mbps UL: 1.2 Mbps	11 mW‡	No	50 cm	No	4.4
[69]§ ISSCC'16	130 nm	0.433	DL:PPM UL:PWM	125 kbps	16 μW	Yes (Symmetric)	5 mm	No	64§

†Assembly of multiple functional layers (photo-voltaic powering, battery, antenna, etc.) is used.

‡The calculated value in [64] is cited.

§PCB-level components including off-chip coupler are required.

Chapter 5

Conclusion and Future Work

In this thesis, the first implementation of a chip-scale quantum magnetometer by integrating diamonds with CMOS technology is reported (Chapter 2). A novel architecture in which the essential components to detect NV-ODMR - a microwave generator, an inductor, an optical pump beam filter, and a photodetector - are fabricated throughout the CMOS multi-layers is created. The first prototype addressing NV spin ensembles in a single crystalline diamond slab is presented. The sensor demonstrates vector-field magnetic field measurements with a sensitivity of 32.1 $\mu T/\sqrt{Hz}$.

We also present in this thesis (Chapter 3) our second vector-field magnetometer, which is based on a scalable platform. We demonstrate room-temperature magnetic field sensing with a sensitivity of 245 $nT/Hz^{1/2}$, which is 130× better than our first prototype (Chapter 2). As described in Chapter 3, the enhancement is mainly due to: (i) the microwave launcher with uniform microwave generation that can be scaled up for large diamond area, (ii) an enhanced multi-layer nanophotonic filter for lower background noise, (iii) the extra rejection of the external laser fluctuation due to the differential measurement.

In Chapter 4 of this thesis, we demonstrate a package-less RFID working at sub-THz frequencies (THzID). This THzID is the smallest reported (1.6 mm^2) ID chip with far-field communication distance ($\sim$5 cm), using 260 GHz backscatter communications, enabled by a 2×2 on-chip patch antenna array. This configuration allows for beam-steering of the back-scattered beam for RF tags for the first time, allowing for extra functions such as interrogating many tags using one reader. The chip is equipped with an asymmetric public-key cryptography processor that provides higher-level security, and makes the THzID tag suitable for privacy-sensitive applications. The THzID consumes a peak power of 21 µW generated by a built-in photovoltaic array placed under the antennas.

In this chapter, future research directions inspired by the work presented in this thesis are discussed. In section 5.1, techniques to push the hybrid CMOS-Diamond magnetometer to unprecedented performance for CMOS integrated magnetometers are presented. Ideas to enable a fully practical solution for authentication using ultra-small, low-cost THz-ID tags are proposed in Section 5.2. The ongoing effort to realize a cryogenic-CMOS controller for diamond color centers is discussed in Section 5.3. Finally, exciting research directions that utilize the advantages of wireless communication and quantum systems to realize a scalable multi-qubit cryogenic CMOS quantum processor are summarized.

5.1 The Future of Hybrid CMOS-Diamond Sensors

The hybrid CMOS-Diamond magnetometer prototypes presented in this thesis provide a clear pathway to further push the sensitivity of the proposed sensor to sub-nT/Hz$^{1/2}$. As shown in Fig. 5-1, the estimated sensitivity with varying optical filtering performance, sensing areas and NV-centers densities (see Appendix A for more details). We predict that if the NV density reaches 1 ppm [80] with a sensing area of 1 mm^2, the sensitivity can reach ∼600 pT/Hz$^{1/2}$. Towards achieving a compact highly-sensitive CMOS quantum magnetometer, the green light pump can be integrated into the system using a chip-scale laser diode [81], a green vertical-cavity surface-emitting laser (VCSEL) [82], or CMOS-compatible waveguided delivery of the optical pump beam [83].

Further improvements can be done on the component level. Even though we managed to improve the filtering by ∼ two orders of magnitude, further enhancement is still required. Fabricating a resonant grating [84] in diamond can additionally attenuate

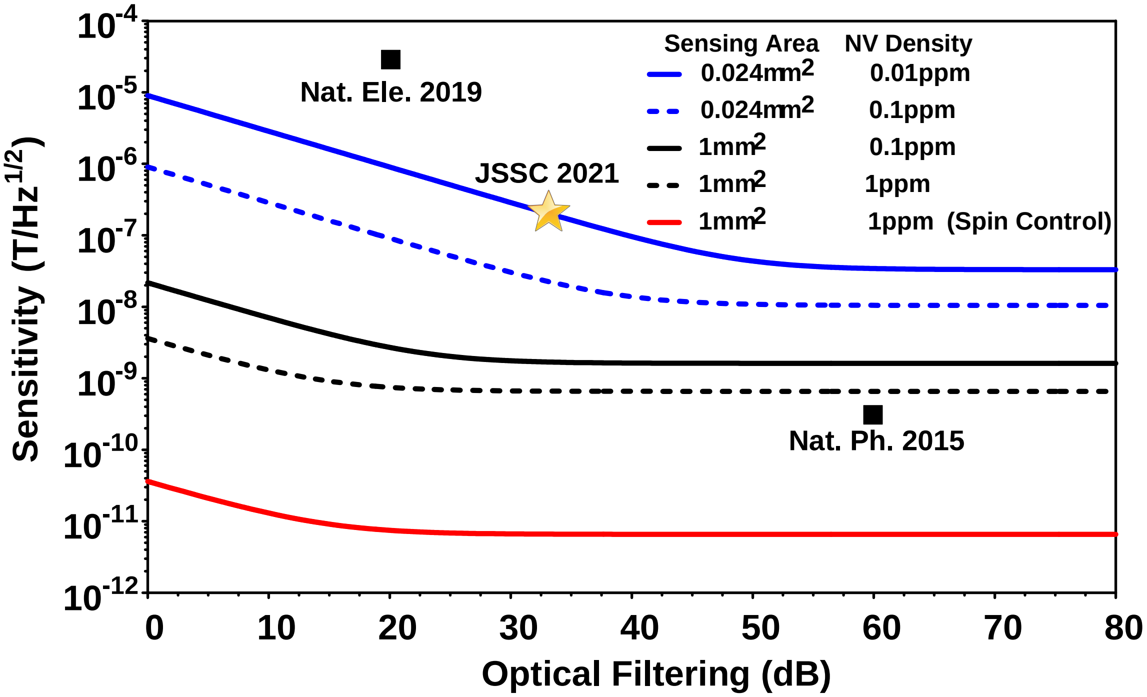

Figure 5-1: Estimation of sensitivity for hybrid CMOS-NV magnetometers with different configurations.

the green laser. On-chip detection circuitry allows for techniques such as time gating can be also utilized to separate the green excitation from the red fluorescence in time [85]. Using a diamond waveguide geometry [19] can enhance both the signal and the filtering (noise reduction), hence, the *SNR*.

The microwave array can be also optimized for a more uniform field. For instance, better optimized configuration of the boundary wire arrays (i.e. Group D in Fig. 3-6b) used in the microwave launcher can lead to high magnetic homogeneity over a larger proportion of the total launcher area. For example, we find that if each Group D consists of m=4 wires (d=4 µm) with I_D=6.35 mA, and a gap of 12 µm exists between Group D and Group A/C, 95% magnetic homogeneity is achieved for the entire -60 to 60-µm space above Group A-B-C. Homogeneity over large space also promises a significant sensitivity enhancement via spin-controlled pulse sequence [36]. It is worth mentioning that we have conducted pulse-based spin control experiments (e.g. Rabi oscillations [86]) on the whole NV ensemble using the magnetic field generated by the chip and off-chip optical detection. The measured Rabi oscillation, shown in Fig. 5-2,

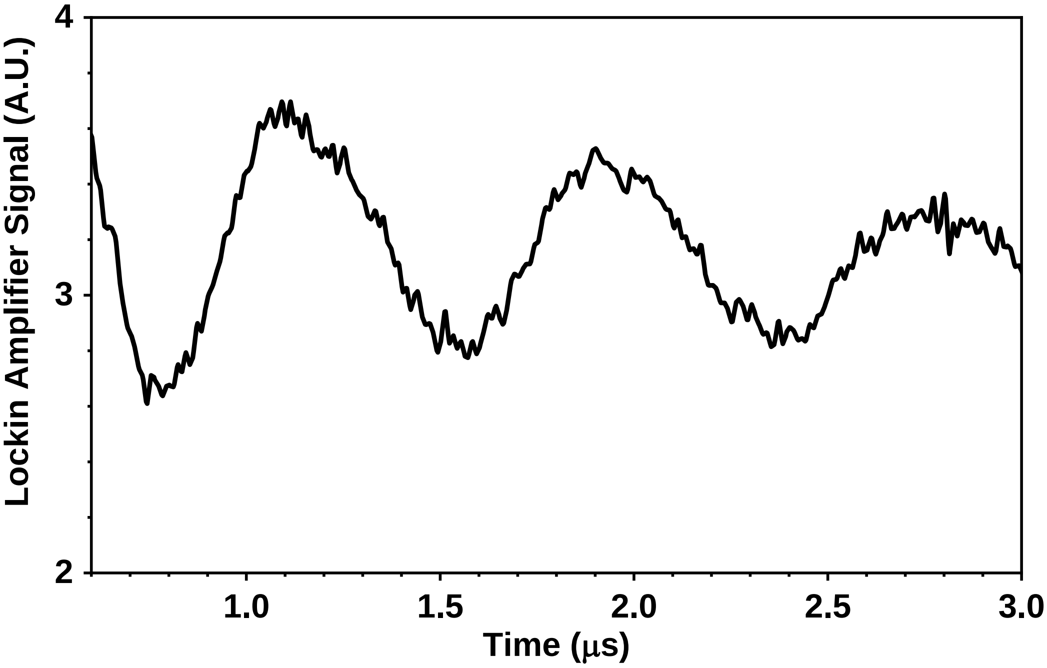

Figure 5-2: Measured Rabi oscillations of an ensemble of NV centers using the uniform microwave field generated by the chip.

confirms that all the NV centers in the ensemble exhibit the same Rabi frequency (∼1.2 MHz) determined by the local microwave field and that the NVs are flipped at the same rate and their spin-dependent fluorescence signals add coherently.

The ability to manipulate the NV centers over a larger area and pushing the performance to the best sensitivity regime enable the integration of larger numbers of detectors for gradient magnetometry, multiplexed analytical nuclear-magnetic resonance (NMR) spectroscopy [87], atomic gyroscopes [88], and other quantum-sensing applications [35]. Two examples are listed below:

1. Multiplexed sensing (see Fig. 5-3) that can be achieved using many pixels of the sensor. Therefore, parallel readout of an entire magnetic field spectrum (magnetic spectrometer) can be made possible. Each pixel scans a specific frequency range similar to comb spectrometers, allowing for advanced current sensing to detect cable faults in industrial settings, among other applications.

2. Gradient magnetometry and imaging capabilities (see Fig. 5-4) that can be

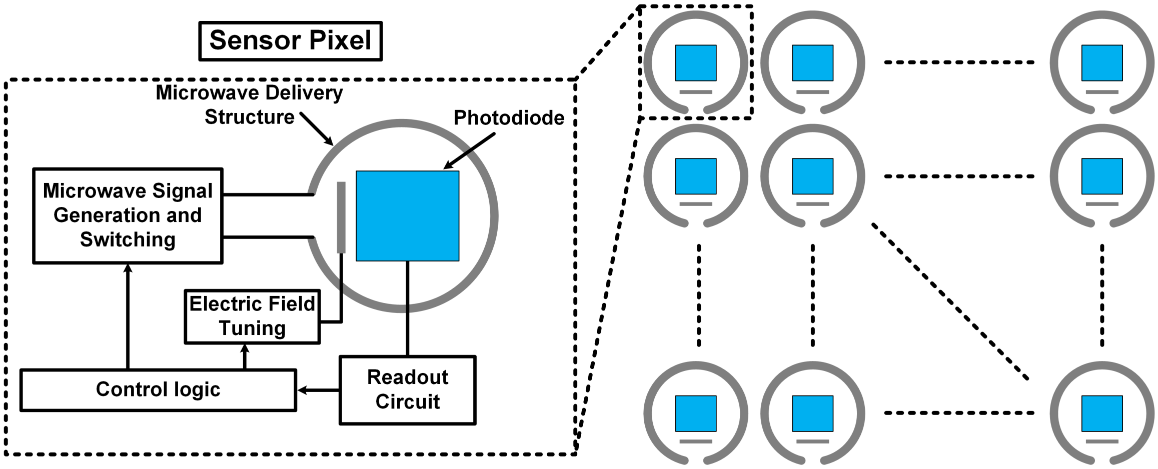

Figure 5-3: NV-based multiplexed sensing architecture with an array of sensors.

realized by integrating an array of photodiodes, forming a camera. This allows for applications including navigation in a GPS denied environment and thermal and magnetic field imaging with micrometer scale resolution.

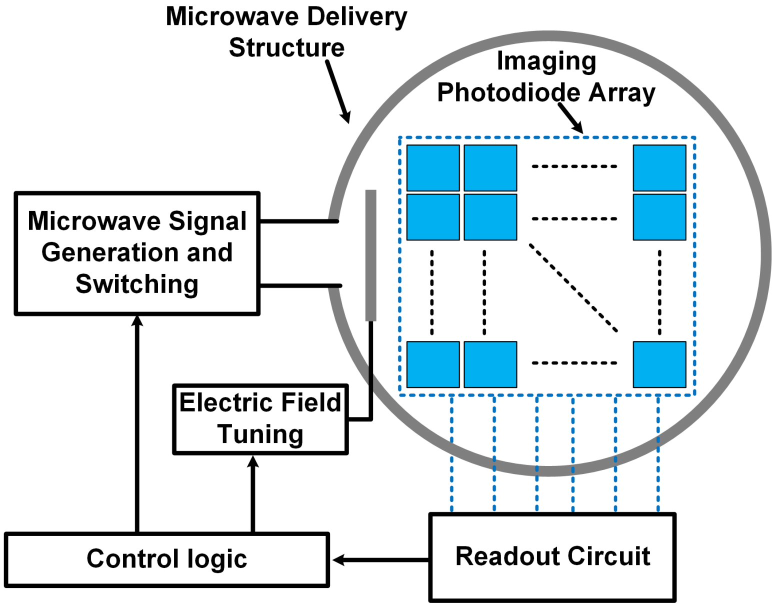

Figure 5-4: NV-based magnetic imager with an array of photodiodes below a single microwave delivery structure.

5.2 The Future of THzID

The work presented in Chapter 4 demonstrates the feasibility of security ID tags with ultra-small size and cost, which is expected to empower a wide range of new applications in manufacturing, logistics, anti-counterfeiting, among others. To fully make these applications practical, a few more technologies should be developed. For example, to allow for embedding of the tag inside opaque materials, energy harvesting directly from the THz wave is desired. That requires high-speed rectifier devices in the CMOS process. To this end, the poly-gate-separate Schottky diodes in CMOS, which have ∼2-THz cutoff frequency and are used in THz imaging [89], could possibly meet the above needs. Secondly, although the size and cost requirements for the THz-ID reader, compared to the tags, are much more relaxed, it is still highly preferred that the reader front-end is implemented using silicon integrated circuits. Rapid advances are being made in this area. For example, in [90], the 200-to-255-GHz power amplifier using 130-nm SiGe BiCMOS process (f_{max}≈500 GHz) is already capable of generating 20 mW of power, which is only 7 dB away from the VDI AMC used in our tag reader. In light of recent developments of high-speed and high-power SiGe and CMOS processes [91–94] with up to 720-GHz f_{max} and up to 7.1-V breakdown voltage, achieving radiation power of 100 mW in the sub-THz regime is no longer unimaginable. All of these advances can promise longer distance communication that can enable applications such as controlling micro drones, where size, cost, beam-steering and low-power are important. Other IoT applications can follow especially with the advances in 6G communication and beyond.

5.3 Cryogenic CMOS Scalable Quantum Processors

The research done in this thesis opened the door for exciting research directions that utilize the advantages of wireless communication and quantum systems, enabling new paradigms in sensing, computing, and biomedical applications. Next, the ongoing efforts to realize a scalable multi-qubit cryogenic CMOS quantum processor are

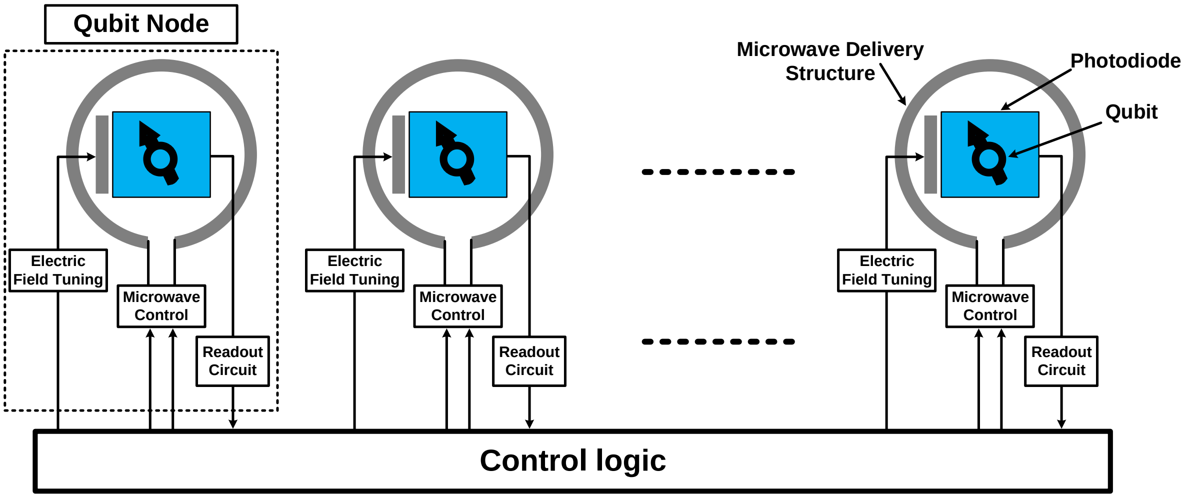

Figure 5-5: NV-based individual Qubit control for scalable quantum information processing applications.

summarized. Driven by the hybrid CMOS-Diamond quantum sensing work (Chapter 2, and Chapter 3), we are currently working on a cryogenic multi-qubit processor for quantum information processing [95–97]. We develop a CMOS-compatible architecture to control the spins and the optical transitions of individual color center qubits (see the conceptual schematic in Fig. 5-5). These color centers (e.g., NV centers in diamond) are integrated into diamond waveguides attached to the top of the CMOS chip (see Fig. 5-6), where each waveguide contains a single qubit. The high integration density of CMOS technologies enables a closely spaced array of inductors; each addresses one qubit. The microwave signal to the inductors is fed from outside through on-chip current drivers. To achieve the microwave control of a large number of individual qubits simultaneously with a reduced number of control signals to the cryostat, we use an integrated digital serial-parallel interface (SPI). To tune the optical transitions of the color centers, we rely on strain tuning using on-chip electrodes. On-chip controller is used to control the individual strain tuning electrodes. This is enabled by the ability to integrate passive and active circuits as well as the low leakage at cryogenic temperatures of the CMOS technologies. This system is the first step towards a more complex scalable solid-state quantum processor.

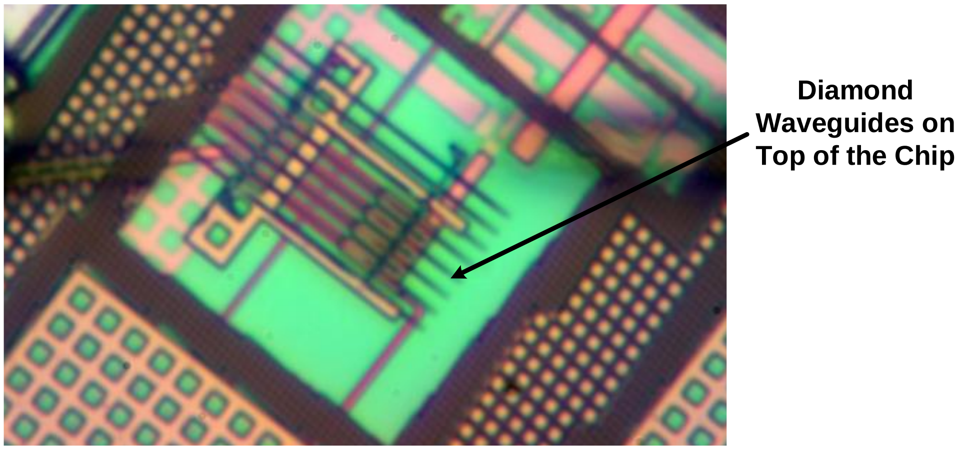

Figure 5-6: Micrograph of the diamond waveguides attached to the cryo-CMOS controller.

On the other hand, enabled by the low-power operation of the THzID (Chapter 4), we are currently exploring utilizing THz wireless systems to push quantum applications forward. Specifically, we are working towards realizing low-power cryogenic THz wireless links that efficiently deliver control signals of quantum systems to the cryostat. Interfacing with the cryostat using conductive links results in a significant heat transfer loss. For example, in our experiments, a coaxial-cable results in $\sim$ 4 mW of heat transfer. It is worth mentioning that the available power budget in a conventional cryostat is $\sim$10-100 mW, and a conventional connection would require tens of cables. This heat loss limits the scalability and practical realizations of quantum systems. Using a low-power cryo-CMOS wireless link that can replace the expensive and lossy physical conductive links promises to be a solution to this problem. Compared to optical links, THz links can also support high data-rates with enhanced noise performance due to the reduced quantum noise, which is a primary contributor to the noise floor at cryogenic temperatures. A cryogenic CMOS receiver can detect multi-Gb/s control signals modulated on a THz carrier (e.g., 300-GHz). Moreover, a full THz transceiver can utilize the backscattering approach presented in Chapter 4 for low-power operation. The readout signals of the qubits can be combined and backscattered using a THz mixer.

The architecture shown in Fig. 5-7 could possibly enable a quantum processor with a larger number of color center qubits. This architecture is composed of two subsystems: (i) The hybrid CMOS-Diamond multi-qubit controller, (ii) THz link, using antennas or dielectric waveguides, communicates between the cryogenic controller and the room-temperature controller. The proposed architecture allows for optimized power budget inside the cryostat, while allowing the flexibility to improve the performance of the circuits integrated inside the cryostat. Towards a full implementation of a scalable quantum processor using color centers, CMOS single-photon avalanche photodiodes (APD) enables on-chip readout circuitry. Moreover, integration with photonic chips is also needed to create the entanglement of the qubits. This allows for closed-loop feedback between the spin states' control and readout using tightly integrated logic on CMOS. This architecture can be extended to other qubits such as superconducting and spin qubits.

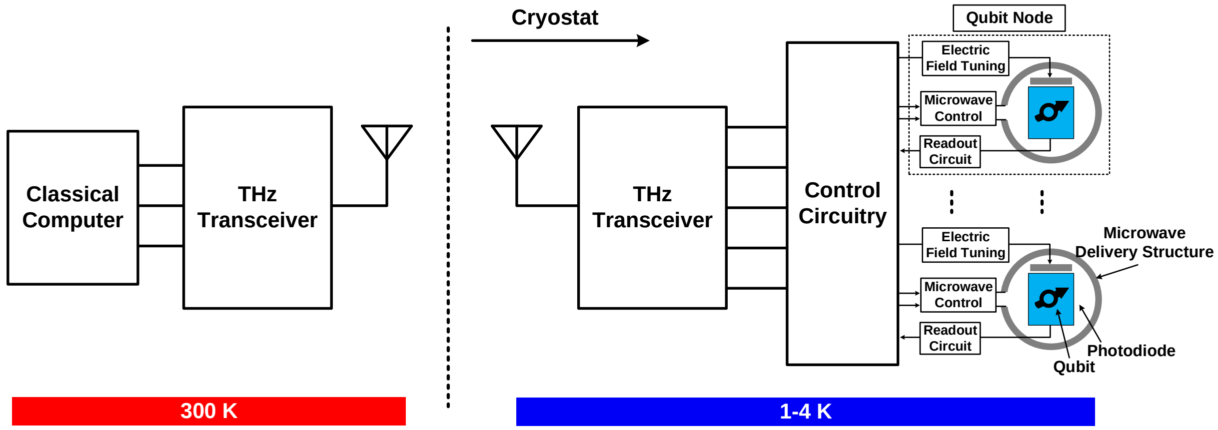

Figure 5-7: Proposed cryogenic hybrid CMOS-Diamond scalable quantum processor architecture.

Appendix A

Estimation of Sensitivity for Future Hybrid CMOS-NV Magnetometers

The sensor sensitivity is inversely proportional to the SNR of the sensor output:

$$S \propto \frac{1}{SNR} = \frac{\sigma_i \cdot \Delta\nu}{\gamma_e \cdot I_r}, \tag{A.1}$$

where σ_i is the total noise current density (unit: A/Hz$^{1/2}$), $\Delta\nu$ is the linewidth of the ODMR curve, I_r is the photo-current due to the red fluorescence signal, and γ_e is 28 GHz/T. From our experiments, the linewidth of the ODMR is 6 MHz. The noise is limited by the shot noise of either the green excitation (for low optical filtering ratio) or the red fluorescence (for high optical filtering ratio):

$$\sigma_i = \sqrt{2 \cdot q \cdot (I_g + I_r)}, \tag{A.2}$$

where q is the electronic charge, and I_g and I_r are the photo-currents due to the unfiltered green light and red fluorescence, respectively. The value of I_g is estimated as:

$$I_g = P_g \cdot R_{PD} \cdot \eta_g, \tag{A.3}$$

where P_g is the input optical power, R_{PD} is the photodiode responsivity, and η_g is the green rejection of the optical filter. The value of I_r is proportional to the total number

n_{nv} of NV centers in the diamond, which is proportional to the sensing area A_{nv} and NV density ρ_{nv}. Lastly, the performance using the spin-controlled pulse sequence is estimated based on the fact that the equivalent transition linewidth (hence the zero-crossing slope m) of the configuration is reduced by ~100× for AC magnetic field measurements [13], [36].

Bibliography

[1] Ken B Cooper, Robert J Dengler, Nuria Llombart, Bertrand Thomas, Goutam Chattopadhyay, and Peter H Siegel. THz Imaging Radar for Standoff Personnel Screening. *IEEE Transactions on Terahertz Science and Technology*, 1(1):169–182, 2011. ISSN 2156342X. doi: 10.1109/TTHZ.2011.2159556.

[2] Zachary D. Taylor, Rahul S. Singh, David B. Bennett, Priyamvada Tewari, Colin P. Kealey, Neha Bajwa, Martin O. Culjat, Alexander Stojadinovic, Hua Lee, Jean Pierre Hubschman, Elliott R. Brown, and Warren S. Grundfest. THz medical imaging: In vivo hydration sensing. *IEEE Transactions on Terahertz Science and Technology*, 1(1):201–219, 2011. ISSN 2156342X. doi: 10.1109/TTHZ.2011.2159551.

[3] Tadao Nagatsuma. Terahertz communications: past, present and future. In *2015 40th International Conference on Infrared, Millimeter, and Terahertz waves (IRMMW-THz)*, pages 1–2, 2015.

[4] Cheng Wang, Xiang Yi, James Mawdsley, Mina Kim, Zihan Wang, and Ruonan Han. An On-Chip Fully-Electronic Molecular Clock Based on sub-THz Rotational Spectroscopy. *Nature Electronics*, 1(7):421–427, 2018.

[5] Edoardo Charbon, Fabio Sebastiano, Masoud Babaie, Andrei Vladimirescu, Mina Shahmohammadi, Robert Bogdan Staszewski, Harald A.R. Homulle, Bishnu Patra, Jeroen P.G. van Dijk, Rosario M. Incandela, Lin Song, and Bahador Valizadehpasha. Cryo-CMOS Circuits and Systems for Scalable Quantum Computing. In *IEEE International Solid-State Circuits Conference*, pages 264–265, San Francisco, CA, 2017. ISBN 9781509037582. doi: 10.1109/ISSCC.2017.7870359.

[6] Joseph C Bardin, Evan Jeffrey, Erik Lucero, Trent Huang, Ofer Naaman, Rami Barends, Ted White, Marissa Giustina, Daniel Sank, Pedram Roushan, Kunal Arya, Benjamin Chiaro, Julian Kelly, Jimmy Chen, Brian Burkett, Yu Chen, Andrew Dunsworth, Austin Fowler, Brooks Foxen, Craig Gidney, Rob Graff, Paul Klimov, Josh Mutus, Matthew Mcewen, Anthony Megrant, Matthew Neeley, Charles Neill, Chris Quintana, Amit Vainsencher, Hartmut Neven, and John Martinis. A 28nm Bulk-CMOS 4-to-8GHz <2mW Cryogenic Pulse Modulator for Scalable Quantum Computing. In *IEEE International Solid-State Circuits Conference*, pages 456–457, San Francisco, CA, 2019. ISBN 9781538685310.

[7] Georg Kucsko, PC Maurer, Norman Ying Yao, Michael Kubo, HJ Noh, PK Lo, Hongkun Park, and Mikhail D Lukin. Nanometre-scale thermometry in a living cell. *Nature*, 500(7460):54, 2013.

[8] Florian Dolde, Helmut Fedder, Marcus W Doherty, Tobias Nöbauer, Florian Rempp, Gopalakrishnan Balasubramanian, Thomas Wolf, Friedemann Reinhard, Lloyd CL Hollenberg, Fedor Jelezko, et al. Electric-field sensing using single diamond spins. *Nature Physics*, 7(6):459, 2011.

[9] JR Maze, PL Stanwix, JS Hodges, S Hong, JM Taylor, P Cappellaro, L Jiang, MV Gurudev Dutt, E Togan, AS Zibrov, et al. Nanoscale magnetic sensing with an individual electronic spin in diamond. *Nature*, 455(7213):644, 2008.

[10] Gopalakrishnan Balasubramanian, IY Chan, Roman Kolesov, Mohannad Al-Hmoud, Julia Tisler, Chang Shin, Changdong Kim, Aleksander Wojcik, Philip R Hemmer, Anke Krueger, et al. Nanoscale imaging magnetometry with diamond spins under ambient conditions. *Nature*, 455(7213):648, 2008.

[11] D. Le Sage, K. Arai, D. R. Glenn, S. J. Devience, L. M. Pham, L. Rahn-Lee, M. D. Lukin, A. Yacoby, A. Komeili, and R. L. Walsworth. Optical Magnetic Imaging of Living Cells. *Nature*, 496(7446):486–489, 2013. ISSN 00280836. doi: 10.1038/nature12072.

[12] A. Gruber, A. Drabenstedt, C. Tietz, L. Fleury, J. Wrachtrup, and C. Von Borczyskowski. Scanning Confocal Optical Microscopy and Magnetic Resonance on Single Defect Centers. *Science*, 276:2012–2014, 1997.

[13] J. M. Taylor, P. Cappellaro, L. Childress, L. Jiang, D. Budker, P. R. Hemmer, A. Yacoby, R. Walsworth, and M. D. Lukin. High-Sensitivity Diamond Magnetometer with Nanoscale Resolution. *Nature Physics*, 4(10):810–816, 2008. ISSN 17452481. doi: 10.1038/nphys1075.

[14] S. Steinert, F. Ziem, L. T. Hall, A. Zappe, M. Schweikert, N. Götz, A. Aird, G. Balasubramanian, L. Hollenberg, and J. Wrachtrup. Magnetic Spin Imaging under Ambient Conditions with Sub-Cellular Resolution. *Nature Communications*, 4, 2013. ISSN 20411723. doi: 10.1038/ncomms2588.

[15] Dominik B. Bucher, David R. Glenn, Hongkun Park, Mikhail D. Lukin, and Ronald L. Walsworth. Hyperpolarization-enhanced nmr spectroscopy with femtomole sensitivity using quantum defects in diamond, 2018.

[16] Gopalakrishnan Balasubramanian, Philipp Neumann, Daniel Twitchen, Matthew Markham, Roman Kolesov, Norikazu Mizuochi, Junichi Isoya, Jocelyn Achard, Johannes Beck, Julia Tissler, et al. Ultralong spin coherence time in isotopically engineered diamond. *Nature materials*, 8(5):383, 2009.

[17] Yechezkel Schlussel, Till Lenz, Dominik Rohner, Yaniv Bar-Haim, Lykourgos Bougas, David Groswasser, Michael Kieschnick, Evgeny Rozenberg, Lucas Thiel,

Amir Waxman, Jan Meijer, Patrick Maletinsky, Dmitry Budker, and Ron Folman. Wide-field imaging of superconductor vortices with electron spins in diamond. *Phys. Rev. Applied*, 10:034032, Sep 2018. doi: 10.1103/PhysRevApplied.10.034032. URL `https://link.aps.org/doi/10.1103/PhysRevApplied.10.034032`.

[18] Thomas Wolf, Philipp Neumann, Kazuo Nakamura, Hitoshi Sumiya, Takeshi Ohshima, Junichi Isoya, and Jörg Wrachtrup. Subpicotesla diamond magnetometry. *Physical Review X*, 5(4):041001, 2015.

[19] Hannah Clevenson, Matthew E Trusheim, Carson Teale, Tim Schröder, Danielle Braje, and Dirk Englund. Broadband magnetometry and temperature sensing with a light-trapping diamond waveguide. *Nature Physics*, 11(5):393, 2015.

[20] Georgios Chatzidrosos, Arne Wickenbrock, Lykourgos Bougas, Nathan Leefer, Teng Wu, Kasper Jensen, Yannick Dumeige, and Dmitry Budker. Miniature cavity-enhanced diamond magnetometer. *Physical Review Applied*, 8(4):044019, 2017.

[21] Martijn F. Snoeij, Viola Schaffer, Sudarshan Udayashankar, and Mikhail V. Ivanov. Integrated fluxgate magnetometer for use in isolated current sensing. *IEEE Journal of Solid-State Circuits*, 51(7):1684–1694, 2016. doi: 10.1109/JSSC.2016.2554147.

[22] Mahdi Kashmiri, Wilko Kindt, Frerik Witte, Robin Kearey, and Daniel Carbonell. 27.9 a 200ks/s 13.5b integrated-fluxgate differential-magnetic-to-digital converter with an oversampling compensation loop for contactless current sensing. In *2015 IEEE International Solid-State Circuits Conference - (ISSCC) Digest of Technical Papers*, pages 1–3, 2015. doi: 10.1109/ISSCC.2015.7063140.

[23] Drew A. Hall, Richard S. Gaster, Kofi A. A. Makinwa, Shan X. Wang, and Boris Murmann. A 256 pixel magnetoresistive biosensor microarray in 0.18 µm cmos. *IEEE Journal of Solid-State Circuits*, 48(5):1290–1301, 2013. doi: 10.1109/JSSC.2013.2245058.

[24] Tiago Costa, Filipe A. Cardoso, José Germano, Paulo P. Freitas, and Moisés S. Piedade. A cmos front-end with integrated magnetoresistive sensors for biomolecular recognition detection applications. *IEEE Transactions on Biomedical Circuits and Systems*, 11(5):988–1000, 2017. doi: 10.1109/TBCAS.2017.2743685.

[25] J.C. van der Meer, F.R. Riedijk, E. van Kampen, K.A.A. Makinwa, and J.H. Huijsing. A fully integrated cmos hall sensor with a 3.65 /spl mu/t 3/spl sigma/ offset for compass applications. In *ISSCC. 2005 IEEE International Digest of Technical Papers. Solid-State Circuits Conference, 2005.*, pages 246–247 Vol. 1, 2005. doi: 10.1109/ISSCC.2005.1493961.

[26] Paul Peng Liu, Karl Skucha, Yida Duan, Mischa Megens, Jungkyu Kim, Igor I. Izyumin, Simone Gambini, and Bernhard Boser. Magnetic relaxation detector for

microbead labels. *IEEE Journal of Solid-State Circuits*, 47(4):1056–1064, 2012. doi: 10.1109/JSSC.2012.2185339.

[27] Simone Gambini, Karl Skucha, Paul Peng Liu, Jungkyu Kim, and Reut Krigel. A 10 kpixel cmos hall sensor array with baseline suppression and parallel readout for immunoassays. *IEEE Journal of Solid-State Circuits*, 48(1):302–317, 2013. doi: 10.1109/JSSC.2012.2224531.

[28] R. L. Fagaly. Superconducting quantum interference device instruments and applications. *Review of Scientific Instruments*, 77(10):101101, 2006. doi: 10.1063/1.2354545. URL `https://doi.org/10.1063/1.2354545`.

[29] M I Faley, U Poppe, K Urban, D N Paulson, and R L Fagaly. A new generation of the HTS multilayer DC-SQUID magnetometers and gradiometers. *Journal of Physics: Conference Series*, 43:1199–1202, jun 2006. doi: 10.1088/1742-6596/43/1/292. URL `https://doi.org/10.1088/1742-6596/43/1/292`.

[30] K.E. Leslie, R.A. Binks, C.J. Lewis, M.D. Scott, D.L. Tilbrook, and J. Du. Three component spinner magnetometer featuring rapid measurement times. *IEEE Transactions on Applied Superconductivity*, 11(1):252–255, 2001. doi: 10.1109/77.919331.

[31] Kasper Jensen, Rima Budvytyte, Rodrigo A Thomas, Tian Wang, Annette M Fuchs, Mikhail V Balabas, Georgios Vasilakis, Lars D Mosgaard, Hans C Stærkind, Jörg H Müller, et al. Non-invasive detection of animal nerve impulses with an atomic magnetometer operating near quantum limited sensitivity. *Scientific reports*, 6(1):1–7, 2016.

[32] Vishal Shah, Svenja Knappe, Peter DD Schwindt, and John Kitching. Subpicotesla atomic magnetometry with a microfabricated vapour cell. *Nature Photonics*, 1 (11):649–652, 2007.

[33] Dong Sheng, Abigail R Perry, Sean P Krzyzewski, Shawn Geller, John Kitching, and Svenja Knappe. A microfabricated optically-pumped magnetic gradiometer. *Applied physics letters*, 110(3):031106, 2017.

[34] Behzad Razavi. *RF microelectronics*. Prentice Hall Press, USA, 2nd edition, 2011. ISBN 0137134738.

[35] Christian L Degen, F Reinhard, and P Cappellaro. Quantum sensing. *Reviews of modern physics*, 89(3):035002, 2017.

[36] John F Barry, Jennifer M Schloss, Erik Bauch, Matthew J Turner, Connor A Hart, Linh M Pham, and Ronald L Walsworth. Sensitivity optimization for nv-diamond magnetometry. *arXiv preprint arXiv:1903.08176*, 2019.

[37] *High Frequency Structure Simulator (HFSS) User Guide*. ANSYS Inc. URL `http://www.ansys.com/`.

[38] Mohamed I Ibrahim, Christopher Foy, Donggyu Kim, Dirk R Englund, and Ruonan Han. Room-Temperature Quantum Sensing in CMOS : On-Chip Detection of Electronic Spin States in Diamond Color Centers for Magnetometry. In *Symposia on VLSI Technology and Circuits*, Honolulu, HI, 2018. ISBN 9781538642146.

[39] Donggyu Kim, Mohamed I. Ibrahim, Christopher Foy, Matthew E. Trusheim, Ruonan Han, and Dirk R. Englund. A CMOS-Integrated Quantum Sensor Based on Nitrogen-Vacancy Centres. *Nature Electronics*, 2, 2019.

[40] Anatoly V Zayats, Igor I Smolyaninov, and Alexei A Maradudin. Nano-optics of surface plasmon polaritons. *Physics reports*, 408(3-4):131–314, 2005.

[41] Lingyu Hong, Hao Li, Haw Yang, and Kaushik Sengupta. Fully integrated fluorescence biosensors on-chip employing multi-functional nanoplasmonic optical structures in cmos. *IEEE Journal of Solid-State Circuits*, 52(9):2388–2406, 2017.

[42] Aleksandar D. Rakić, Aleksandra B. Djurišić, Jovan M. Elazar, and Marian L. Majewski. Optical Properties of Metallic Films for Vertical-Cavity Optoelectronic Devices. *Applied Optics*, 37(22):5271, 1998. ISSN 0003-6935. doi: 10.1364/ao.37.005271.

[43] H.-J. Hagemann, W. Gudat, and C. Kunz. Optical Constants from the Far Infrared to the x-Ray Region: Mg, Al, Cu, Ag, Au, Bi, C, and Al_2O_3. *Journal of the Optical Society of America*, 65(6):742, 1975. ISSN 0030-3941. doi: 10.1364/josa.65.000742.

[44] Lumerical. FDTD Product Reference Manual. URL `www.lumerical.com`.

[45] Kartikeya Murari, Ralph Etienne-Cummings, Nitish Thakor, and Gert Cauwenberghs. Which photodiode to use: a comparison of cmos-compatible structures. *IEEE sensors journal*, 9(7):752–760, 2009.

[46] C Patrick Yue and S Simon Wong. On-chip spiral inductors with patterned ground shields for si-based rf ics. *IEEE Journal of solid-state circuits*, 33(5): 743–752, 1998.

[47] Mohamed I. Ibrahim, Christopher Foy, Dirk R. Englund, and Ruonan Han. A Scalable Quantum Magnetometer in 65nm CMOS with Vector-Field Detection Capability. In *IEEE International Solid-State Circuits Conference*, pages 458–460, San Francisco, CA, 2019. ISBN 9781538685310. doi: 10.1109/ISSCC.2019.8662434.

[48] Mohamed I. Ibrahim, Christopher Foy, Dirk R. Englund, and Ruonan Han. High-scalability cmos quantum magnetometer with spin-state excitation and detection of diamond color centers. *IEEE Journal of Solid-State Circuits*, 56(3):1001–1014, 2021. doi: 10.1109/JSSC.2020.3027056.

[49] A. Dréau, M. Lesik, L. Rondin, P. Spinicelli, O. Arcizet, J. F. Roch, and V. Jacques. Avoiding Power Broadening in Optically Detected Magnetic Resonance of Single NV Defects for Enhanced DC Magnetic Field Sensitivity. *Physical Review B*, 84 (19):1–8, 2011. ISSN 1550235X.

[50] E. R. Eisenach, J. F. Barry, L. M. Pham, R. G. Rojas, D. R. Englund, and D. A. Braje. Broadband loop gap resonator for nitrogen vacancy centers in diamond. *Review of Scientific Instruments*, 89(9):094705, 2018. doi: 10.1063/1.5037465.

[51] Khadijeh Bayat, Jennifer Choy, Mahdi Farrokh Baroughi, Srujan Meesala, and Marko Loncar. Efficient, Uniform, and Large Area Microwave Magnetic Coupling to NV Centers in Diamond Using Double Split-Ring Resonators. *ACS: Nano Letters*, 14:1208–1213, 2014. ISSN 21622701.

[52] Ning Zhang, Chen Zhang, Lixia Xu, Ming Ding, Wei Quan, Zheng Tang, and Heng Yuan. Microwave Magnetic Field Coupling with Nitrogen-Vacancy Center Ensembles in Diamond with High Homogeneity. *Applied Magnetic Resonance*, 47 (6):589–599, 2016. ISSN 09379347.

[53] P. L. Stanwix, L. M. Pham, J. R. Maze, D. Le Sage, T. K. Yeung, P. Cappellaro, P. R. Hemmer, A. Yacoby, M. D. Lukin, and R. L. Walsworth. Coherence of Nitrogen-Vacancy Electronic Spin Ensembles in Diamond. *Physical Review B*, 82 (20), 2010. ISSN 10980121.

[54] Ali Hajimiri. The Future of High Frequency Circuit Design. In *Proc. of the European Solid State Device Research Conf.*, 2009. ISBN 978-1-4244-4351-2.

[55] Kaushik Sengupta and Ali Hajimiri. A 0.28 THz Power-Generation and Beam-Steering Array in CMOS Based on Distributed Active Radiators. *IEEE Journal of Solid-State Circuits*, 47(12):3013–3031, 2012. ISSN 00189200.

[56] Zhi Hu, Mehmet Kaynak, and Ruonan Han. High-Power Radiation at 1-THz in Silicon: A Fully Scalable Array Using A Multi-Functional Radiating Mesh Structure. *IEEE Journal of Solid-State Circuits (JSSC)*, 53(5):1313–1327, 2018.

[57] H.F. Talbot. Facts Relating to Optical Science. No. IV. *The London, Edinburgh, and Dublin Philosophical Magazine and Journal of Science*, 9(56):401–407, 1836. ISSN 1941-5966. doi: 10.1080/14786443608649032.

[58] Albert Wang and Alyosha Molnar. A light-field image sensor in 180 nm CMOS. *IEEE Journal of Solid-State Circuits*, 47(1):257–271, 2012. ISSN 00189200. doi: 10.1109/JSSC.2011.2164669.

[59] Cheng Wang and Ruonan Han. Molecular Detection for Unconcentrated Gas with ppm Sensitivity Using Dual-THz-Comb Spectrometer in CMOS. *IEEE Trans. Biomedical Circuits and Systems*, 12(3):709–721, 2018.

[60] V. M. Acosta, E. Bauch, M. P. Ledbetter, A. Waxman, L. S. Bouchard, and D. Budker. Temperature Dependence of the Nitrogen-Vacancy Magnetic Resonance in Diamond. *Physical Review Letters*, 104(7):1–4, 2010. ISSN 00319007. doi: 10.1103/PhysRevLett.104.070801.

[61] Roy Want. An Introduction to RFID Technology. *IEEE Pervasive Computing*, (January-March):25–33, 2006.

[62] Gitanjali Swamy and Sanjay Sarma. *White Paper: Manufacturing Cost Simulations for Low Cost RFID Systems.* MIT Auto-ID Center, 2003.

[63] Hugo Pristauz. RFID Chip Assembly for 0.1 Cents? *OnBoard Technology*, (September):46–49, 2006.

[64] Li-Xuan Chuo, Yao Shi, Zhihong Luo, Nikolaos Chiotellis, Zhiyoong Foo, Gyouho Kim, Yejoong Kim, Anthony Grbic, David Wentzloff, Hun-Seok Kim, and David Blaauw. A 915MHz Asymmetric Radio Using Q-Enhanced Amplifier for a Fully Integrated 3x3x3mmˆ3 Wireless Sensor Node with 20m Non-Line-of-Sight Communication. In *IEEE International Solid-State Circuits Conference (ISSCC)*, pages 132–134, 2017. ISBN 9781509037582.

[65] Bo Zhao, Nai Chung Kuo, Benyuanyi Liu, Yi An Li, Lorenzo Lotti, and Ali M. Niknejad. A 5.8GHz Power-Harvesting 116μmx116μm "Dielet" Near-Field Radio with On-Chip Coil Antenna. In *IEEE International Solid-State Circuits Conference (ISSCC)*, pages 456–458, 2018. ISBN 9781509049394. doi: 10.1109/ISSCC.2018.8310381.

[66] Adam Khalifa, Yasha Karimi, Qihong Wang, Sahithi Garikapati, Webert Montlouis, Milutin Stanaćević, Nitish Thakor, and Ralph Etienne-Cummings. The microbead: A highly miniaturized wirelessly powered implantable neural stimulating system. *IEEE transactions on biomedical circuits and systems*, 12(3): 521–531, 2018.

[67] S. O'Driscoll, S. Korhummel, P. Cong, Y. Zou, K. Sankaragomathi, J. Zhu, T. Deyle, A. Dastgheib, B. Lu, M. Tierney, J. Shao, C. Gutierrez, S. Jones, and H. Yao. A 200µm × 200µm × 100µm, 63nw, 2.4ghz injectable fully-monolithic wireless bio-sensing system. In *2017 IEEE Radio Frequency Integrated Circuits Symposium (RFIC)*, pages 256–259, 2017. doi: 10.1109/RFIC.2017.7969066.

[68] Maryam Tabesh, Mustafa Rangwala, Ali Niknejad, and Amin Arbabian. A Power-Harvesting Pad-Less mm-Sized 24/60GHz Passive Radio with On-Chip Antennas. In *IEEE Symposium of Very-Large-Scale Integrated Circuits (VLSI)*, 2014. ISBN 9781479933280.

[69] Chiraag Juvekar, Hyung-Min Lee, Joyce Kwong, and Anantha Chandrakasan. A Keccak-Based Wireless Authentication Tag with per-Query Key Update and Power-Glitch Attack Countermeasures. In *IEEE International Solid-State Circuits Conference (ISSCC)*, pages 290–292, 2016. ISBN 9781467394673.

[70] Taiyun Chi, Hechen Wang, Min-Yu Huang, Fa Foster Dai, and Hua Wang. A Bidirectional Lens-Free Digital-Bit-In/-Out 0.57mmˆ2 Terahertz Nano-Radio in CMOS with 49.3mW Peak Power Consumption Supporting 50cm Internet-of-Things Communication. In *IEEE Custom Integrated Circuits Conference (CICC)*, 2017. ISBN 9781509051915.

[71] Mohamed I. Ibrahim, Muhammad Ibrahim Wasiq Khan, Chiraag S. Juvekar, Wanyeong Jung, Rabia Tugce Yazicigil, Anantha P. Chandrakasan, and Ruonan Han. THzID: A 1.6mmˆ2 Package-Less Cryptographic Identification Tag with Backscattering and Beam-Steering at 260GHz. In *IEEE Intl. Solid-State Circuits Conference (ISSCC)*, pages 24–26, 2020. ISBN 9781728132051.

[72] Muhammad Ibrahim Wasiq Khan, Mohamed I. Ibrahim, Chiraag S. Juvekar, Wanyeong Jung, Rabia Tugce Yazicigil, Anantha P. Chandrakasan, and Ruonan Han. Cmos thz-id: A 1.6-mm^2 package-less identification tag using asymmetric cryptography and 260-ghz far-field backscatter communication. *IEEE Journal of Solid-State Circuits*, 56(2):340–354, 2021. doi: 10.1109/JSSC.2020.3015717.

[73] Jens Hermans, Roel Peeters, and Cristina Onete. Efficient, Secure, Private Distance Bounding without Key Updates. In *Proc. 6th ACM Conf.Security Privacy Wireless Mobile Network*, pages 207–218, 2013. ISBN 9781450319980.

[74] Constantine Balanis. *Antenna Theory, Third Edition.* Wiley-Interscience, 2005.

[75] Cheng Wang and Ruonan Han. Dual-Terahertz-Comb Spectrometer on CMOS for Rapid, Wide-Range Gas Detection with Absolute Specificity. *IEEE Journal of Solid-State Circuits*, 52(12):3361–3372, 2017. ISSN 00189200. doi: 10.1109/JSSC.2017.2755693.

[76] Erik Öjefors, Ullrich R Pfeiffer, Alvydas Lisauskas, and Hartmut G Roskos. A 0.65 THz Focal-Plane Array in a Quarter-Micron CMOS Process Technology. *IEEE Journal of Solid State Circuits*, 44(7):1968–1976, 2009.

[77] Muhammad Ibrahim Wasiq Khan, Suna Kim, Dae Woong Park, Hyoung Jun Kim, Seok Kyun Han, and Sang Gug Lee. Nonlinear Analysis of Nonresonant THz Response of MOSFET and Implementation of a High-Responsivity Cross-Coupled THz Detector. *IEEE Transactions on Terahertz Science and Technology*, 8(1): 108–120, 2018. ISSN 2156342X. doi: 10.1109/TTHZ.2017.2778499.

[78] Roel Peeters and Jens Hermans. Wide strong private rfid identification based on zero-knowledge. *IACR Cryptology ePrint Archive*, 2012:389, 2012.

[79] Harald T. Friis. A Note on a Simple Transmission Formula. *Proceedings of the IRE and Waves and Electrons*, 34(5):254–256, 1946. ISSN 0096-8390. doi: 10.1109/JRPROC.1946.234568.

[80] VM Acosta, E Bauch, MP Ledbetter, C Santori, K-MC Fu, PE Barclay, RG Beausoleil, H Linget, JF Roch, F Treussart, et al. Diamonds with a high density of nitrogen-vacancy centers for magnetometry applications. *Physical Review B*, 80 (11):115202, 2009.

[81] Thomas Oeckinghaus, Rainer Stöhr, Roman Kolesov, Julia Tisler, Friedemann Reinhard, and Jörg Wrachtrup. A compact, diode laser based excitation system for microscopy of nv centers. *Review of Scientific Instruments*, 85(7):073101, 2014.

[82] Daiji Kasahara, Daisuke Morita, Takao Kosugi, Kyosuke Nakagawa, Jun Kawamata, Yu Higuchi, Hiroaki Matsumura, and Takashi Mukai. Demonstration of blue and green gan-based vertical-cavity surface-emitting lasers by current injection at room temperature. *Applied Physics Express*, 4(7):072103, 2011.

[83] David J Moss, Roberto Morandotti, Alexander L Gaeta, and Michal Lipson. New cmos-compatible platforms based on silicon nitride and hydex for nonlinear optics. *Nature photonics*, 7(8):597, 2013.

[84] Song Peng and G Michael Morris. Resonant scattering from two-dimensional gratings. *JOSA A*, 13(5):993–1005, 1996.

[85] Sajjad Moazeni, Eric H. Pollmann, Vivek Boominathan, Filipe A. Cardoso, Jacob T. Robinson, Ashok Veeraraghavan, and Kenneth L. Shepard. 19.2 a mechanically flexible implantable neural interface for computational imaging and optogenetic stimulation over 5.4×5.4 mm 2 fov. In *2021 IEEE International Solid- State Circuits Conference (ISSCC)*, volume 64, pages 288–290, 2021. doi: 10.1109/ISSCC42613.2021.9365796.

[86] F. Jelezko, T. Gaebel, I. Popa, A. Gruber, and J. Wrachtrup. Observation of coherent oscillations in a single electron spin. *Phys. Rev. Lett.*, 92:076401, Feb 2004.

[87] David R Glenn, Dominik B Bucher, Junghyun Lee, Mikhail D Lukin, Hongkun Park, and Ronald L Walsworth. High-resolution magnetic resonance spectroscopy using a solid-state spin sensor. *Nature*, 555(7696):351, 2018.

[88] J.-C. Jaskula, K. Saha, A. Ajoy, D.J. Twitchen, M. Markham, and P. Cappellaro. Cross-sensor feedback stabilization of an emulated quantum spin gyroscope. *Physical Review Applied*, 11(5), May 2019. ISSN 2331-7019. doi: 10.1103/physrevapplied.11.054010. URL `http://dx.doi.org/10.1103/PhysRevApplied.11.054010`.

[89] Ruonan Han, Yaming Zhang, Youngwan Kim, Dae Yeon Kim, Hisashi Shichijo, Ehsan Afshari, and Kenneth K. O. Active terahertz imaging using schottky diodes in CMOS: Array and 860-GHz pixel. *IEEE Journal of Solid-State Circuits*, 48(10):2296–2308, 2013.

[90] Mohamed Hussein Eissa and Dietmar Kissinger. A 13.5dBm Fully Integrated 200-to-255GHz Power Amplifier with a 4-Way Power Combiner in SiGe:C BiCMOS. In *IEEE International Solid-state Circuits Conference (ISSCC)*, pages 82–84, San Francisco, CA, 2019. IEEE. ISBN 9781538685310. doi: 10.1109/ISSCC.2019.8662424.

[91] B Heinemann, H Rücker, R Barth, F Bärwolf, J Drews, G G Fischer, A Fox, O Fursenko, T Grabolla, F Herzel, J Katzer, J Korn, A Krüger, P Kulse, T Lenke, M Lisker, S Marschmeyer, A Scheit, D Schmidt, J Schmidt, M A Schubert, A Trusch, C Wipf, and D Wolansky. SiGe HBT with fT/fmax of 505 GHz/720

GHz. In *IEEE International Electron Device Meeting*, pages 51–54, San Francisco, CA, 2016. ISBN 9781509039029. doi: 10.1109/IEDM.2016.7838335.

[92] S. N. Ong, S. Lehmann, W. H. Chow, C. Zhang, C. Schippel, L. H.K. Chan, Y. Andee, M. Hauschildt, K. K.S. Tan, J. Watts, C. K. Lim, A. Divay, J. S. Wong, Z. Zhao, M. Govindarajan, C. Schwan, A. Huschka, A. Bcllaouar, W. Loo, J. Mazurier, C. Grass, R. Taylor, K. W.J. Chew, S. Embabi, G. Workman, A. Pakfar, S. Morvan, K. Sundaram, M. T. Lau, B. Rice, and D. Harame. A 22nm FDSOI Technology Optimized for RF/mmWave Applications. In *IEEE Radio Frequency Integrated Circuits Symposium*, 2018. ISBN 9781538645451. doi: 10.1109/RFIC.2018.8429035.

[93] H Lee, S Rami, S Ravikumar, V Neeli, K Phoa, B Sell, and Y Zhang. Intel 22nm FinFET (22FFL) Process Technology for RF and mmWave Applications and Circuit Design Optimization for FinFET Technology. In *2018 IEEE International Electron Devices Meeting (IEDM)*, pages 316–319, San Francisco, CA, 2018. IEEE. ISBN 9781728119878.

[94] H. J. Lee, S. Morarka, S. Rami, Q. Yu, M. Weiss, G. Liu, M. Armstrong, C.-Y. Su, D. Ali, B. Sell, and Y. Zhang. Implementation of High Power RF Devices with Hybrid Workfunction and OxideThickness in 22nm Low-Power FinFET Technology. In *IEEE International Electron Devices Meetings (IEDM)*, pages 610–613, San Francisco, CA, 2019. ISBN 9781728140315. doi: 10.1109/IEDM19573.2019.8993647.

[95] Hannes Bernien, Bas Hensen, Wolfgang Pfaff, Gerwin Koolstra, MS Blok, Lucio Robledo, TH Taminiau, Matthew Markham, DJ Twitchen, Lilian Childress, et al. Heralded entanglement between solid-state qubits separated by three metres. *Nature*, 497(7447):86, 2013.

[96] Wolfgang Pfaff, BJ Hensen, Hannes Bernien, Suzanne B van Dam, Machiel S Blok, Tim H Taminiau, Marijn J Tiggelman, Raymond N Schouten, Matthew Markham, Daniel J Twitchen, et al. Unconditional quantum teleportation between distant solid-state quantum bits. *Science*, 345(6196):532–535, 2014.

[97] Peter C Humphreys, Norbert Kalb, Jaco PJ Morits, Raymond N Schouten, Raymond FL Vermeulen, Daniel J Twitchen, Matthew Markham, and Ronald Hanson. Deterministic delivery of remote entanglement on a quantum network. *Nature*, 558(7709):268, 2018.